



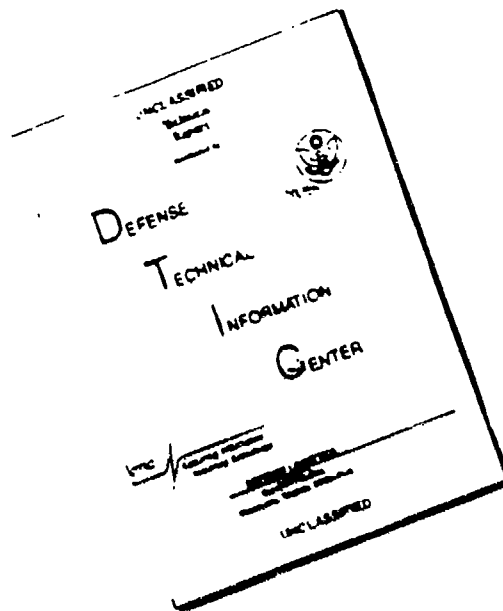
Information is estimated to average 1 hour per response, including the time for reviewing instructions, searching existing data sources, completing and reviewing the collection of information. Send comments regarding this burden estimate or any other aspect of this burden estimate, including suggestions for reducing this burden, to Washington Headquarters Services, Directorate for Information Operations and Reports, 1215 Jefferson Avenue, Washington, DC 20540, and to the Office of Management and Budget, Paperwork Reduction Project (0704-0188), Washington, DC 20503.

1. AGENCY USE ONLY (Leave blank)		2. REPORT DATE 1991	3. REPORT TYPE AND DATES COVERED THESIS/DISSERTATION	
4. TITLE AND SUBTITLE Validation of the Thermospheric Vector Spherical Harmonic (VSH) Computer Model			5. FUNDING NUMBERS	
6. AUTHOR(S)  Jerry Lynn Davis Jr.				
7. PERFORMING ORGANIZATION NAME(S) AND ADDRESS(ES)  AFIT Student Attending: The Univ of Michigan			8. PERFORMING ORGANIZATION REPORT NUMBER  AFIT/CI/CIA-93-067	
9. SPONSORING/MONITORING AGENCY NAME(S) AND ADDRESS(ES) DEPARTMENT OF THE AIR FORCE AFIT/CI 2950 P STREET WRIGHT-PATTERSON AFB OH 45433-7765			10. SPONSORING/MONITORING AGENCY REPORT NUMBER	
11. SUPPLEMENTARY NOTES				
12a. DISTRIBUTION/AVAILABILITY STATEMENT  Approved for Public Release IAW 190-1 Distribution Unlimited MICHAEL M. BRICKER, SMSgt, USAF Chief Administration			12b. DISTRIBUTION CODE	
13. ABSTRACT (Maximum 200 words)				
14. SUBJECT TERMS				
15. NUMBER OF PAGES 99			16. PRICE CODE	
17. SECURITY CLASSIFICATION OF REPORT	18. SECURITY CLASSIFICATION OF THIS PAGE	19. SECURITY CLASSIFICATION OF ABSTRACT	20. LIMITATION OF ABSTRACT	

DTIC  
ELECTE  
AUG 13 1993  
S C D

93-18726

# DISCLAIMER NOTICE



THIS DOCUMENT IS BEST QUALITY AVAILABLE. THE COPY FURNISHED TO DTIC CONTAINED A SIGNIFICANT NUMBER OF PAGES WHICH DO NOT REPRODUCE LEGIBLY.



93-067

The University of Michigan  
Department of Atmospheric, Oceanic and Space Sciences  
Space Physics Research Laboratory

**VALIDATION OF THE THERMOSPHERIC VECTOR SPHERICAL  
HARMONIC (VSH) COMPUTER MODEL**

by

Jerry Lynn Davis Jr.

Advisors:

Professor, Timothy L. Killeen  
Assistant Research Scientist, Alan G. Burns

Phillips Laboratory  
Grant Number F19623-89-K-0047

DTIC QUALITY INSPECTED 3



Accession For	
NTIS CRA&I	<input checked="checked" type="checkbox"/>
DTIC TAB	<input type="checkbox"/>
Unannounced	<input type="checkbox"/>
Justification	
By	
Distribution/	
Availability Codes	
Dist	Avail and/or Special
A-1	

**VALIDATION OF THE THERMOSPHERIC VECTOR SPHERICAL  
HARMONIC (VSH) COMPUTER MODEL**

by

**Jerry Lynn Davis Jr.**

**A thesis submitted in partial fulfillment  
of the requirement for the degree of  
Master of Science  
(Atmospheric and Space Sciences)  
in the University of Michigan  
1991**

**Advisors:**

**Professor, Timothy L. Killeen  
Assistant Research Scientist, Alan G. Burns**

© Jerry Lynn Davis Jr. 1991  
All Rights Reserved

## ABSTRACT

A semi-empirical computer model of the lower thermosphere has been developed that provides a description of the composition and dynamics of the thermosphere (Killeen et al., 1992). Input variables needed to run the VSH model include time, space and geophysical conditions.

One of the output variables the model provides, neutral density, is of particular interest to the U.S. Air Force. Neutral densities vary both as a result of change in solar flux (eg. the solar cycle) and as a result of changes in the magnetosphere (eg. large changes occur in neutral density during geomagnetic storms). Satellites in earth orbit experience aerodynamic drag due to the atmospheric density of the thermosphere. Variability in the neutral density described above affects the drag a satellite experiences and as a result can change the orbital characteristics of the satellite. These changes make it difficult to track the satellite's position.

Therefore, it is particularly important to insure that the accuracy of the model's neutral density is optimized for all input parameters. To accomplish this, a validation program was developed to evaluate the strengths and weaknesses of the model's density output by comparing it to SETA-2 (satellite electrostatic accelerometer) total mass density measurements.

The SETA-2 instrument was flown on a low altitude satellite in 1982 during solar maximum of solar cycle 21. The data set used includes over 186,000 data points gathered between 17 May and 22 July 1982. As a result, a large statistical distribution was available to determine deviations of the VSH model density from the SETA-2 data.

Density output from the MSIS-86 (Mass Spectrometer-Incoherent Scatter) empirical model was also compared with the SETA-2 data set. In this way comparisons of VSH and MSIS deviations from SETA 2 could be used to test their performance.

A one to one comparison was made between the VSH and MSIS models and the satellite data. The average relative error, or percent difference, for the models was calculated for each point and was plotted against their frequency of occurrence.

A significant shortcoming in the model was discovered as a result of conducting this validation study. By binning the data in a variety of parameters we were able to evaluate latitudinal and geomagnetic dependences of the two models. Initially, the plots showed there were conditions when the VSH model overestimated neutral densities. The data was binned by F10.7 values and was discovered that the area of overestimation occurred during times of high F10.7. This problem was corrected and subsequent results showed lower standard deviation values by 10% (for this particular case). The study also showed that the models provided the best standard deviations (6-8%) in the low latitude regions and during low magnetic activity and conversely, poorer standard deviations (15-18%) in the high latitudes and during high magnetic activity.

Atmospheric density is not the only cause of drag that a satellite experiences. In-track winds that are anti-parallel to the direction of the satellite can also induce drag, affecting the orbit of the satellite. In particular, winds in the polar cap region can reach speeds over 1000 m/s, or roughly 10-15% of the satellite speed.

In an attempt to quantify some of these questions, neutral winds from the VSH model were calculated throughout a typical orbit. Many

different orbital tracks were used where different parameters were changed, such as varying the local time "slice" of the satellite's orbit in order to find in-track winds in the polar region where these circulation cells exist.

These winds are quite important, with results showing that for a 742 m/s wind the satellite drag changes by 23%. This is for a satellite crossing the polar cap region across the 14-02 local time meridian during high magnetic activity. However, this is a very specific case during a certain day, the circulation cell is highly variable in it's position. Nevertheless, it is important to know what local times the convergence area of the circulation cells occur and the direction of these winds.



## **ACKNOWLEDGEMENTS**

While working on my M.S. degree here at the University of Michigan there were a number of people who helped me attain my goal; however, special thanks should go to the U.S. Air Force for allowing me to attend this fine university.

First of all I would like to thank Dr. Tim Killeen and Alan Burns for their advice, motivation, and patience while working towards my goal. I am also appreciative of Pat Purcell, Tom Smith, and Steve Lehr for their friendship and overall help. Others I would like to thank; Gerry Schmitt who was extremely helpful with the many programming problems I had while conducting my research, Nelly DeMaldonado for her friendship, guidance and vast administrative help, Ed Hume and his help preparing my thesis, and Rob Raskin and Mike Minock who patiently answered my many questions about VSH.

Most of all, I would like to express my love and appreciation for my wife Ruth. Without her the whole task would have been unbearable and nearly impossible. And finally, my son, Quinten Storm; thoughts of him throughout the day momentarily took away the frustrations and problems I experienced.

## TABLE OF CONTENTS

<b>Abstract</b>	
<b>Acknowledgements</b>	<b>i</b>
<b>1. Introduction</b>	<b>1</b>
1.1 General	1
1.2 Thermospheric neutral density and winds	2
1.2.1 Control of thermospheric density	4
1.2.1.1 Solar flux and geomagnetic indices	8
1.2.1.2 Geomagnetic storms	11
1.2.2 High latitude winds	13
1.3 Aerodynamic drag	14
<b>2. Description of tools used</b>	<b>17</b>
2.1 Thermospheric General Circulation Models (TGCMs)	17
2.2 Vector Spherical Harmonic (VSH) Model	19
2.2.1 Spherical Harmonics	21
2.2.2 Interpolation Methods	23
2.2.3 Truncation	25
2.3 Mass Spectrometer-Incoherent Scatter (MSIS) model	27
2.4 SETA-2 instrument	31
2.4.1 Operation	32
2.4.2 Data	34
2.4.3 Orbital characteristics	37
2.5.1 NACS instrument	40
2.5 Statistical Techniques	42
<b>3. Validation study results</b>	<b>48</b>

3.1 Introduction.....	48
3.2 Comparison of VSH and MSIS to SETA-2.....	48
3.2.1 Discovery of F10.7 dependence.....	49
3.2.1.1 Height variation.....	56
3.2.2 Model to data comparisons using current VSH .....	58
3.2.2.1 Overall dependence.....	60
3.2.2.2 Kp dependence.....	62
3.2.2.3 Latitude dependence.....	64
3.2.2.4 Standard deviation comparisons .....	72
3.3 Conclusions .....	77
4. Effects of orbital in-track winds on satellite drag .....	79
4.1 Introduction.....	79
4.2 Procedure .....	80
4.3 Results and discussion .....	81
5. Discussion.....	84
Appendix A F10.7 dependence.....	88
References.....	96

## CHAPTER 1

### INTRODUCTION

#### 1.1 General

The objective of this thesis is the validation of the neutral density output of the VSH (Vector Spherical Harmonic) model and the determination of the atmospheric drag effects on artificial satellites due to in-track winds using VSH model neutral wind output.

When planning a satellite mission it is important to consider the atmospheric drag effects on the satellite. Drag affects the lifetime prediction, design and control, tracking, on-board fuel requirements, and the reentry (Marcos et al., 1989). Therefore, accurate specification of neutral density is quite important and one of the primary objectives of the VSH thermospheric model.

To validate the model, neutral density measurements from the satellite electrostatic triaxial accelerometer (SETA-2) instrument are used. The VSH model is also compared with output from the Mass Spectrometer-Incoherent Scatter (MSIS-86) (Hedin, 1987) empirical model.

The effects of wind drag on satellites is quantified by comparing the satellite drag due to in-track winds to the drag without winds for different cases dependent on magnetic activity and satellite orbit paths.

The first chapter contains background information on the theory of upper atmospheric dynamics and the parameters that control thermospheric density structure. Also, increases in drag due to polar winds are explained.

The next chapter contains details on the research tools utilized. Information on thermospheric general circulation models (TGCMs) is included as a prelude to the section on the VSH computer model. VSH model output is compared against total density measurements from the SETA-2 instrument and the instrument on the Dynamics Explorer 2 (DE-2) satellite. The 1986 version of the MSIS empirical model (Hedin, 1987) is used to make model-to-model comparisons. And finally, the technique used to compare satellite data to the models is illustrated.

The next chapter goes into the model validation program that was created and the systematic process used to compare model and data. Satellite data was binned using a variety of parameters to evaluate model characteristics. Inclusion of an additional solar flux parameterization was added based on results from this study. Validation studies such as this are important in continuously updating and improving model performance.

The atmospheric drag effects of wind on a satellite is detailed in chapter four. And finally, a discussion of current and future research is summarized in chapter five.

## **1.2 Thermospheric neutral density and winds**

Since the objective of this thesis is the validation of neutral density output of the VSH thermospheric model, some background on the modelled region should be provided.

In general, the mean atmospheric density decreases with altitude. In the lower atmosphere up to 100 km, most of the chemical species behave as one and decrease exponentially by the barostatic distribution equation

$$\rho(z) = \rho(z_0)e^{-\frac{\bar{m}g}{kT}(z-z_0)} \quad (1.1)$$

where density,  $\rho$ , drops off with respect to some reference altitude  $z_0$  exponentially by the scale height of the gas. The scale height

$$H = \frac{kT}{\bar{m}g} \quad (1.2)$$

of the overall gas with mean molecular mass  $\bar{m}$  at a constant temperature,  $T$ , and constant gravity,  $g$ , ( $k$  being Boltzmann's constant) is the "thickness" that the gas would exhibit if held at a reference pressure. Based on this equation it can be seen that heavy gases have small scale heights and light gases have large scale heights. This lower region is called the homosphere and is dominated by eddy diffusion, the process by which the individual gases are fully mixed due to winds and turbulence.

Above 100 km, well into the thermosphere, eddy diffusion gives way to molecular diffusion in the heterosphere. The individual species gravitationally separate based on their own masses and exhibit individual scale heights. In equation 1.2,  $H$  and  $\bar{m}$  change to  $H_i$  and  $m_i$  where the subscript  $i$  represents each individual species scale height and mass, respectively. Figure 1.1 illustrates this distinction in scale heights in the homosphere and heterosphere. It can be seen that the heavier species such as argon (Ar) and ozone (O<sub>3</sub>) begin to fall off (with respect to density) more rapidly than the lighter species (He) around 100 km. In the heterosphere

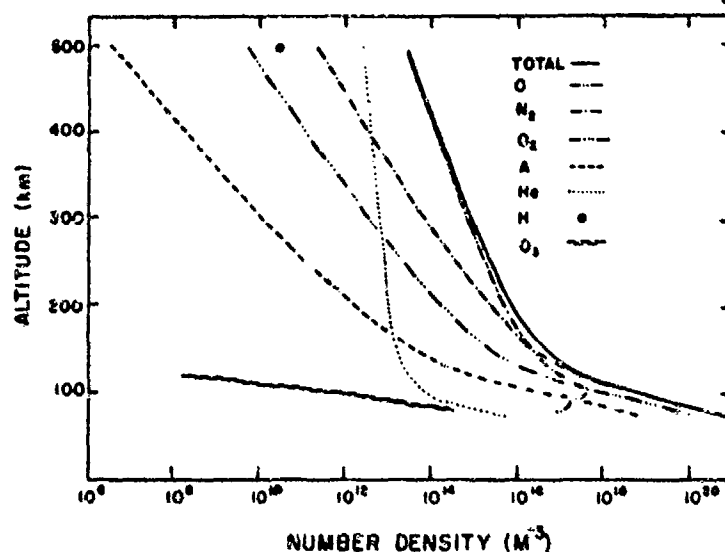


Figure 1.1 Density profiles of various atmospheric constituents.

most of the species are in molecular equilibrium, meaning that there is no net motion of an individual species through the rest of the gases.

The most important and abundant chemical species in the thermosphere are O, O<sub>2</sub>, and N<sub>2</sub>. Molecular nitrogen is chemically inert and is in molecular equilibrium, and therefore, is controlled by dynamic transport. However, O and O<sub>2</sub> are not in molecular equilibrium, instead, their density profiles are controlled by chemistry in the lower thermosphere.

### 1.2.1 Control of thermospheric density

The density structure of the thermosphere is best described by evaluating one of the primitive, or governing, equations for the thermosphere. There are three equations, the conservation of mass, momentum, and energy. The equation for the conservation of mass, also called the continuity equation, best describes the processes responsible for the composition and density structure of the thermosphere.

The single species continuity equation for the thermosphere is given in terms of the ratio of the individual species density to that of the whole gas, the mass mixing ratio  $\Psi$ :

$$\begin{aligned} \frac{\partial \bar{\Psi}}{\partial t} = & -\frac{e^{-z}}{\tau} \frac{\partial}{\partial z} \left[ \frac{\bar{m}}{m_{N_2}} \left( \frac{T_{00}}{T} \right)^{0.25} \frac{L}{\alpha} \bar{\Psi} \right] \\ & + e^z \frac{\partial}{\partial z} \left[ K(z) e^{-z} \frac{\partial}{\partial z} \bar{\Psi} \right] - \left[ \bar{\mathbf{V}} \cdot \nabla \bar{\Psi} + w \frac{\partial}{\partial z} \bar{\Psi} \right] + \bar{\mathbf{S}} - \bar{\mathbf{R}} \end{aligned} \quad (1.3)$$

The terms on the right-hand side of the equation are, respectively, changes in composition due to molecular diffusion, eddy diffusion, horizontal and vertical advection, and finally, chemical production and loss (Killeen et al., 1988). The various terms are:

$\bar{\mathbf{V}}$  = horizontal velocity vector

$w$  = vertical neutral velocity

$T$  = temperature

$T_{00}$  = surface temperature (273 K)

$\tau$  = diffusion time scale

$L$  = matrix of diffusive equilibrium solutions

$\alpha$  = matrix of diffusion coefficients

$\mathbf{S}$  = matrix for chemical production rates

$\mathbf{R}$  = matrix for chemical loss rates



Looking at each term and applying it to the lower thermosphere, we can choose the most important process that affects variations in the total density.

The chemical sources and sinks are important for individual species chemistry but not so for total density. Also, molecular and eddy diffusion have significance for individual species density profiles but are of little importance in specifying perturbations in total density (Killeen et al., 1988). Therefore, variations in the mean density structure of the thermosphere are primarily controlled by horizontal and vertical advective effects (Killeen et al., 1988). These advective effects are caused by heating or momentum exchange.

Thermospheric neutral winds respond to differential heating by flowing from the warm day side to the cooler night side of the earth (figure 1.2) and from the summer to the winter hemisphere. This thermospheric flow results in restoring the global temperature distribution. Subsequently, this flow causes day-night and summer-winter horizontal density gradients due to the advective effects of the winds.

Winds also reside in large scale systems such as planetary waves and diurnal tides (the "breathing effect" of the atmosphere in response to the daily solar EUV/UV heating), and small scale systems such as gravity waves and localized upwelling (as a result of local heating) (Killeen et al., 1988). These occurrences of momentum transfer create vertical winds, resulting in changes to the density profile. For instance, the diurnal tide creates upward winds (increased total mass density) during the day and downward winds (decreased total mass density) during the night. Figure 1.3 clearly illustrates this diurnal variation, where the vertical axis is

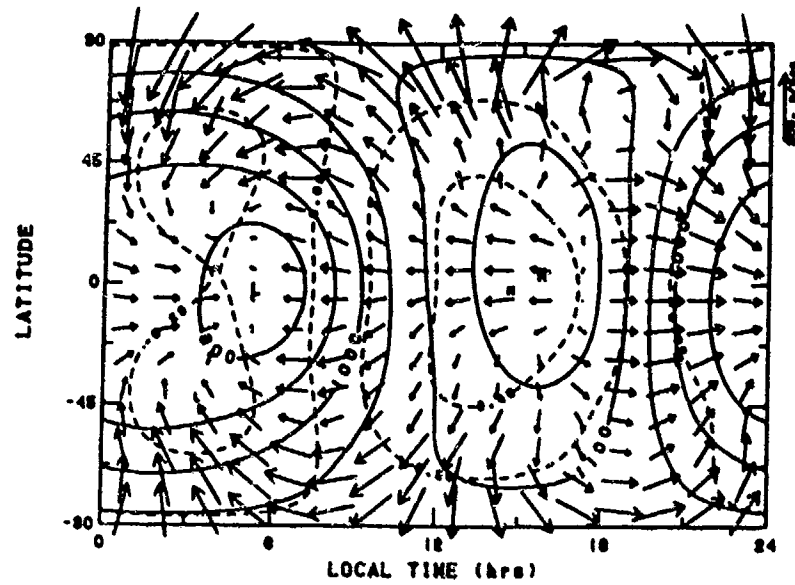


figure 1.2 Illustration of horizontal wind flow due to differential heating (Hedin et al., 1988).

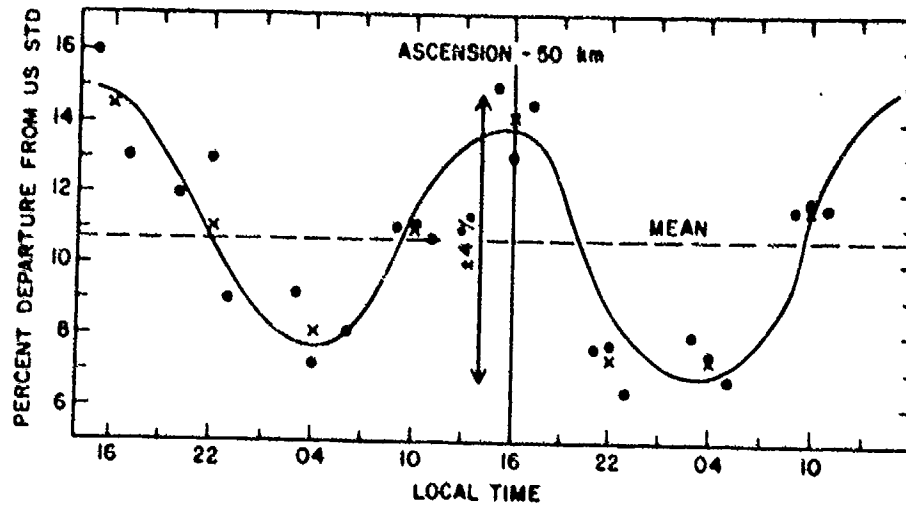


figure 1.3 Diurnal variation in density due to the diurnal tide (AFGL, 1985).

departure from the U.S. standard atmosphere density and the horizontal axis is local time. The thermospheric wind system, and resultingly, the density structure, can also be disrupted by the 11 year solar cycle and geomagnetic storms. More information on geomagnetic storms and their effect on total mass density is discussed in section 1.2.1.2. These are specific occurrences which essentially result in changes to the density structure described in the above paragraphs. These features are perturbations that cause variations in the mean density structure, but what restores the mean density structure?

For a "steady state" thermosphere, the horizontal and vertical total mass density profiles are governed by the distribution law, equation 1.1, for each of its individual species, which simply says that the temperature profile is the controlling factor. The temperature profile, in turn, is controlled by thermospheric heat sources and sinks which are solar EUV/UV heating (source) and downward heat conduction (sink). Downward heat conduction to the mesosphere is the primary means of the thermosphere to dissipate heat. Therefore, the balance between these two factors control the mean, or globally averaged, density structure.

#### **1.2.1.1 Solar flux and geomagnetic indices**

The 10.7 cm (2800 MHz) solar radio emission has been extensively used to indicate solar activity. This emission has been designated the F10.7 index and correlates well with the sunspot number (figure 1.4), which, based on hundreds of years of recorded observations, is clearly indicative of solar activity (AFGL, 1985).

An F10.7 value gives the day-to-day variability, and can vary greatly over a short period. A slowly variable index was found to be useful in upper

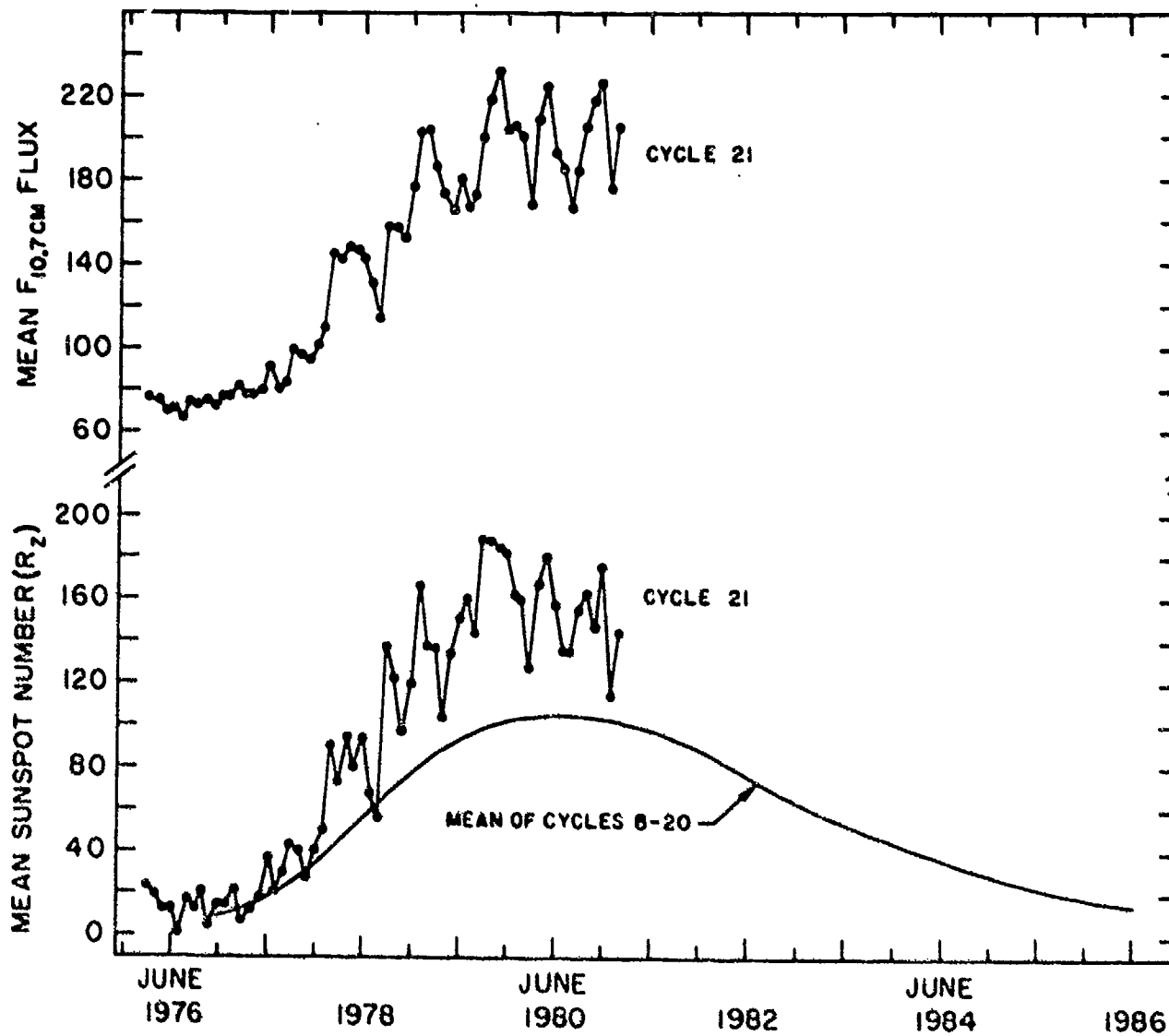


figure 1.4 Illustration showing correlation between sunspot numbers to solar flux (AFGL, 1985).

atmospheric models; the F10.7 average (F10.7a) value, accounts for the long-term variability (Hinteregger, 1981) of the sun. This value is a running 81 day average of the previous F10.7 values (Hinteregger, 1981). For some thermospheric computer models, as in the case of the MSIS model, the F10.7a value is calculated by a  $\pm 40$  day mean value for its determination of exospheric temperatures (Hinteregger, 1981). A study by Hinteregger [1981] using AE-E observations lead to the conclusion that EUV fluxes correlate with F10.7a more so than with the daily F10.7 value. This discovery also relates well with the results of this validation study, showing that VSH needed F10.7a as an input parameter in addition to the daily F10.7 value to improve its density output.

Even though the 10.7 cm solar flux is a good indicator of the sun's variability, it still can only be considered a proxy to the more indicative solar EUV/UV emissions. The 10.7 cm emission is different from these stronger UV emissions. While the former comes from the upper chromosphere, lower corona region of the sun, EUV/UV emissions come from a broad region of the solar atmosphere where the temperatures, densities, and altitudes are quite different (AFGL, 1985).

EUV/UV emissions are primarily responsible for the earth's global energy budget (Torr et al., 1981) and would be the perfect indicator for solar-terrestrial interactions. However, trying to index these many different EUV/UV spectral lines would make their use impractical. Also, the success of the MSIS model and Jacchia satellite drag model and their level of verified inconsistencies with actual aeronomical observations shows that a large number of solar variability indices is not really needed anyway (Hinteregger, 1981).

A number of indices have been developed to measure geomagnetic activity. The K index was developed to show irregular variations in magnetograms, which are indicators of magnetic disturbances such as geomagnetic storms.

The K index is taken at 3 hour intervals based on the difference between the highest and lowest deviations from the regular daily variation in the magnetic field. Due to the structure of the earth's magnetosphere, this index primarily indicates auroral, or high-latitude, activity (AFGL, 1985).

K values are roughly logarithmic integers from 0 to 9. The Kp index, where p stands for "planetary", is intended to reflect the worldwide average level of magnetic activity (AFGL, 1985).

The ap and Ap index is also widely used, mostly when averaging of the 3-hourly Kp values is needed to get a daily average. The ap value has a linear range that is converted from the Kp range by use of a standardized table (AFGL, 1985). The ap values are then averaged over eight 3-hour intervals to get the daily Ap index. Ap values range from 0 to 400.

The need for the indexing of solar flux and geomagnetic activity primarily arises in computer models that simulate the earth's upper atmosphere. The VSH model, for instance, is strongly dependent on variations in the daily solar flux, and a simple index characterizing this field helps in simplifying the model.

#### **1.2.1.2 Geomagnetic storms**

Geomagnetic disturbances come about from the transfer of energy from the solar wind to the earth's magnetosphere. The largest

disturbances of the magnetosphere are called magnetospheric storms and the resulting disturbance of the geomagnetic field is called a geomagnetic storm (AFGL, 1985). These larger disturbances are primarily due to a sudden impulse from a shock in the solar wind. Shocks in the solar wind are sometimes caused by solar flares (Roble et al, 1987).

This transfer of energy causes enhanced particle precipitation (ie. enhanced mean particle energy) in the earth's auroral, or high latitude, region and also causes magnetospheric convection. These processes disturb the high-latitude thermospheric wind circulation patterns, temperature, and composition.

Forbes et al. [1987] describes the effects on total mass density by such a storm using satellite neutral wind and total mass density measurements. Their results show that densities in the high latitude region of the northern hemisphere were enhanced on the day-side by about 60% during the peak of the magnetic storm. This enhancement corresponded with intense heating. The measurement was taken at 180 km at the throat of the ion convection pattern (see section 1.2.2). This area of the ion convection pattern has enhanced particle and Joule heating and strong convergence during geomagnetic storms (Roble et al., 1987). Joule heating is the frictional heating due to the changes between the accelerated ions and the slower neutral particles that flow with them.

The disturbance increases the density as it propagates from the high latitudes to the equator. Satellite measurements on the night-side show less latitudinal density enhancement, where the disturbance did not propagate equatorward as extensively (Forbes et al., 1987). After the storm passes, densities continue to stay high (10-20%) (Forbes et al., 1987) compared to pre-storm conditions.

### 1.2.2 High latitude winds

The previous section describes thermospheric composition and winds in general. I will now go into some background information needed to help explain my research in the effects of atmospheric drag due to winds experienced by satellites.

Thermospheric winds reach a maximum in the polar cap regions of the earth. During strong geomagnetic storms, neutral winds can reach speeds well over 1000 m/sec (Killeen et al., 1988), and when compared with the average satellite speed of 8000 m/sec, the wind can change the drag/lift forces on the satellite by 50% under worse case conditions.

In the higher latitudes neutral winds follow the ion convection pattern. This circulation pattern results from interactions between the solar wind, magnetosphere and the ionosphere.

The solar wind interacts with the magnetosphere producing dynamo electric fields. An external dynamo is produced that creates dawn to dusk electric fields ( $E_{pc}$ ) that map down to the polar cap region. An internal dynamo is also produced that creates electric fields ( $E_a$ ) that, when mapped down to the polar cap, are reversed in direction, creating a dusk to dawn electric field. Figure 1.5 (Thayer, 1990) shows the location and direction of  $E_{pc}$  and  $E_a$  and the resulting wind pattern (black arrows) that develops around these electric fields.

These electric fields force ions into motion creating this two-cell ion convection pattern that flows anti-sunward in the polar cap with a sunward return flow on the outer boundaries. Due to ion-neutral collisional drag, or simply called ion drag, the neutrals are "dragged" along following this



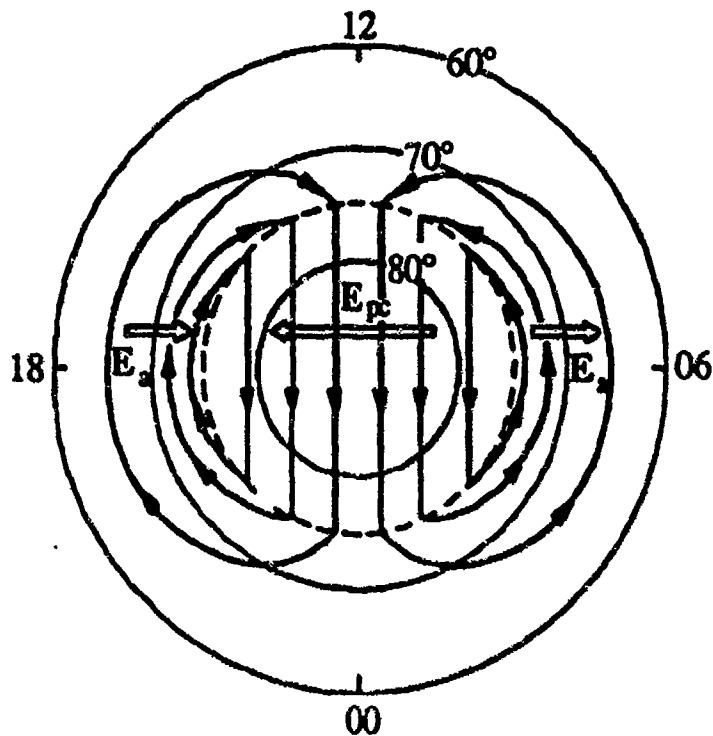


figure 1.5 Schematic of the resulting circulation cells from externally imposed electric fields (Thayer, 1990).

pattern. Neutral wind speeds in this pattern are normally 100-300 m/sec across the polar cap.

This pattern is generally oriented along the 0000-1200 local time meridian (Marcos, 1985). But during strong geomagnetic storms the pattern expands to lower latitudes, becomes more antisymmetric and can change its orientation. Neutral winds can also increase during these storms to over 1000 m/sec. The enhanced circulation pattern prevails for hours after a storm ceases (Marcos, 1985).

### 1.3 Aerodynamic drag

The total mass density and its variability is directly related to the atmospheric drag effect on satellites. Therefore, our ability to measure or model the mean density and its variability is important to the success of any satellite mission. Atmospheric drag should be taken into consideration for orbital lifetime, design and control, tracking and on-board fuel requirement (Marcos et al., 1989). Such empirical models as Jacchia-70 and MSIS have been and still are used successfully to estimate the impact of drag on satellites. However, accuracies of these models have remained at ~15% for the past two decades (Marcos, 1991). Soon, the VSH model will also be used for this purpose, but with improved accuracy and possibly in a forecast mode of operation.

Although there has been much research into the aerodynamic drag effect on satellites due to atmospheric density, there has been little study of the effect that winds by themselves have on satellite drag. Neutral winds directed opposite to that of the satellite velocity vector have the strongest drag effect on satellites, since the drag force is proportional to the square of the relative velocity.

Studies by Marcos [1985] have shown that the drag force on a satellite can increase by ~5% for every 200m/sec. This applies only if the winds are anti-parallel to the direction of the satellite. During geomagnetic storms, enhanced winds in the twin circulation cells can increase the drag on a satellite significantly.

I attempted to expand upon this study by determining the integrated drag/lift forces (along the orbit track) on a satellite due to neutral winds. I used a typical DE-2 orbit and computed neutral winds along the satellite track with the VSH model. It was found that 742 m/sec, anti-parallel winds changed the satellite drag by 23%.

The equation used to determine aerodynamic drag is similar to that used in section 2.4.2 but with a few assumptions:

$$F_D = \rho V^2 \quad (1.4)$$

The vector  $F_D$  represents the drag force and  $\rho$ , the total mass density.  $V$  is the atmospheric mass velocity,  $V_w$ , relative to the satellite velocity,  $V_s$ :

$$V = V_s - V_w \quad (1.4)$$

This is different from the expression in section 2.4.2 because we are making relative comparisons, so to simplify the parameterization in the FORTRAN program we assume all the other parameters (satellite frontal area and drag coefficient) are simply 1. The factor of 1/2 is also taken out for simplification.

I attempted to do more research in this matter, calculating the integrated drag along the satellite orbit, and determining exactly the contributions to drag in the polar cap region. However, due to time constraints I was required to cut the study short, providing only information on the increase in drag at particular points along the orbit.

## **CHAPTER 2**

### **DESCRIPTION OF TOOLS USED**

The following chapter provides background information on the devices used to conduct the VSH validation study. A short history on thermospheric general circulation models (TGCMs) is included since the VSH model is based on the output of the NCAR-TIGCM. And, of course, details on the techniques used in the VSH model are important in understanding the nature of the computer model's output. The MSIS empirical model is referenced by both TGCM and VSH models under various situations and is also used in this study comparing results to the SETA measurements. The SETA instrument and its measurements used in the validation procedure are explained also. DE-2 density measurements were also used to a small extent to possibly provide altitudinal comparisons of the models in the study. So background on the neutral atmosphere composition spectrometer instrument is also included.

#### **2.1 Thermospheric General Circulation Models (TGCMs)**

Historically, development of general circulation models has been limited due by the inability of computers to solve the primitive equations

associated with aeronomical applications in a timely, usable manner. After years of developing and using one dimensional, then two dimensional global thermospheric models, it was finally realized that to best simulate the thermosphere, a self-consistent three dimensional model that simultaneously solved the applicable conservation equations was needed.

The National Center for Atmospheric Research Thermospheric General Circulation Model (NCAR-TGCM) (Dickinson et al. 1981) and the University College at London Thermospheric General Circulation Model (Fuller-Rowell and Rees, 1980) were the first models to solve the three dimensional time dependent equations that used to describe the thermosphere. The NCAR-TGCM is based on a circulation model of the lower atmosphere, used in forecasting tropospheric weather, with added physical processes applicable to the upper atmosphere (Dickinson et al., 1981). The development and use of global circulation models like these has helped provide insight into the dynamics of the upper atmosphere.

The resolution of the NCAR-TGCM is  $5^{\circ}$  in latitude and longitude and has 24 pressure levels which covers altitudes from about 90 km to 500 km. The TGCM employs empirical and semi-empirical models and parameterizations to provide its output (Dickinson et al., 1981). Output includes neutral winds, temperature, and composition.

The dominant forcing of thermospheric processes is solar radiation in the extreme ultra-violet (EUV) and ultra-violet (UV) range. Dickinson et al. [1981] describes using solar EUV fluxes from Hinteregger [1981] and UV fluxes from Torr et al. [1980] to characterize the solar heating and photodissociation terms. To represent the electron density distribution from 90 to 500 km, the ionospheric model by Chiu [1975] was used (Dickinson et al., 1981). Neutral composition and temperature to calculate

the global average is taken from the MSIS empirical model from Hedin [1977] (Dickinson et al., 1981).

In recent years the original NCAR-TGCM has become more self-consistent, relying less on empirical models, and broadened its boundaries. A Thermosphere/Ionosphere General Circulation Model (TIGCM) has been developed that couples the dynamics between the two regions, alleviating part of the need for the Chiu [1975] model. Included in a recent version of the model are the effects of neutral constituents on ions and has led to the development of the Thermosphere/Ionosphere Electrodynamics General Circulation Model (TIEGCM). Finally, the extension of the model to include the chemistry and dynamics of the mesosphere will lead to the TIMEGCM (communication with R. Roble, 1991).

## **2.2 Vector Spherical Harmonic (VSH) Model**

The Vector Spherical Harmonic (VSH) semi-empirical model is based on output from the NCAR-TIGCM. Input needed to drive the VSH model include temporal, spatial and geophysical parameters (Killeen et al., 1991). The model was developed partly to give researchers a simple, relatively easy to use computer model of the global thermospheric structure that can run on a small computer. The basic idea of the VSH model is to take a spectral expansion in latitude and longitude of the gridded output from the NCAR-TIGCM using scalar and vector spherical harmonics (Thayer, 1990). Its use of vector spherical harmonics is where the model gets its name.

The specification of neutral density is very important in determining the atmospheric drag on artificial satellites. Historically, the accuracy of the prediction of neutral density has been limited to no better than 15%. The VSH model's goal is to reduce this error to 5% by using real-time satellite data to refine the model's output (Killeen et al., 1991).

VSH is referred to as a semi-empirical model because it employs output from the MSIS-86 empirical model for altitudes above 500 km and altitudes below 90 km.

The TIGCM output fields (winds, temperature and composition) are in 5 degree grids in latitude and longitude over 24 pressure levels vertically at selected Universal Times (UTs). A procedure is conducted on the TIGCM history file which performs the spectral expansion described above using vector spherical harmonics on the wind fields and scalar spherical harmonics on the temperature and composition output fields of the TIGCM. The coefficients, or "weighting factors", created due to this expansion are placed in a coefficient file. The coefficients are used by the VSH model, by various interpolation methods, to fit smooth curves over the TIGCM output fields to show variation in winds, temperature and composition with respect to the initial conditions. Inputs include temporal (UT), spatial (latitude, longitude) and geophysical conditions ( $A_p$ , solar flux) (Killeen et al., 1991). This procedure results in converting discrete gridded TIGCM output to continuous output used by VSH (Killeen et al., 1991).

The coefficient files mentioned above are placed in a coefficient library. The coefficient library is produced from a number of runs of the NCAR-TIGCM and are limited to keep the storage requirements at a minimum. These runs are based on a broad range of geophysical

conditions including seasonal variation, magnetic activity, and solar activity. A matrix of runs exist that cover three time periods over the year (June and December solstice and equinox conditions), three levels of magnetic activity ( $A_p$  values of 5, 11 and 32), and two levels of solar activity (low and high values of F10.7a and F10.7 to represent solar minimum and maximum) (Killeen et al., 1991), so there are presently 18 TIGCM runs in the coefficient library for use by VSH.

### 2.2.1 Spherical Harmonics

The following paragraphs describe the scalar and vector spherical harmonics used by the VSH model to convert the TIGCM history file to the coefficient files used by VSH to resynthesize output fields. More details on the mathematics of spherical harmonics can be found in Thayer [1990].

Since the earth is primarily spherical, one of the best ways to describe horizontal variations over the earth is by using spherical harmonics. This method helps alleviate the problem of discontinuities occurring over the poles as lines of longitude converge. A scalar quantity (e.g. density or temperature) can be described in scalar spherical harmonics at a particular location on a sphere from the sum

$$q(\theta, \lambda) = \sum_{m,n} a_{m,n} Y_n^m(\theta, \lambda) \quad (2.1)$$

where  $\theta$  is colatitude,  $\lambda$  is longitude,  $Y_n^m$  is the scalar spherical harmonic and  $a_{m,n}$  are the complex coefficients. The value  $Y_n^m$  can be expressed as:

$$Y_n^m(\theta, \lambda) = P_n^m(\cos \theta) e^{im\lambda} \quad (2.2)$$



with  $P_n^m$  being the associated Legendre functions

$$P_n^m(\theta) = \frac{1}{2^n n!} (\sin \theta)^m \frac{d^{(m+n)}}{dx^{m+n}} (x^2 - 1)^n; \quad x = \cos \theta \quad (2.3)$$

The top index  $m$  is the order or zonal wavenumber at a particular latitude and the bottom index  $n$  is the degree. The latitude wavenumber is determined by  $n-m$  (Thayer, 1990).

The vector quantity  $V$ , in this case the TIGCM output wind field, is expanded using vector spherical harmonics which has this form:

$$V = \sum_{m,n} (a_{m,n} P_{m,n} + b_{m,n} B_{m,n} + c_{m,n} C_{m,n}) \quad (2.4)$$

where  $a, b, c$  are the complex coefficients, and

$$P_{m,n} = \begin{bmatrix} P_n^m \\ 0 \\ 0 \end{bmatrix} e^{im\lambda}; \quad (2.5 \text{ a,b,c})$$

$$B_{m,n} = \begin{bmatrix} 0 \\ A_n^m \\ iB_n^m \end{bmatrix} \frac{e^{im\lambda}}{\sqrt{n(n+1)}};$$

$$C_{m,n} = \begin{bmatrix} 0 \\ iB_n^m \\ -A_n^m \end{bmatrix} \frac{e^{im\lambda}}{\sqrt{n(n+1)}}.$$

where  $A_n^m$  and  $B_n^m$  are related to the Legendre functions  $P_n^m$  by

$$A_n^m = \frac{dP_n^m}{d\theta} \quad (2.6 \text{ a,b})$$

$$B_n^m = \frac{m}{\sin \theta} P_n^m$$

(Killeen, 1987).

The complex coefficients that go into the library are computed by taking a least squares fit of the TIGCM wind output (Killeen et al., 1991). Then by putting these coefficients back into equation 1.4, the global wind field can be resynthesized with continuous output (Thayer, 1990).

### 2.2.2 Interpolation Methods

The curves described above are not only fitted through a single TIGCM run but can also be fitted across different TIGCM runs, such as the manner solar flux values are interpolated, to better represent the initial conditions. The interpolation methods used by VSH are described in the following paragraphs.

The interpolation method used to represent vertical structure is a cubic spline, which is a piecewise polynomial (Killeen et al., 1991). The vertical structure of the atmosphere varies greatly due to physical processes that occur at different altitudes. The vertical profiles of density and temperature vary significantly between 100 km and 500 km.

Near 100 km, where the turbopause exists, density falls off in a uniformly exponential manner below the turbopause. Above the turbopause, the individual chemical species begin to separate and their density drops off depending on their individual mass. Near this same altitude at the mesopause the temperature of the atmosphere is at its coldest and quickly increases to its maximum near 500 km.

In the VSH model cubic splines are used in the altitude range from 110 - 500 km. Above that altitude temperatures from the MSIS model are

used. Coefficients of the polynomial are different for each subinterval of the altitude range (Killeen et al., 1991).

A Fourier time series is used to reproduce diurnal, semidiurnal, and terdiurnal variations. A Fourier representation assumes a periodic nature of that field. This is generally true, for example, for diurnal tides, but during magnetic storms, fields can vary significantly before returning to a normal state. Plans exist to implement the use of a spectral fit for magnetic storm cases (Killeen et al., 1991).

The Fourier series used is expressed as:

$$a_{m,n,s} = \frac{a_{0,m,n,s}}{2} + \sum_{k=1}^T a_{k,m,n,s} \cos kt + \sum_{k=1}^T b_{k,m,n,s} \sin kt \quad (2.7)$$

For  $T=3$  this represents a constant term, three symmetric coefficients, and three antisymmetric coefficients (diurnal, semidiurnal, and terdiurnal) (Killeen et al., 1991).

To account for seasonal variations over the year a trigonometric interpolation method is used. Solstice and equinox conditions due to the annual solar cycle are represented by a sinusoidal curve of the radiation absorbed by the earth (Killeen, et al., 1991).

Previously, the VSH model used only the F10.7 solar EUV proxy in representing solar flux variations (Killeen, 1991). As mentioned before, solar EUV and UV radiation affects thermospheric dynamics greatly, so a good representation of solar flux is very important to the VSH model. During the model validation process described in chapter 3, VSH model density was noticed being greatly overestimated under certain conditions. It was discovered that this overestimation was occurring during times of

strong solar flux, or high F10.7 values. A better representation of solar flux was needed.

The F10.7a value (the 81 day running average) is very important in describing low altitude dynamics, while the daily solar flux value, F10.7, is more important in the higher altitude region. A parameterization combining the effects of these two values into one value, F10.7', is used to take into account this height dependence

$$F10.7' = F10.7a + k_1(h) \cdot (F10.7 - F10.7a) + k_2(h) \cdot (F10.7 - F10.7a)^2 \quad (2.8)$$

Here  $k_1$  and  $k_2$  are height dependent coefficients derived from the MSIS model. The weights increase monotonically with height thereby giving more importance to the F10.7 value at high altitudes. This parameterization corrected the density overestimation and resulted in improved density output.

Geomagnetic activity is indexed by the  $A_p$  value. Since the  $A_p$  index is a linear measure of the magnetic activity, variations of magnetic storm activity are represented by a linear interpolation across  $A_p$  (Killeen et al., 1991).

### 2.2.3 Truncation

One of the important precepts of the VSH model is to retain the high latitude resolution feature of the TIGCM output fields (e.g. the vector wind fields) but keeping the coefficient library down to a manageable size. This is done by truncating the coefficients by a certain amount which is dependent on the indices  $n$  and  $m$ . To get good resolution from the spherical harmonics the latitudinal wavenumber ( $n-m$ ) must be

considerably larger than the zonal wavenumber ( $m$ ) as in describing the latitudinal variations of the wind fields at high latitudes (Thayer, 1990). This makes sense physically since most of the variability in a wind field, for instance, occurs latitudinally.

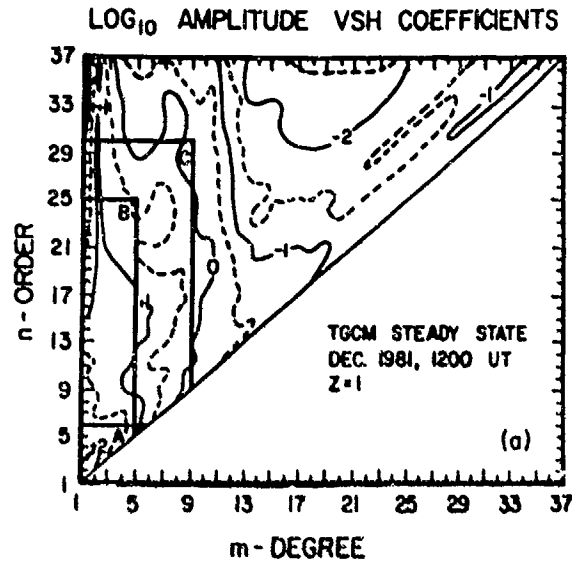


figure 2.1 Contours of the logarithmic amplitude of the vector spherical harmonic coefficients with the three different levels of truncation (Killeen, 1987).

Figure 2.1 describes the distribution of power (amplitude) in the VSH spectral coefficients for a steady state TGCM run, under the conditions stated in the figure, where the pressure level  $Z=1$  corresponds to a height of  $\sim 350$  km (Killeen et al., 1987). This is a plot of the order ( $m$ ) versus the degree ( $n$ ) of the harmonic. The lower right section is unfilled since only the values  $n > m$  are nonzero. It can be seen that most of the power lies in the lower wavenumbers but is also relatively high latitudinally. The power,

or importance, of the coefficients decreases rapidly with variation in longitude. Therefore, to have good resolution at the high latitudes, the most important coefficients to keep are with respect to the degree  $n$  and less important with respect to the order  $m$ . The best level of truncation was determined to be for values of  $n \leq 25$  and  $m \leq 5$  (Killeen et al., 1987), which is level B in the figure. This maintains good resolution, showing the high latitude neutral wind patterns, while cutting down the size of the coefficient files (Thayer, 1990). Semi-empirical models such as MSIS truncate coefficients at level A (Hedin, 1983). Level C would result in excellent representation of neutral wind fields but at a cost of storage space (Killeen et al., 1987).

When using a rectangular truncation, even after choosing optimal values of  $n$  and  $m$ , undesirable coefficients are included due to the nature of the contours. To only attain the coefficients desired, the more logical means of truncating would be to follow the path of the desired contour, which also results in optimizing required storage space. This will be the method of truncation for future versions of VSH (private communication with M. Minnock).

### **2.3 Mass Spectrometer-Incoherent Scatter (MSIS) empirical model**

There are a large number of models that simulate different aspects of the thermosphere. Most of them are based on data taken from in situ measurements by satellites, rocket borne instruments, or ground based instruments such as incoherent scatter radars. These empirical models have been very good at organizing large data bases to be used in theoretical work and comparing other data. One of the first of such models was

developed by Jacchia [1965] which inferred total densities from satellite drag. Other models were developed using temperature data from incoherent scatter radars (Carru et al., 1967). But no model had been produced that provided a combination of thermospheric parameters until MSIS-77 (Hedin, 1977).

The MSIS empirical model is arguably the most widely used model for thermospheric research. It uses data taken from all the methods mentioned above. The version used in this study, MSIS-86, uses data taken from eight satellites, numerous rocket probes, and five ground-based incoherent scatter radar sites (Hedin, 1987).

The MSIS model currently provides information on temperature, density, and composition of the atmosphere from the upper mesosphere to the upper thermosphere. This information is also provided for a large range of solar activity and magnetic activity, for seasonal, geographical, and UT effects.

Data is sorted into bins based on latitude, local time, day of year, UT, Ap, F10.7, and altitude. It is then expanded using spherical harmonics to tie in all the different data sets by spatial, temporal, and geophysical conditions (Hedin, 1987).

A Bates model temperature profile is used for the upper thermosphere. An inverse polynomial (Hedin, 1987) is used in the lower thermosphere since this is the region where the atmosphere changes from mixing to diffusive equilibrium and a simple profile does not model this area well. These methods are used to determine the density profile with respect to geographical and solar/ geomagnetic parameters (Hedin, 1987).

The expansion mentioned above produces coefficients that are used to fit curves over different data sets. In Hedin [1977] the coefficients are

determined by the 120 km temperature, 120 km N<sub>2</sub> density, and the exospheric temperature for both quiet and active magnetic cases.

MSIS has coverage over a large range of solar activity, with F10.7 values between 70 and 200 (Hedin, 1983). Representation over magnetic activity has also improved by using the ap, or 3 hourly, geomagnetic index as opposed to using the daily Ap value (Hedin, 1983).

With the inclusion of temperature and composition data from the Dynamics Explorer satellite, MSIS has improved its representation of the high latitudes for solar maximum conditions (Hedin, 1987). However, calibration problems in the instrument on the DE-2 satellite that measured total density resulted in making the data unreliable and a fitting parameter was required (Hedin, 1987).

Such models as MSIS are good at accurately assessing density during quiet geomagnetic activity at low latitude regions (with errors ~12-15%) but during geomagnetic storms at high latitudes, uncertainty in densities reach ~50% (Killeen et al., 1988). The above 12-15% accuracies currently exist as a limit to the ability of such models. Even additional data sets such as the use of density and temperature measurements from the Dynamics Explorer does not improve accuracy (Killeen et al., 1988). This boundary is due to the inherent accuracy of the sensors used to gather data, possible errors in the analytical procedures used to interpolate data and limited data coverage (Killeen et al., 1988).

Another, more important, limitation to the MSIS model in particular is the temporal and spatial resolution of this model. The temporal resolution is limited by the use of the 3-hourly ap geomagnetic index (Hedin, 1987). It is known that magnetic disturbances can occur well within this time frame (Killeen, et al., 1988). Also, the spatial resolution is



limited by the level of harmonics used by such empirical models (Killeen et al., 1987).

As mentioned in section 2.2.3, level A in figure 2.2, is the typical level of truncation used by empirical models such as MSIS (Thayer, 1990). This level controls the extent of the resolving capability of the model and subsequently, the accuracy the model may attain. This limitation in accuracy primarily affects the representation of the high latitude region where there is a large amount of structure (ie. density enhancements) occurring over small distances.

Until the Dynamics Explorer 2 satellite provided a large data base of global thermospheric winds, no empirical model for such winds had been created (Hedin et al., 1988). Previous wind data from ground-based optical instruments, incoherent scatter radar sites, and rocket chemical releases did not provide adequate global coverage. In addition to DE-2 data, winds from satellite-based accelerometers (Marcos and Forbes, 1985) have recently been available.

As a result of the availability of this recent data an empirical horizontal wind model (HWM-87) has been developed (Hedin, 1988) that provides global winds for the upper thermosphere. This model uses wind data from two satellites, and is analogous to the MSIS model (Hedin, 1988). The DE-2 provided in-situ zonal wind measurements from the wind and temperature spectrometer (WATS) and remotely sensed meridional winds from the Fabry-Perot Interferometer (FPI) (Hedin et al., 1988). The Atmosphere Explorer E (AE-E) satellites also supplied meridional and zonal winds from the NATIE instrument (Hedin et al., 1988).

Due to the data available, the model is limited to altitudes above 220 km, and contains no F10.7 effects. However, effects due to magnetic

variability are available. Similar to MSIS, data was sorted based on latitude, local time, day of year, UT, Ap, and F10.7 (Hedin et al., 1988). An expansion using vector spherical harmonics creates coefficients for the spatial representation. No altitude dependence is included due to the limited data and theory suggests (Rishbeth, 1972) that viscosity in the upper thermosphere reduces vertical wind shears, so a vertical wind profile is not as important.

The HWM only roughly depicts the neutral wind circulation pattern in the polar region, but low- and mid-latitude winds compare well with ground-based measurements (Hedin et al., 1988).

#### **2.4 SETA-2 instrument**

The data set used in this validation study is composed of in-situ total mass density measurements from the Satellite Electrostatic Triaxial Accelerometer (SETA) instrument. It was flown on a low altitude satellite with an 83 degree inclination during 1982. This instrument has provided an extensive data base of total density measurements of the lower thermosphere.

The original accelerometers were single axis systems flown successfully on several satellites such as the AE-C, -D and -E satellites. This instrument was called the Miniature Electrostatic Accelerometer (MESA) and since it was only a single axis system, three mutually perpendicular sensors were required to provide a triaxial sensing capability. The MESA system weighed 10 kg and required 20 W of power (Marcos and Swift, 1982). The SETA instrument was an improvement over the MESA by weighing less (4.6 kg) and requiring less power (11.7 W).

### 2.4.1 Operation

As its name suggests, the SETA instrument has a triaxial sensing capability as the MESA system, but is accomplished within one sensor. The instrument is capable of measuring total mass density and cross-track winds from acceleration measurements (Marcos and Forbes, 1985). The instrument electrostatically suspends a proof mass within a hollow cylinder along its radial axis. The Z axis is along the center of the cylinder and the X and Y axes are perpendicular to the cylinder. Each of the axes have a pair of electrodes that act to constrain the proof mass (see figure 2.2a,b).

Accelerations along each of these axes are measured by sensing motion in the proof mass and applying an electrostatic force on the appropriate electrode that acts to restore the proof mass to its initial position (Marcos and Swift, 1982). In this way the dc voltage required to restore the proof mass is proportional to the acceleration. The subsequent output of the sensor is a digital pulse rate in proportion to the input acceleration (Marcos and Swift, 1982).

The accelerations that must be measured are very small, so the instrument sensitivity range is from  $1.2 \times 10^{-3}$  g to  $1 \times 10^{-6}$  g. However, accelerations as low as  $2 \times 10^{-9}$  g can be sensed when on the most sensitive scale of the unit (Marcos and Swift, 1982). The instrument stores digital pulses for a 2.045 s sample period and provides the average acceleration over this period as the output.

The instrument is calibrated against a portion of the earth's gravity field by tilting the instrument slightly from the horizontal, zero position

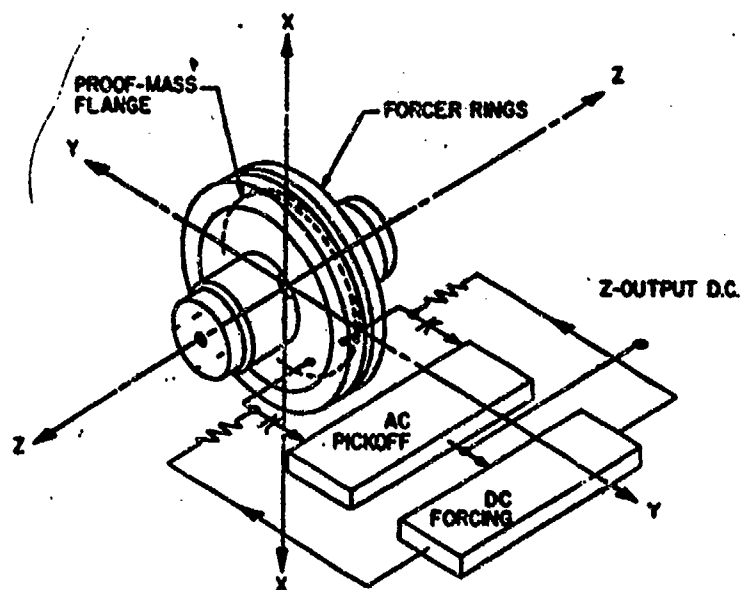


figure 2.2a Diagram of the Z-axis Force Rebalance Loop (Marcos, 1982).

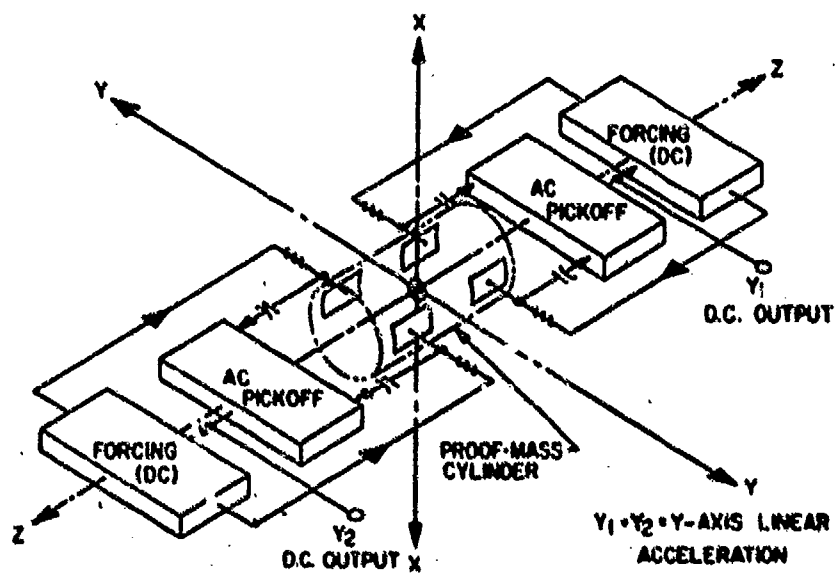


figure 2.2b Diagram of the Y- (or X-) axis Force Rebalance Loop (Marcos, 1982).

(Marcos and Swift, 1982). The calibration is limited by a means capable of measuring very small changes in angular displacement; a laser interferometer is used that allowed for a measurement as low as  $10^{-7}g$ .

The instrument is mounted on the satellite so that its Z axis corresponds to the satellites in-track direction, the Y axis is situated along the earth's radial direction, and the X axis the cross-track direction.

## 2.4.2 Data

Typical plots of the data represent X,Y, and Z axis accelerations vs time and is illustrated in figure 2.3. The Z axis plot represents satellite

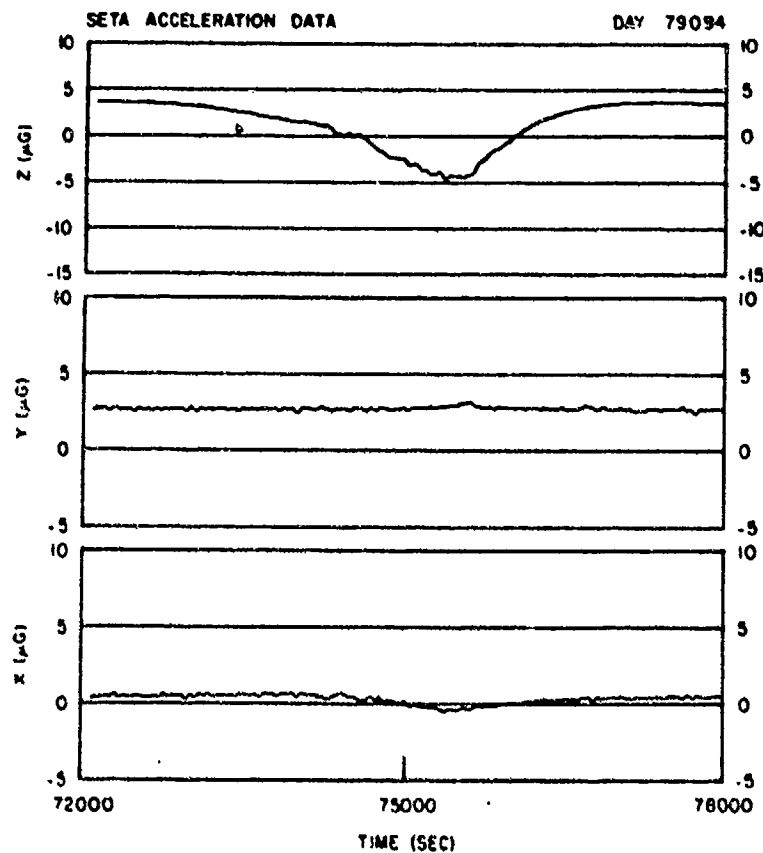


figure 2.3 Filtered data from accelerometer (Marcos, 1982).

drag and reaches a maximum ( $\sim 8\mu\text{g}$ ) at the perigee where the density is highest. Since atmospheric drag opposes the direction of the satellite, accelerations are negative and therefore, maximum densities correspond to more negative accelerations and minimum densities correspond to less negative accelerations (Marcos and Swift, 1982).

Plotted accelerations along the Y axis represent forcing radially away from the earth with spikes coming from the pitch-attitude thrusters on the satellite. The plot for the X axis shows the effects of cross component winds (corresponding to zonal winds at low and middle latitudes and meridional winds at high latitudes since the satellite is not in a perfectly polar orbit).

The raw data has contributions from vehicle dynamics,  $a_v$  (spacecraft vibrations) and instrument operating characteristics,  $a_b$  and  $a_N$  (bias and random noise) as well as atmospheric drag and wind accelerations (Marcos and Forbes, 1985). The 2.045 s averaged instrument output ( $a_T$ ) is therefore expressed as

$$a_{Ti} = a_{Di} + a_{vi} + a_{bi} + a_{Ni} \quad (2.9)$$

where the  $i$  represents the three axes, X, Y, and Z. Solving for  $a_{Di}$ , the aerodynamic component

$$a_{Di} = a_{Ti} - (a_{vi} + a_{bi} + a_{Ni}) \quad (2.10)$$

we get the acceleration due to aerodynamic drag which is related to total atmospheric density.

Unwanted contributions from spacecraft vibrations,  $a_v$ , and instrument noise,  $a_N$ , are removed by numerical filtering techniques (Marcos and Swift, 1982). The bias value  $a_b$  is different for each orbit and

was removed by fitting a line to average bias values for 22 days for each of the axes (Marcos and Swift, 1981).

Once the corrected acceleration term is determined, atmospheric density and wind velocities are calculated by the expression

$$a_{Di} = \frac{A_{ref}}{2m} C_i \rho V^2 \quad (2.11)$$

The values  $i$ ,  $a_{Di}$  and  $\rho$  are the same as in previous expressions.  $A_{ref}$  is the satellite frontal area,  $m$  is the satellite mass,  $C_i$  are the drag coefficients with respect to the three axes velocities.  $V$  is the atmospheric mass velocity relative to the satellite and is determined by

$$V = -V_G + V_A + V_w \quad (2.12)$$

where  $V_G$ ,  $V_A$ , and  $V_w$  respectively gives the velocities for the satellite's inertial reference frame, atmospheric rotation, and neutral wind (Marcos and Swift, 1982).

The components for the drag coefficient are calculated using the results from Sentman [1961]. The drag coefficients for each axis is calculated and plotted as a function of pitch angle in figure 11 of Marcos and Swift [1982].

An iterative technique is used to solve equation 2.11 since there are more unknowns ( $\rho$ ,  $V$ ) than equations. An initial estimate of density is determined and used to calculate the three velocity components (Marcos and Swift, 1982). The density estimate is refined by using a new  $V$ , and in turn until an acceptable error is reached (Marcos and Swift, 1982).

Accuracy of the instrument is limited by accelerometer bias, attitude uncertainties, drag coefficient estimates, instrument noise not filtered out,

and the inability to separate wind and density effects along the in-track axis (Marcos and Swift, 1982). However, attitude errors are comparatively small, and those due to bias and noise are  $\sim 0.5\%$  at low altitudes (170 km) and climb by a factor of five at higher altitudes (220 km). The drag coefficients and wind uncertainty contribute the primary error in density and are within  $\pm 5\%$  each. Accelerometers, therefore, provide the most accurate means of measuring total density at these low altitudes.

### 2.4.3 Orbital characteristics

The SETA-2 instrument was flown on a low altitude satellite with an apogee of 260 km and perigee of 170 km. The data set used in this study provided total mass density (in  $\text{g/cm}^3$ ) measurements between May and July 1982. This time period was near solar maximum conditions for solar cycle 21. The set consisted of a measurement every 20 seconds totalling 186,814 data points over 1369 orbits.

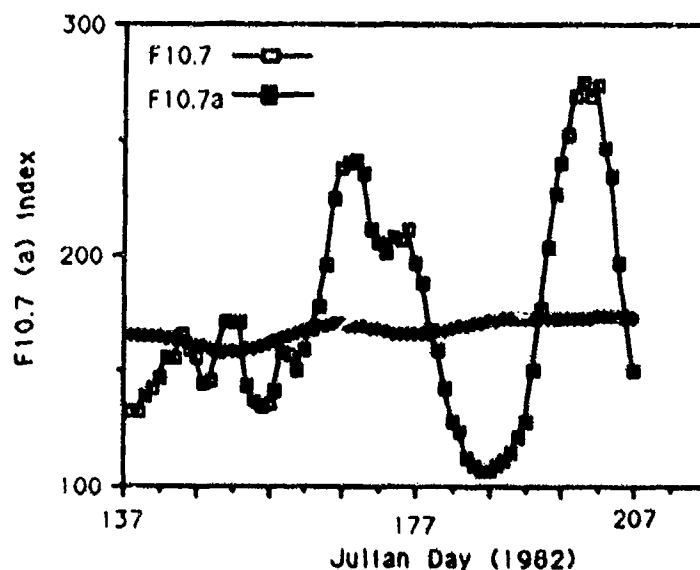


figure 2.4 F10.7 and F10.7a values during the SETA-2 period.



Figure 2.4 and 2.5 shows the F10.7 and F10.7a, Ap and Kp indices for the time period of the data set. The indices show that there were a number of geomagnetic disturbances during this time, providing ample data for a broad range of magnetic activity in order to study this aspect of VSH and MSIS.

The orbit of the satellite took it through an almost constant local time meridian (10-22 LT) throughout the whole data set with apogee being in the night sector and perigee in the day sector. This obviously puts a local time bias on the results of the study. However, the amount of data available and time of coverage still provides a good statistical distribution to make meaningful comparisons with VSH and MSIS.

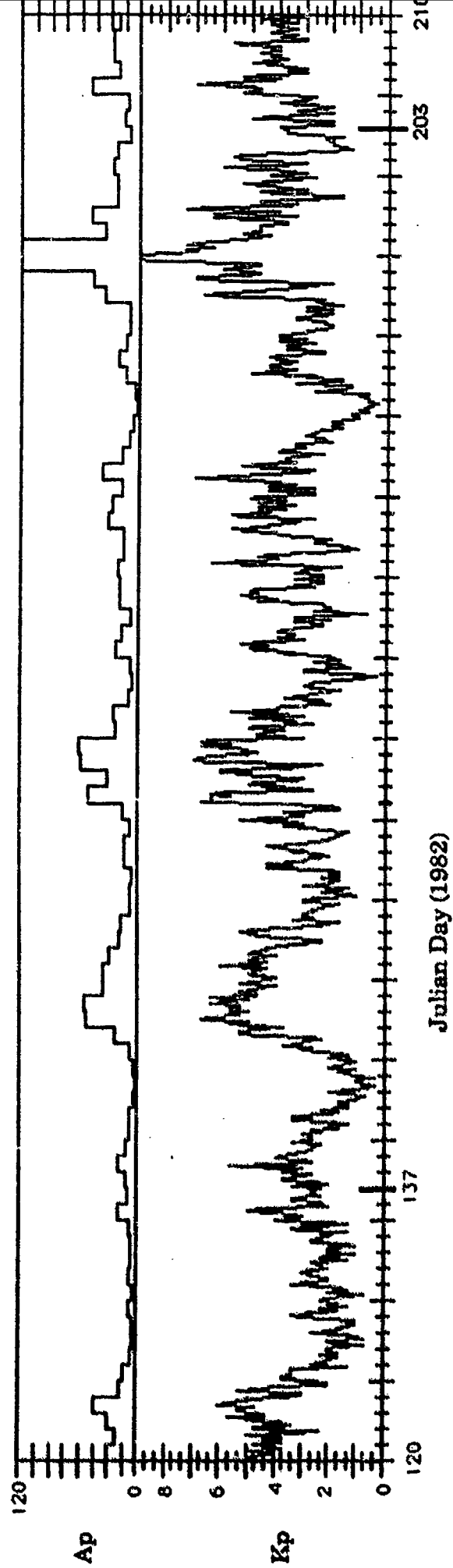


figure 2.5 Geomagnetic parameters during the SETA-2 period (137-203).

## 2.5 Dynamics Explorer NACS instrument

The Dynamics Explorer program was developed to study interactions between the magnetosphere, ionosphere, and the atmosphere. The program provided for two coplanar satellites with an inclination of 90 degrees and with different altitudes. Satellites DE-1 and 2 were launched in 1981. The high altitude satellite (DE-1) was used for global auroral imaging, plasmasphere and plasmopause observations, and magnetic measurements (Hoffman and Schmerling, 1981). The low altitude satellite (DE-2) had a perigee of 305 km and an apogee of 1300 km and was used to provide neutral particle and wind measurements. Orbital characteristics of the DE-2 satellite were determined so that perigee went from pole to pole in less than two months since the emphasis was on polar phenomena (Hoffman et al., 1981).

The relevant satellite for my research is the DE-2 satellite. Instruments from this satellite give neutral atmosphere density and wind data which complement the lower altitude measurements from the SETA-2 instrument. By comparing measurements from these two satellites it is conceivable to evaluate the height dependence of the VSH model.

One of the nine instruments on this satellite is the neutral atmosphere composition spectrometer (NACS). This instrument measured similar parameters of the neutral atmosphere, but in slightly different methods in order to provide a redundancy in measurements.

### 2.5.1 NACS instrument

Density is the NACS instrument's primary objective. Instruments similar to this one were flown on the AE-C, -D, and -E satellites giving good results. It uses a quadrupole mass spectrometer to measure abundances of O, N<sub>2</sub>, He, and Ar in the 300-500 km range.

The closed source mode is employed allowing the particles to come in chemical and thermodynamic equilibrium. By using this method, chemically reactive species such as atomic oxygen are determined indirectly by measuring the species in some reacted form (ie. molecular oxygen).

Particles enter the antechamber of the sensor where they are allowed to collide with the walls before being ionized and measured. This enhances the particle density as they cool from 1000 K to 300 K (temperature of the sensor) and results in improved sensitivity in the detection of low concentration particles such as He and Ar in these altitude regions (Carignan et al., 1981). The particles are then ionized by electron bombardment in the ion source region of the sensor and are focused onto the aperture of the quadrupole. The quadrupole consists of four long rods with appropriate potentials applied to allow mass selection with a resolution of 1 amu. The range for detection is from 2 to 50 amu. The ions then have individual mass to charge ratios and only ions with the selected ratio move down the rods to be detected by an electron multiplier.

Mass numbers are selected into eight 0.016 s intervals and the sequence is repeated every 0.128 s. Combinations of mass selection can be used to allow for a particular investigation such as the He to Ar ratio. Mass 4 could be selected for two intervals and mass 40 in the other six. The eight interval mass selection means that a sweep of the masses from 1-25 can be accomplished in 2 seconds (Carignan et al., 1981).

Problems in instrument calibration resulted in no absolute calibration error being determined (A. Burns, private communication). Instrument measurements drifted from month to month with probable error exceeding that of the SETA instrument measurements, and more closely approaching model errors. Subsequently, comparisons between model and NACS data are difficult to interpret.

## 2.5 Statistical Techniques

One important aspect of the validation study is the statistical method used to validate the model output. In choosing the method a number of items were taken under consideration. Obviously, we wanted to compare VSH density output to the satellite measurements, but also wanted an objective comparison of VSH with another model such as MSIS. We also had a large data set to make good statistical comparisons.

The most simple way of comparing two values is by taking the average relative error, or the percent difference between them. This is expressed mathematically by

$$\epsilon = \frac{\rho_{\text{model}} - \rho_{\text{seta}}}{\rho_{\text{seta}}} \times 100. \quad (2.13)$$

We define  $\epsilon$  to be the percent difference of the model (VSH, MSIS) and total mass density output,  $\rho_{\text{model}}$ , relative to the total mass density measurements by the SETA instrument,  $\rho_{\text{seta}}$ .

A one to one comparison, using equation 2.13, is taken between the model output and the measurements for each point in the SETA data set. A

frequency distribution is produced by summing over the percent differences. The resulting curve is a probability distribution.

The subsequent plots generated illustrate the percent difference between the models (VSH and MSIS) and the SETA measurements versus the respective frequency of occurrence. Therefore, two frequency distribution curves are shown, one for VSH and the other for MSIS. Figure 2.6 illustrates the format for the plots where the horizontal axis is the percent difference, or "error", from SETA values, and the vertical axis is the frequency (or number of counts) at a specified error. The 0 point is the "true" (SETA) value and the areas of negative (positive) percent difference is where the model underestimates (overestimates) the SETA density.

The natural way of fitting a frequency distribution is by using a Gaussian distribution. The Gaussian distribution is an approximation to the Binomial distribution for the special case where the number of data points is very large and the probability of success is very good (Bevington, 1969). This certainly describes our case since there are almost 200,000 data points and the percent differences, of the model output, from SETA data are relatively small.

The equation for a Gaussian distribution is

$$P_G(x, \mu, \sigma) = \frac{1}{\sigma\sqrt{2\pi}} \exp\left[-\frac{1}{2}\left(\frac{x - \mu}{\sigma}\right)^2\right] \quad (2.14)$$

Figure 2.7 shows the symmetric Gaussian "bell" curve about a mean,  $\mu$ , with standard deviation,  $\sigma$ . The width of the curve,  $\Gamma$ , is represented by the full-width at half-maximum. The tangent to the curve at  $\Gamma$  drawn to intersect the horizontal axis locates the value for two standard deviations (Bevington, 1969).

The "weighted" mean of the Gaussian is calculated by

$$\mu = \frac{\sum_{i=1}^n x_i f_i}{\sum_{i=1}^n f_i} \quad (2.15)$$

where the summation is over the whole data set  $n$ , from -100 to +100 percent difference  $x$ , and the frequency  $f$  at each  $x_i$  (Bevington, 1969). The denominator is the area bounded by the distribution curve and is therefore a normalization factor to make the sum of the probabilities equal to 1. The next parameter needed to calculate the Gaussian is the standard deviation (Bevington, 1969), which is the square root of the variance,  $\sigma^2$ :

$$\sigma^2 = \frac{\sum_{i=1}^n [(x_i)^2 f_i]}{\sum_{i=1}^n f_i} - \mu^2 \quad (2.16)$$

Where all values are the same as in equation 2.14.

The standard deviation is a measure of the dispersion about the mean, and is also proportional to the uncertainty in determining the mean of the distribution (Bevington, 1969). Therefore, the standard deviation is the primary statistical value used to make comparisons of VSH with MSIS.

One term that is used a number of times to describe the appearance of a frequency distribution curves is skewness. As defined by Press et al. [1986], "skewness characterizes the degree of asymmetry of a distribution around its mean. It is a pure number that characterizes only the shape of the distribution." Figure 2.8 (Press et al., 1986) illustrates positive and negative skewness, where positive skewness indicates a distribution with a

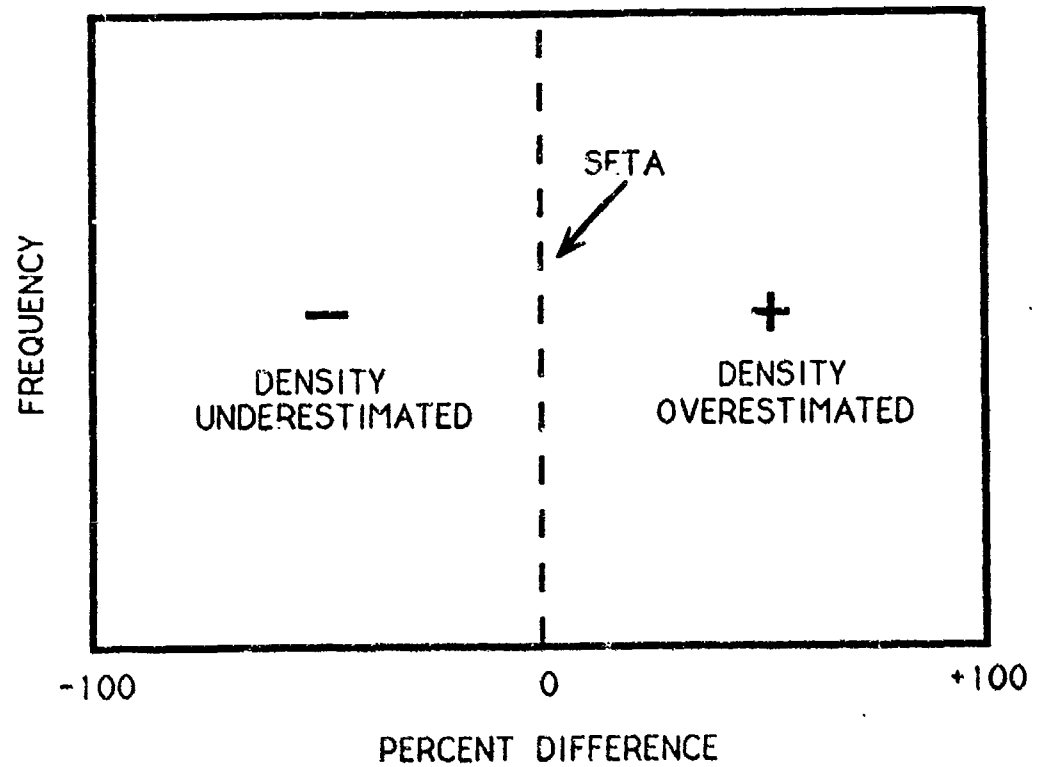


figure 2.6 Format: used for model to data comparisons.

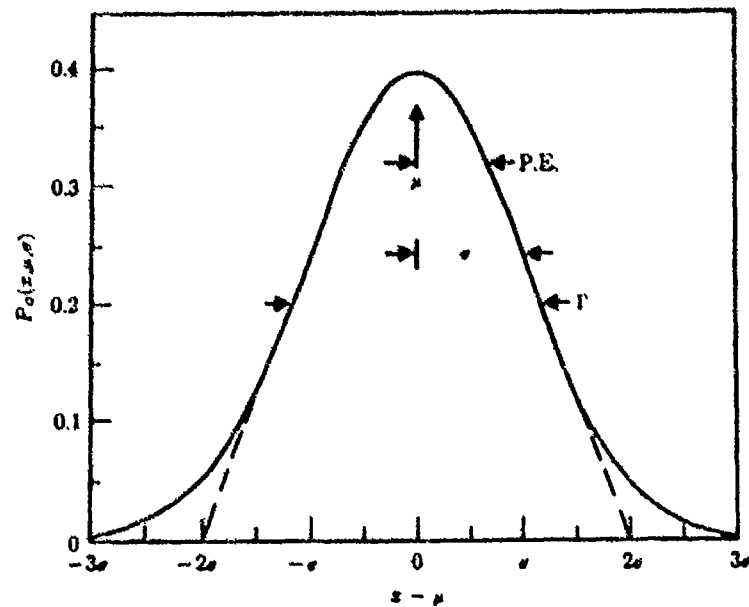


figure 2.7 Gaussian probability distribution with the mean and standard deviation values shown.



tail that extends towards positive values of  $x$  and a negative skewness indicates a tail that extends towards negative values of  $x$ . The effect of skewness on the plots in chapter 3 is to shift the mean value and sometimes increase the dispersion about the mean.

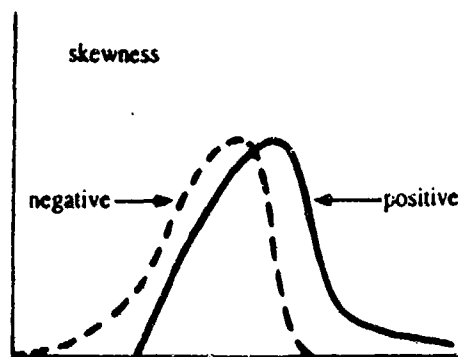


figure 2.8 Graphic illustration of skewness.

Problems were noted in using a Gaussian to fit some of the curves. In some cases the VSH frequency distribution was bifurcated or spread out across large errors. The bifurcation was noted in an earlier version of the VSH model and the dispersion was noted when insufficient data existed to compare with the models. In these cases the frequency distribution was distinctly non-Gaussian and the standard deviations calculated were not good indicators to make comparisons between VSH and MSIS.

However, this method has been used extensively in previous studies to make statistical comparisons (Marcos et al., 1989; Marcos, 1991) and it was necessary to continue its use in this study to show an historical progression in comparisons with other models in these studies.

In future validation studies a more applicable statistical method is recommended. A modification to the current method would be to weight each of the percent difference values based on their difference from the maximum frequency in the mean value calculation. A value close to the maximum value would have a higher weight than one further away. This would make the Gaussian mean match more closely with the parent frequency distribution maximum frequency value.

## **CHAPTER 3**

### **VALIDATION STUDY RESULTS**

#### **3.1 Introduction**

The previous two chapters provide the necessary background for the results of the validation study included in this chapter. This chapter includes a number of plots that are based primarily on SETA-2 measurements and to a lesser extent on NACS measurements (from the DE-2 satellite) and show certain dependences of the VSH model. NACS measurements were included in an attempt to evaluate the altitude dependence of the model. Section 3.2.1 includes the results from the systematic process used to discover a significant shortcoming in the VSH model and an explanation of the subsequent changes to the model. Model to model comparisons are then made between the updated version of VSH and the MSIS empirical model in section 3.2.2.

#### **3.2 Comparison of VSH and MSIS to SETA-2**

A general comparison was first made between the models and the whole SETA-2 data set (with no data binning) to get an overall impression of

the VSH model's performance. Figure 3.1 illustrates this overall plot. The horizontal axis is the average relative error, or percent deviation from SETA-2 measurements and the vertical axis is the frequency or number of counts. In all of the following plots the smooth dark lines are the Gaussian fits to each of the model's frequency distribution and the model standard deviation and mean values are indicated in the upper right hand corner.

It was noticed during this study that in a number of cases the Gaussian fits do not fully represent the frequency distributions. Although the Gaussian fits are good at showing model trends and relative comparisons between the models, in these cases the distributions are simply non-Gaussian. However, the method for calculating the standard deviation and mean have been used in past studies by Marcos [1989] to make comparisons between the Jacchia and MSIS models. Therefore, in order to make meaningful comparisons between the current VSH model and the other models in past validation studies I have continued using this statistical method.

### 3.2.1 Discovery of F10.7 dependence

Figure 3.1 is for an early version of VSH and was instrumental in giving us our first indication that a significant shortcoming existed in the model. The VSH curve is distinctly non-Gaussian, with a prominent "leg" extending from ~15% well into high positive values (indicative of a positively skewed distribution) which indicates the model is overestimating density under certain conditions. Previous validation studies showed no indication of this skewness because the comparisons were made with data over

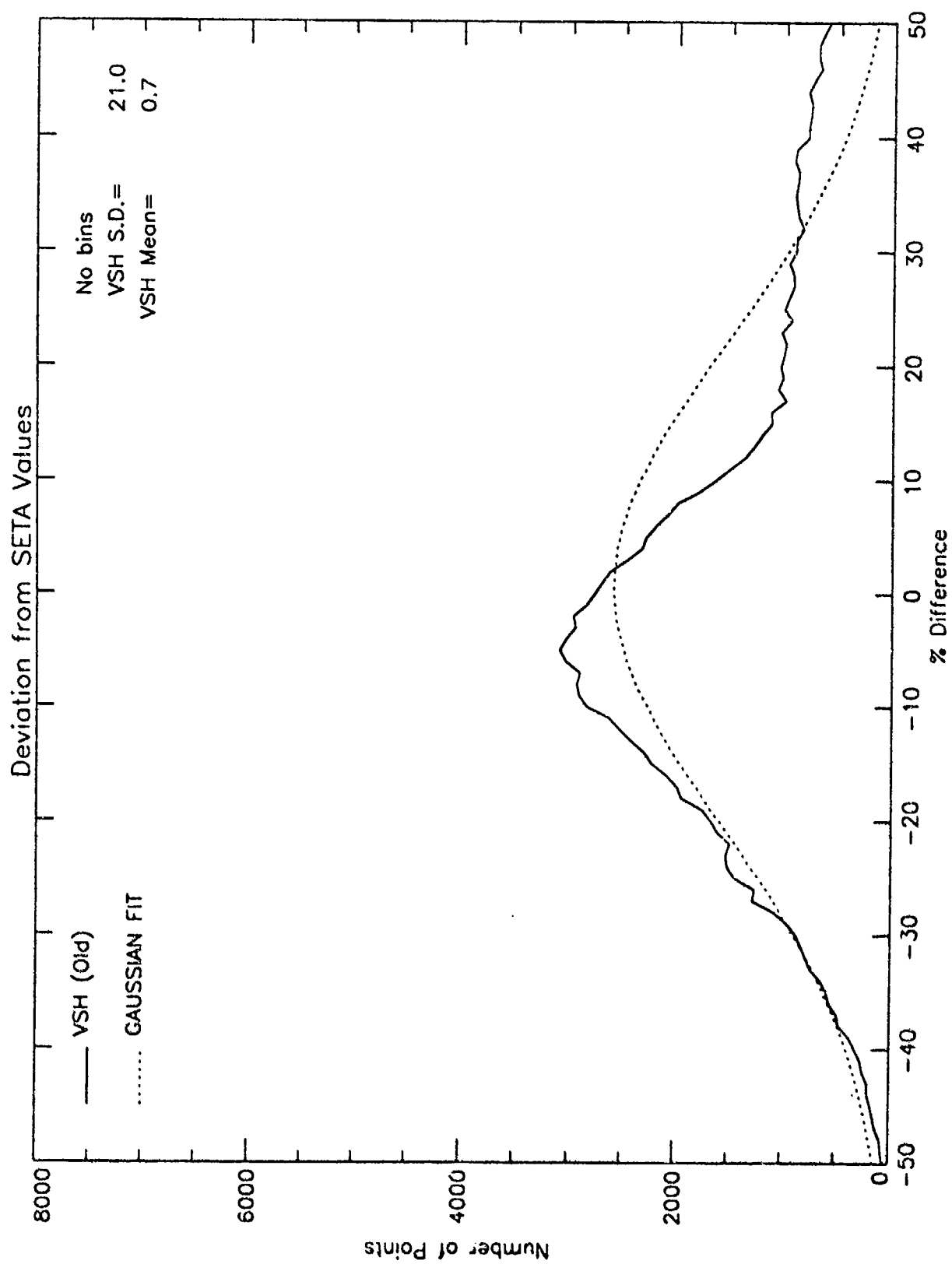


figure 3.1 Overall plot of old VSH deviations from SETA values.

relatively short time periods, whereas the data set used in this study covers 70 days.

In order to systematically investigate the performance characteristics of the model and determine the conditions for which the VSH model is overestimating density, the SETA-2 data was binned into low ( $0 \leq Kp < 3-$ ), medium ( $3- \leq Kp < 4+$ ) and high ( $4+ \leq Kp < 9$ ) Kp indices.

Figures 3.2 represent deviations from SETA-2 measurements for the three magnetic activity levels. The low Kp case shows VSH being skewed towards positive values and in the medium Kp case even more skewed with a larger area of overestimation. The VSH curve in the high Kp case again shows a wide area of overestimation, but now the curve begins to show a distinct bifurcation, or secondary maximum.

Next, to check for latitude dependence, the data was binned into six 30 degree latitude intervals in addition to the Kp bins. The top three plots on the page in each of figures 3.3-3.5 are for the northern hemisphere and the bottom three plots are for the southern hemisphere. From left to right the latitude intervals indicate high-latitude  $\pm(60^\circ-90^\circ)$ , middle-latitude  $\pm(30^\circ-60^\circ)$ , and equatorial  $\pm(0^\circ-30^\circ)$  regions.

Figure 3.3 illustrates the latitudinal dependent low Kp case. VSH continues to show the positive skewness, but now the data is becoming even more bifurcated, with small secondary and even tertiary maximums evident. In all cases, however, the primary peak is very close to the SETA-2 measurements and shows little variation over latitude. The medium Kp case in figure 3.4 shows similar results. The high Kp case in figure 3.5 does not illustrate a good statistical distribution because of the small number of occurrences of Kp values greater than 4. But what is most evident in these plots is how the curve is being "stretched" towards higher

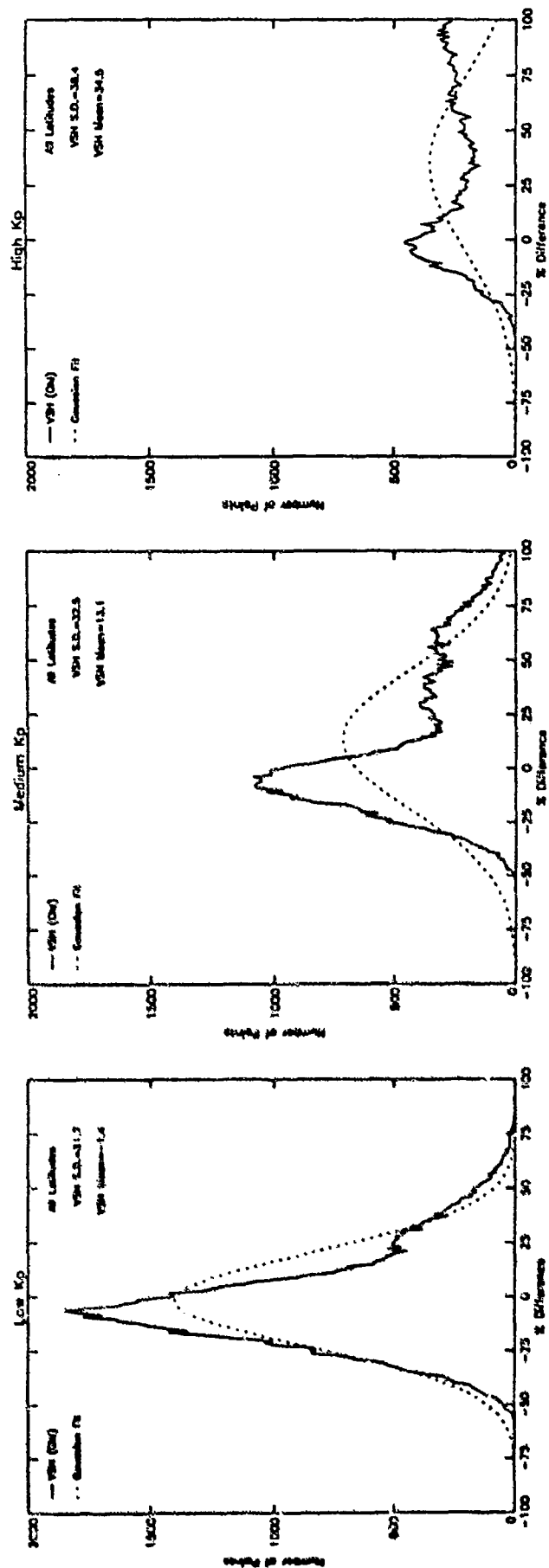


Figure 3.2 Plots of Kp dependence by old VSH.

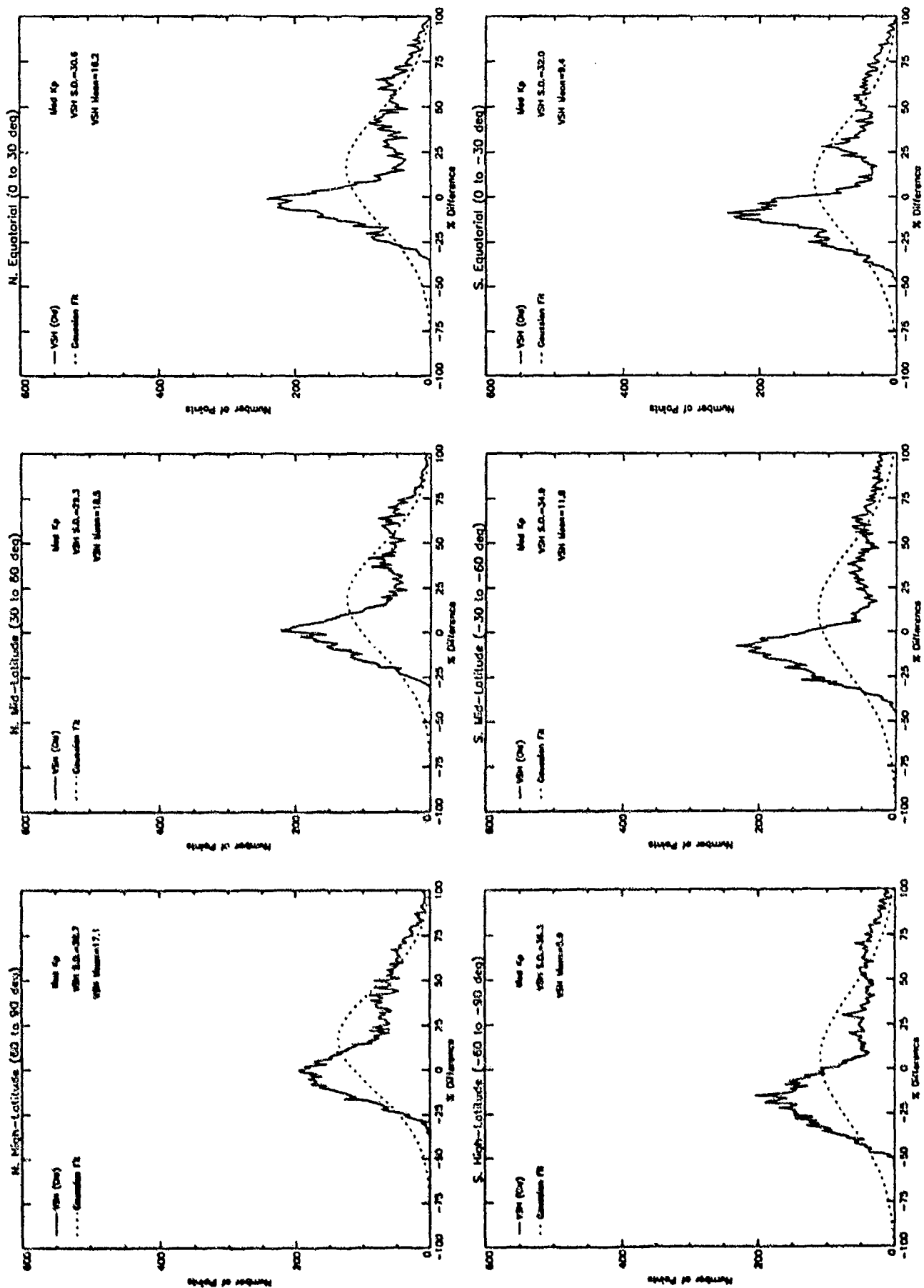


figure 3.4 Same as figure 3.3 except Medium Kp case.



values. Obviously the cause of this bifurcation is not latitude or Kp dependent since it occurs through all latitudes and Kp values.

The root of the problem was discovered when the data was divided even further into F10.7 bins. Three F10.7 intervals were chosen;  $F10.7 < 160$ ,  $160 \leq F10.7 \leq 190$ , and  $F10.7 > 190$ . Figure 3.6 is most indicative of the results from this binning. Each page represents one of the latitude intervals with the top row showing low Kp values, the second row medium Kp values, and the bottom row high Kp values. The three columns on each page coincide with the three F10.7 bins mentioned above.

The other latitude and Kp cases for the F10.7 binning are located in the appendix, a representative case is included here for evaluation. The series of three F10.7 plots in figure 3.6 indicates the cause of the bifurcation in the latitude plot in figure 3.4 and is for the case of the North equatorial region during medium Kp values. The first F10.7 plot corresponds directly with the primary peak of the North equatorial latitude plot of figure 3.4. The second F10.7 plot is an intermediate one that shows the VSH densities beginning to drift towards higher values, while the third F10.7 plot directly coincides with the secondary peak in the latitude plot. Therefore, VSH specified densities well during low F10.7 values ( $< 160$ ), but began overcompensating as the F10.7 value increased until a local maximum occurred during high F10.7 values ( $> 190$ ).

This can be further explained by figure 3.7 which shows a plot of the F10.7 values versus the Kp values during the SETA-2 period. The horizontal axis represents the three F10.7 intervals used in this study and the vertical axis represents the Kp values with horizontal lines drawn to represent the three Kp bins. This type of plot illustrates the correlations

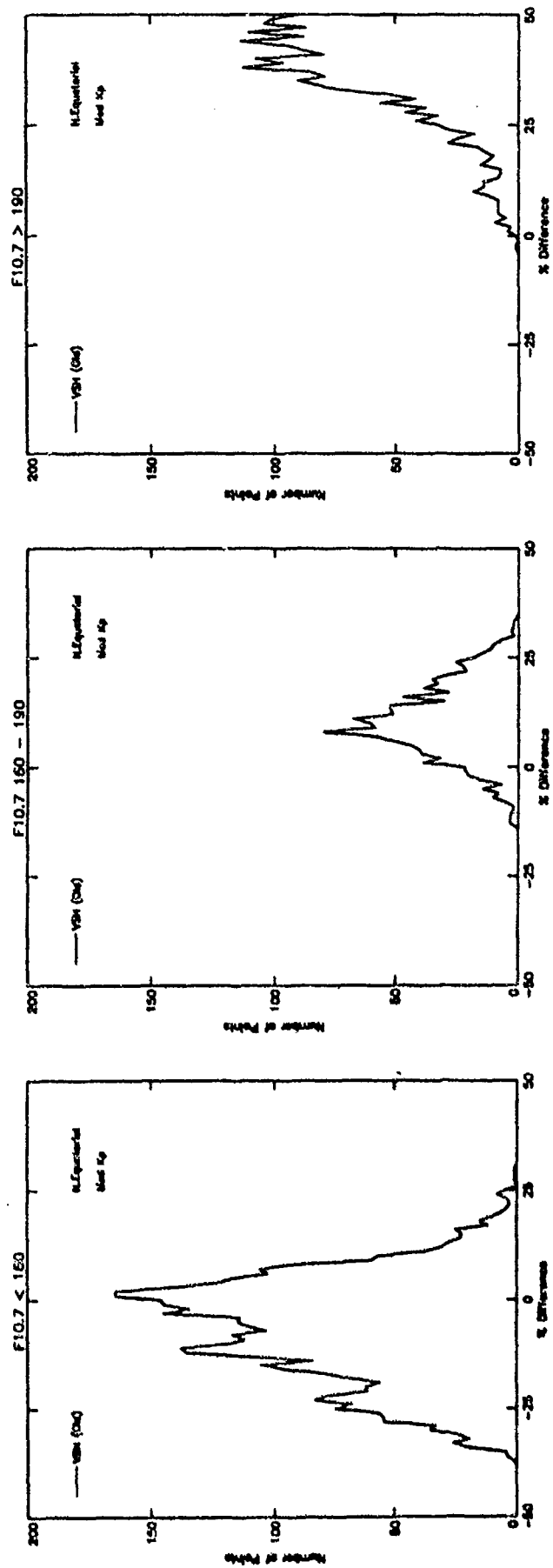


figure 3.6 Plots illustrating the F10.7 dependence of old VSH  
(for N. Equatorial, Medium Kp case).

between the two indices and helps explain that the data was being bifurcated partly because of the choice of Kp and F10.7 bins.

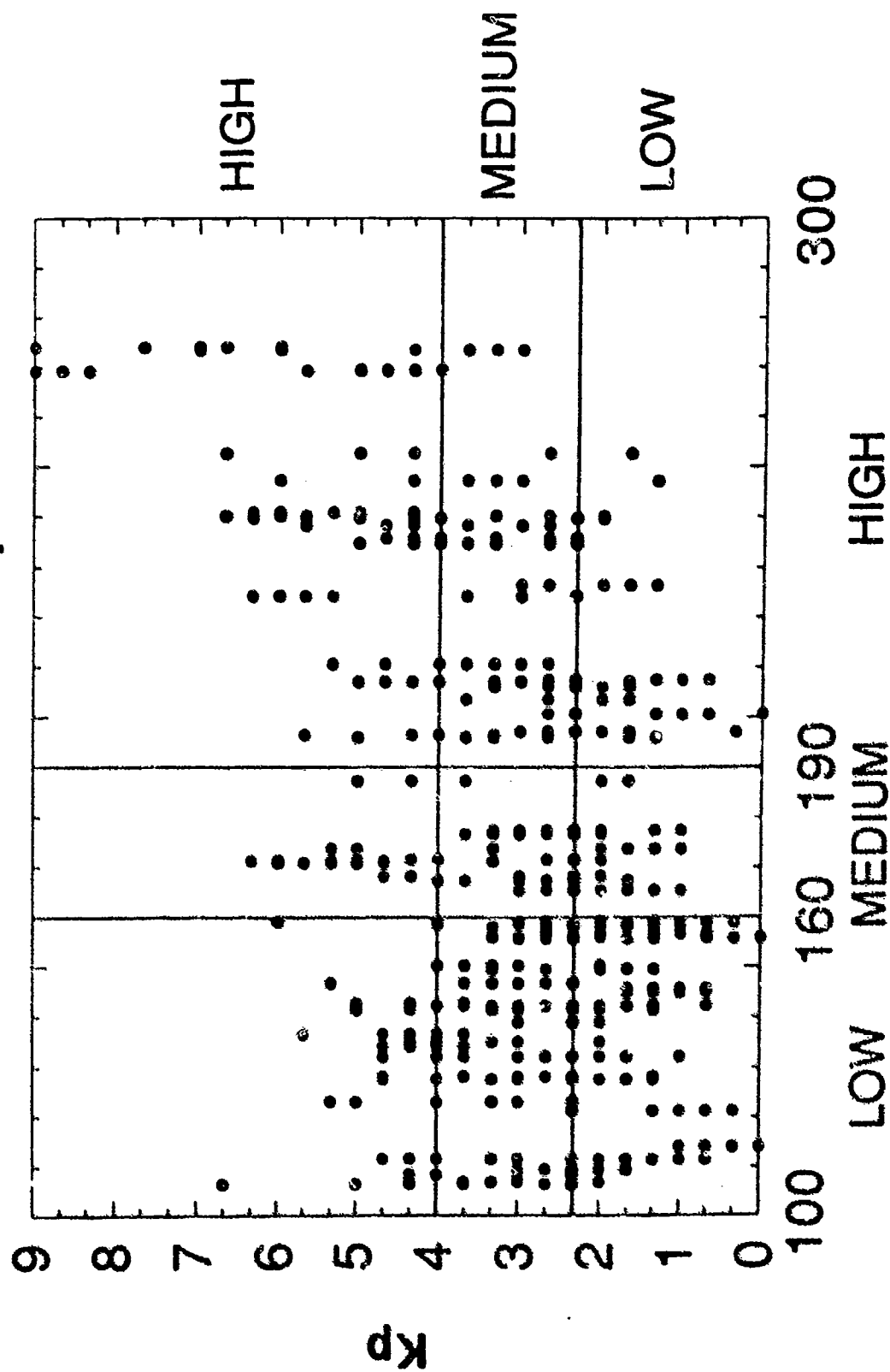
The figure illustrates that during low Kp values most of the occurrences of F10.7 values were concentrated in a small interval (100-160) on the low side. In the high Kp case, occurrences of F10.7 were mostly on the high side, but were spread out over a larger interval (190-280). The narrow interval in the low Kp case tended to concentrate the VSH densities into the primary peak whereas the larger F10.7 interval tended to "spread" the densities on the high side. The sum of these effects was to create the bifurcation.

The physical reason for this problem was also due to VSH using only F10.7 as the input for solar flux. But F10.7 is primarily an indicator of the short term variability of the sun which affects the upper thermosphere more so than the lower thermosphere (see section 1.2.1.1 for further discussion of this matter). Therefore the SETA-2 measurements occurred at low altitudes this F10.7 dependence showed up indicating a need for an additional parameterization. The F10.7a index was included in a height dependent solar flux parameterization (section 1.2.1.1) since it better indicates the state of the lower thermosphere. The current version of VSH (with this parameterization) shows marked improvement in density specification and shows no bifurcation of data. Results of the current version are included in section 3.2.2.

### 3.2.1.1 Height variation

Another problem noted during this study has to do with the NCAR-TIGCM and its ability in specifying the mean density values. The TIGCM

# F10.7 vs. Kp



F10.7

Figure 3.7 Correlation between the Kp bins and the F10.7 bins used in this study.

is very good at computing variations of output fields about a global mean. However, as mentioned previously, in the case of neutral density output, the TIGCM global mean is different from that of the MSIS model, which is derived from climatologically averaged satellite data (Killeen, et al., 1991). The density mean of the TIGCM has to be adjusted to be more in line with MSIS.

It was initially thought that the density profile of the for the TIGCM and MSIS looked like figure 3.8a, where the scale heights (or slopes) were equal but offset by a factor. Based on this, one height level was chosen in making the correction factor between the two scale heights (a to b in figure 3.8a). But later it was found that the scale heights were different as in figure 3.8b. A correction was made in going from a to b and then also applied to a lower level, following the assumed scale height, the density was still off by the difference between c and d. Therefore, a single height level couldn't provide a proper correction factor. A second height was used to get an improved adjustment as in figure 3.8c and correction factors were determined by interpolating between the two heights.

This adjustment is important in mapping the proper height to a pressure level (which is the vertical coordinate system used in the TIGCM) for use by the VSH model. This also results in enhancing the performance of the mass density output from VSH.

### **3.2.2 Model to data comparisons using current version of VSH**

The results included in this section come from the August 1991 version of VSH. I used the same systematic approach with the current version as with the older version, showing an overall dependence of the

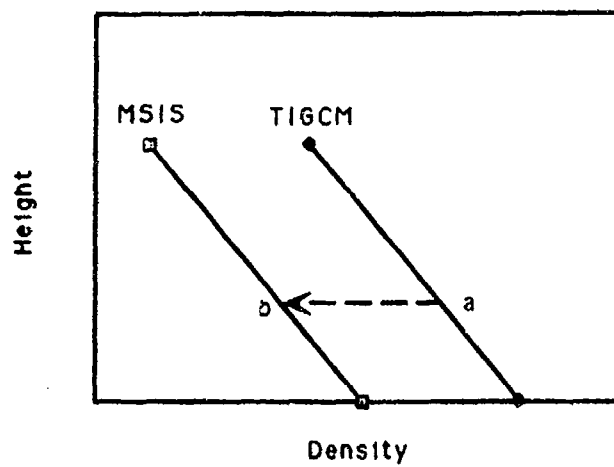


figure 3.8a Scale height comparison (expected)

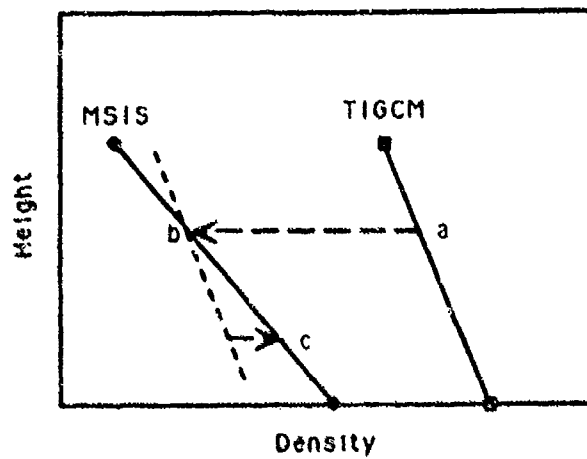


figure 3.8b Scale height comparison (expected)

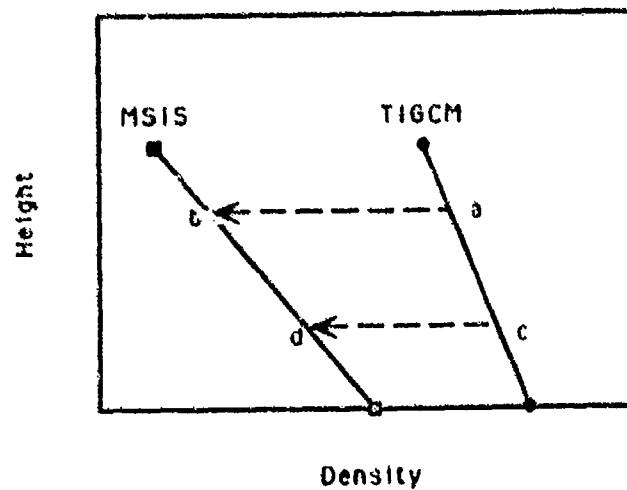


fig. 3.8c Scale Height Comparison (actual)

model to the SETA-2 data and then binning the data into Kp and latitude intervals. In addition to this I have also included MSIS curves to make inter-model comparisons and also identify and attempt to explain the physical processes that cause model variability. Since the standard deviation value is most indicative of how well a model specifies density, I will primarily use this value as a "yardstick" to compare VSH and MSIS results.

The last subsection includes model to model comparisons of standard deviation results based on binning by various parameters including Kp, latitude, altitude, and F10.7. These results indicate that VSH does as well as and in many cases significantly better than MSIS in the specification of density.

### 3.2.2.1 Overall dependence

The whole data set was compared with both VSH and MSIS models with no binning of data. The results of this are illustrated in figure 3.9. As can be seen the VSH curve is markedly improved over the older version of VSH (see figure 3.1 for comparison). The frequency distribution for VSH is more Gaussian-like with little dispersion about the mean and no areas where the density is strongly over- or under-estimated. In comparison, the MSIS curve has more dispersion about the mean, creating a larger standard deviation than that of VSH (14.8% compared to 12.2% for VSH). This standard deviation for MSIS corresponds well with previous studies (Marcos, 1989) and represents the limit of performance for empirical models. In comparing the mean values, MSIS is much closer to the SETA-2 measurements, whereas the VSH mean indicates underestimation by

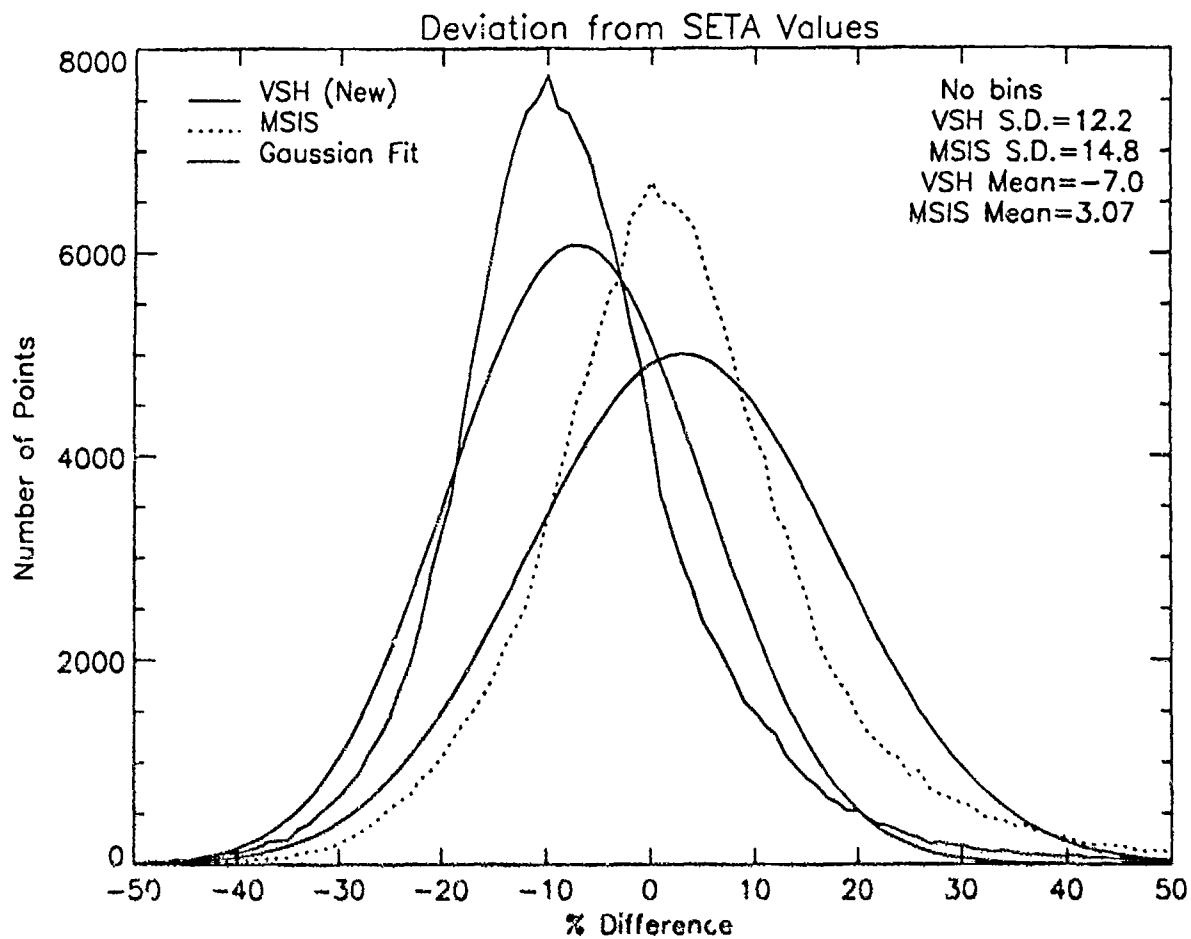


figure 3.9 Overall plot of new VSH deviations from SETA values.



7.0%. However, for the end user of the VSH model a simple correction factor can be included to shift the mean in the desired direction.

Little physical information can be derived from this plot, only to note that MSIS is slightly skewed to the right with a small "tail" where a number of density values are being overestimated by 30-40%. However, no reasoning for this can be given based on this plot. More information may be concluded by dividing the data under various conditions.

### 3.2.2.2 Kp dependence

Using the same procedure as section 3.2.1 the data is binned into three Kp intervals in order to determine the performance characteristics of the model based on magnetic activity. Figure 3.10 illustrates low, medium and high Kp conditions for VSH and MSIS.

The models represent density best during low Kp cases. The VSH curve has little dispersion and does not appear to be skewed in either direction. MSIS, on the other hand, has a larger standard deviation than VSH but a better handle on the mean value. As in figure 3.9 MSIS is positively skewed indicating some conditions where densities are being overestimated.

Under the medium Kp case it can be seen that both models begin to disperse more and the mean values are shifted. In the high Kp case (note change in vertical scale) the models have a more difficult time representing density. The standard deviations for each increase to values  $>16\%$ . Both models are also strongly skewed positively, more so in the MSIS curve, which accounts for the larger standard deviation.

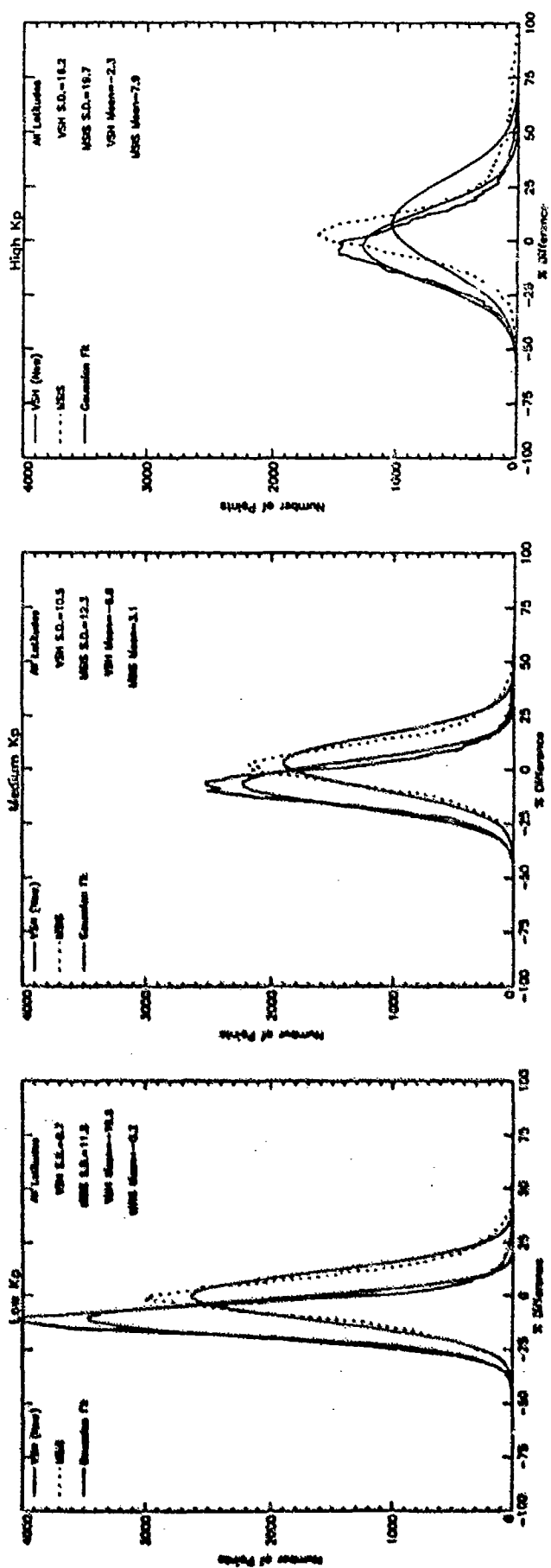


Figure 3.10 Plots of Kp dependence by new VSH and MSIS.

The MSIS model does poorer in the high Kp case than in low Kp case, due to the spatial resolution of the model. As described in section 2.2, MSIS retains ~5 harmonics which in turn limits the effective spatial resolution to 20 degrees. The VSH model also has poorer statistics during high Kp cases, but tends to do slightly better (a standard deviation of 16.2% compared to 19.7% for MSIS) possibly due to the better resolution of the NCAR-TIGCM, which has an effective spatial resolution of 10 degrees. The limited spatial resolution of the models makes it difficult to resolve the fine density structure that occurs during times of high Kp such as during geomagnetic storms. During these storms the density can vary greatly from the high density area in the "throat" of the ion convection pattern to the relatively low density surrounding areas.

The mean values for both models drift from negative to more positive values from low to high Kp values. This is most probably due to the models overcompensating as the Kp levels increase. This pattern of the mean drifting is also obvious in the latitude plots shown in the next subsection.

### 3.2.2.3 Latitude dependence

The accuracy of thermospheric models is limited by their ability to resolve atmospheric occurrences that happen on very small scales. As described in the first chapter the ion convection pattern in the high latitude regions causes intricate circulation patterns, upwelling and enhanced localized heating that results in small scale variability in the density structure. During geomagnetic storms when the Kp index increases, the variability in density becomes even more complicated since the circulation pattern is even further enhanced and distorted.

The next step in evaluating model performance was to put the data in six 30 degree latitude bins while keeping the Kp bins. The plots in figures 3.11-3.13 are set up as described in section 3.2.1.

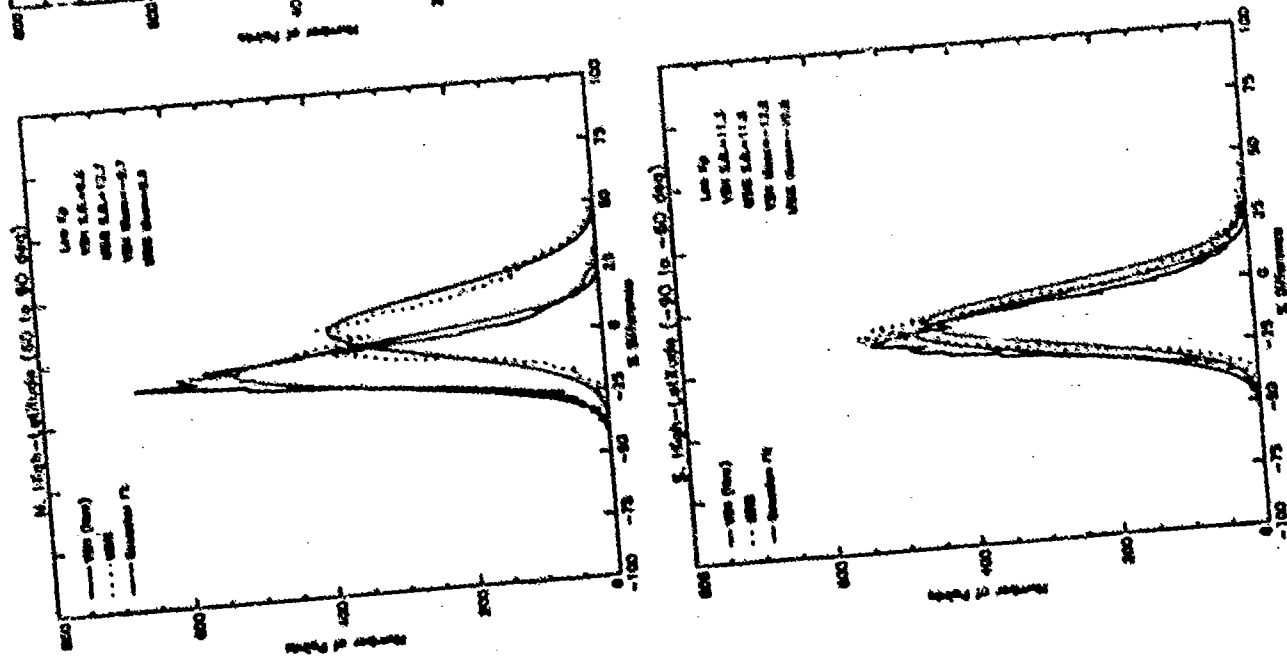
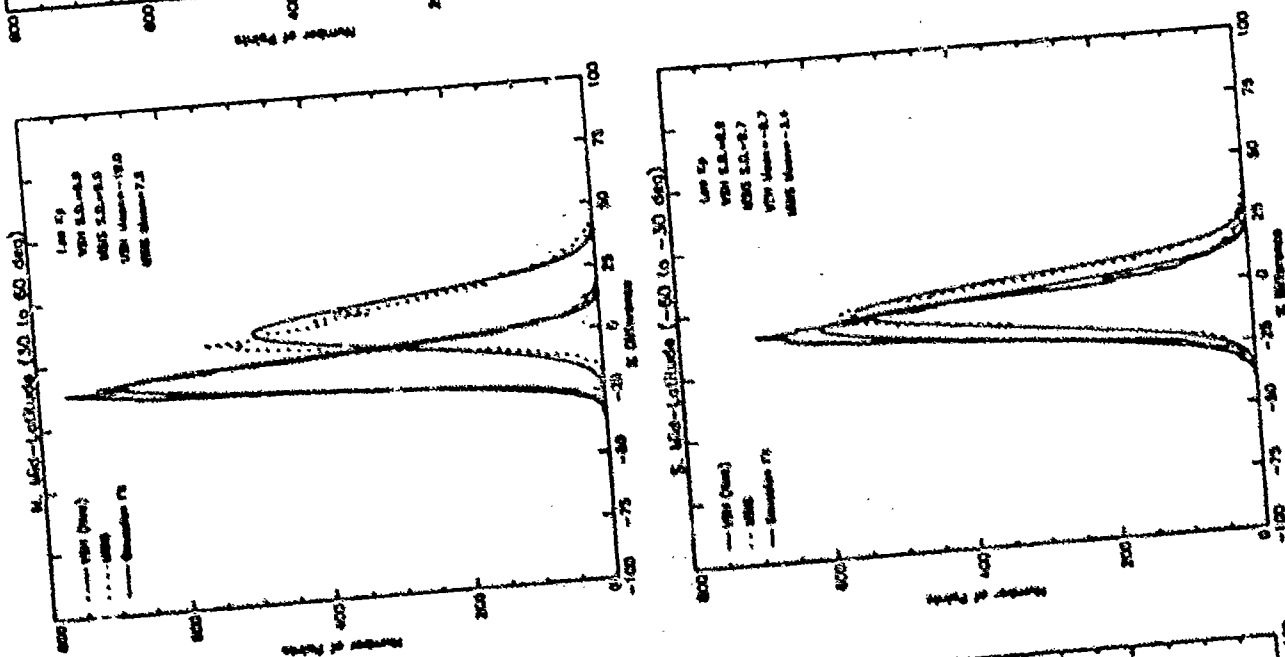
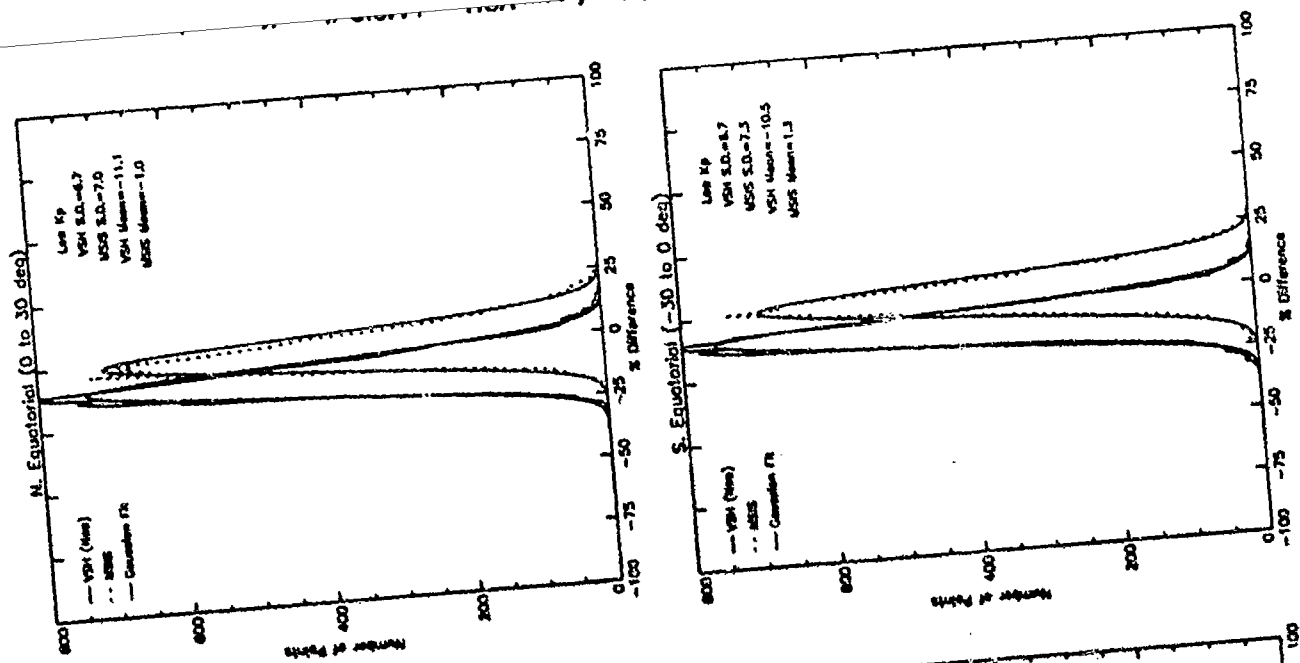
The VSH and MSIS curves exhibit little dispersion in the low latitude regions during low Kp values, with VSH having slightly better standard deviations, but both curves become more dispersed in the middle and high latitudes. Also noticed, is that both models show positive skewness with increasing latitude, possibly due to the models beginning to compensate for the more structured auroral regions but tend towards overestimation.

In the medium Kp case both models' standard deviations increase by ~1-2% over the low Kp case due to the enhanced density structure that begins as magnetic activity increases.

As seen in the low Kp case the models do well in the low latitudes but their standard deviations increase by a factor of two in the high latitude case. The models begin to show this increase in the mid-latitudes due to auroral effects becoming evident even at mid-latitudes. As mentioned before, the resolving capability of the models limit their ability to specify the fine density structure that shows up during these effects.

It is also evident that there is some pattern to the way the mean value drifts. This is evident in each of the cases to some degree. It is most obvious in the medium Kp case of the MSIS curve. The mean value increases from negative to more positive values as the latitude goes from the southern to the northern hemisphere. This occurs to a lesser extent in the VSH curves also.

There really is not enough information to definitively explain the occurrence of mean drift. It could be due to a seasonal dependence of the model, with underestimation occurring in the southern hemisphere winter



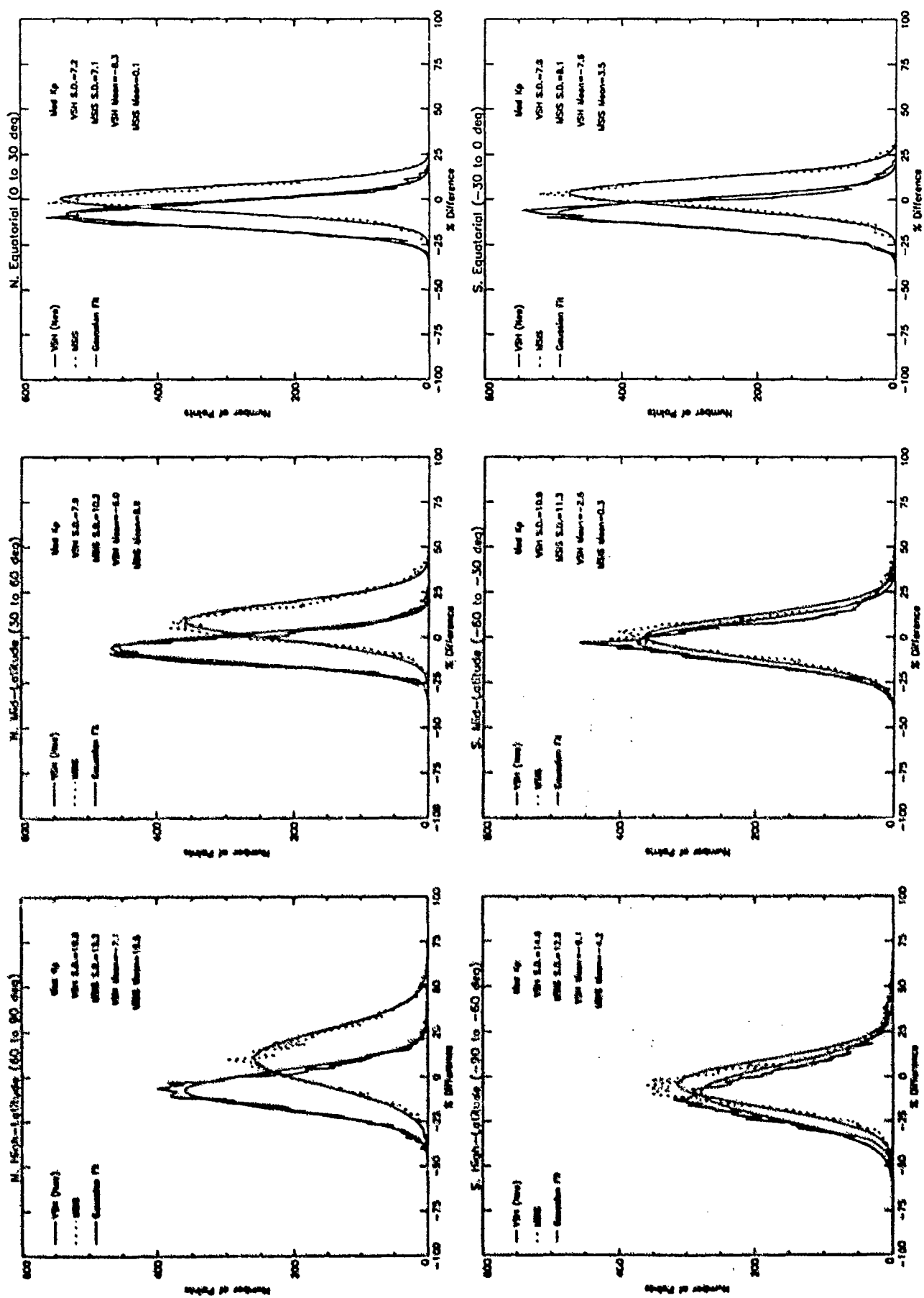


figure 3.12 Same as figure 3.11 except Medium Kp case.

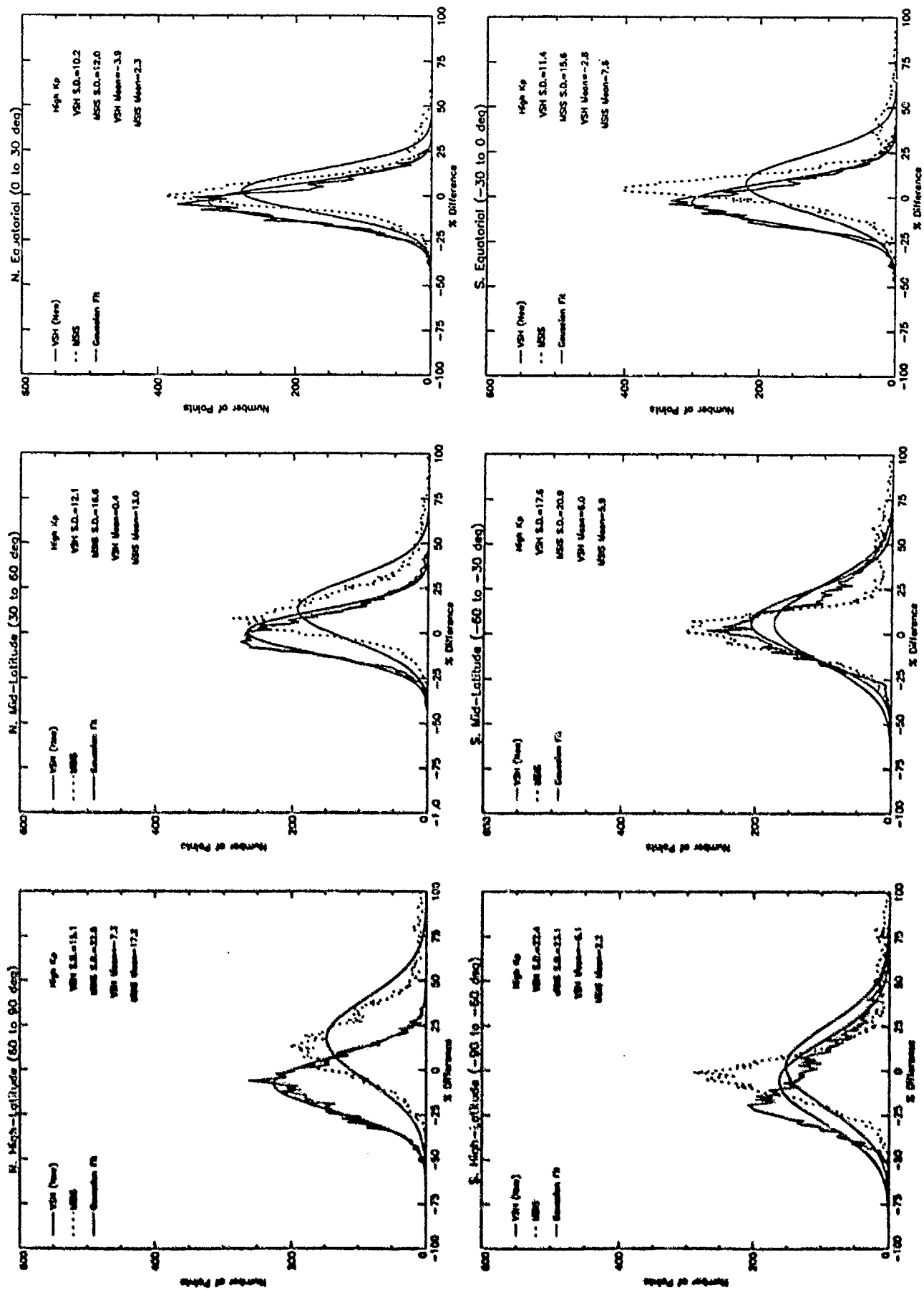


Figure 3.13 Same as figure 3.11 except High Kp case.

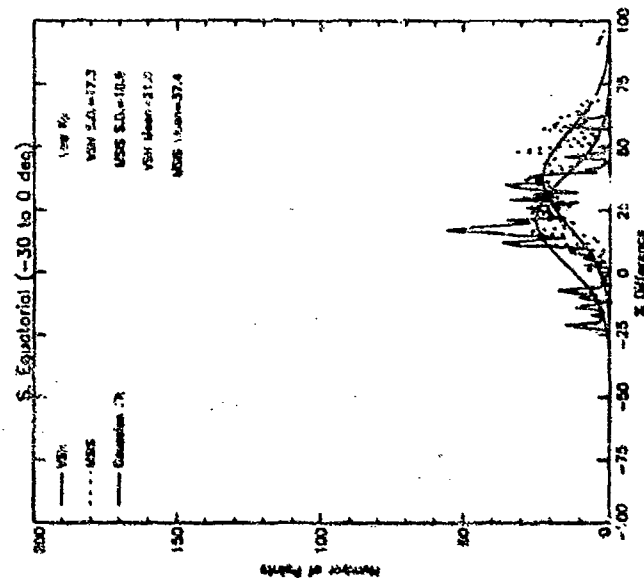
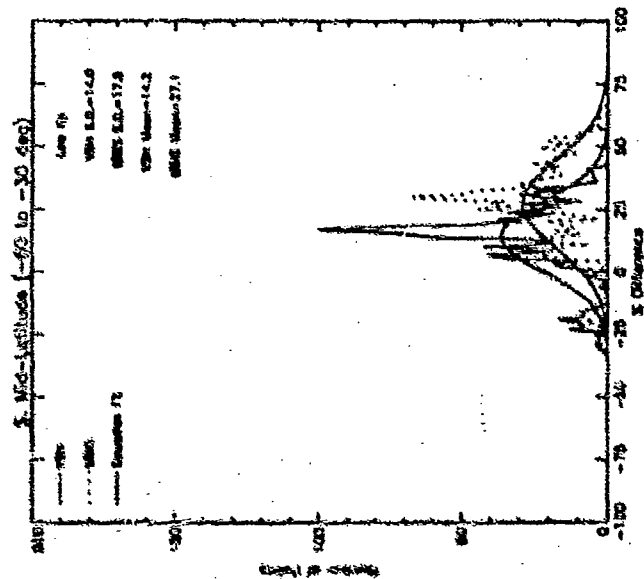
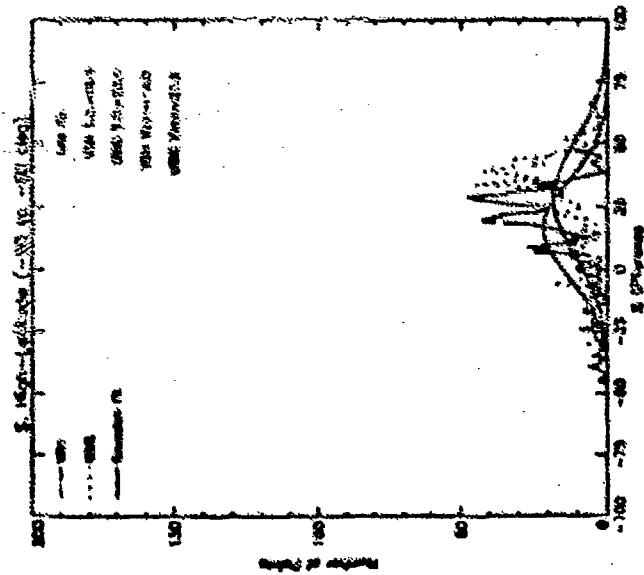
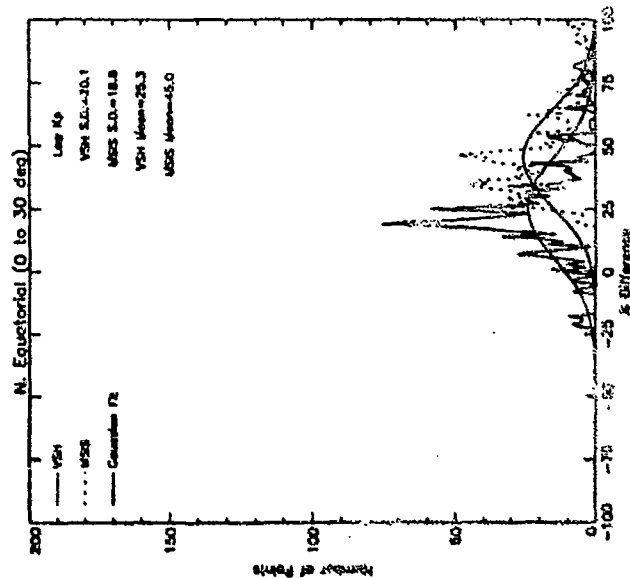
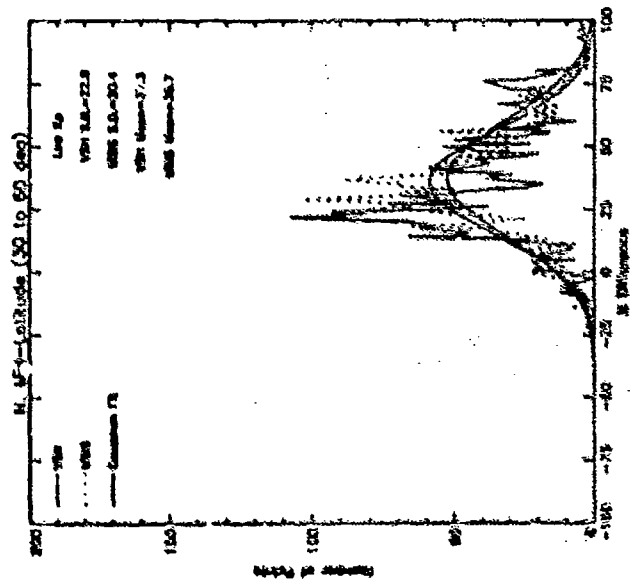
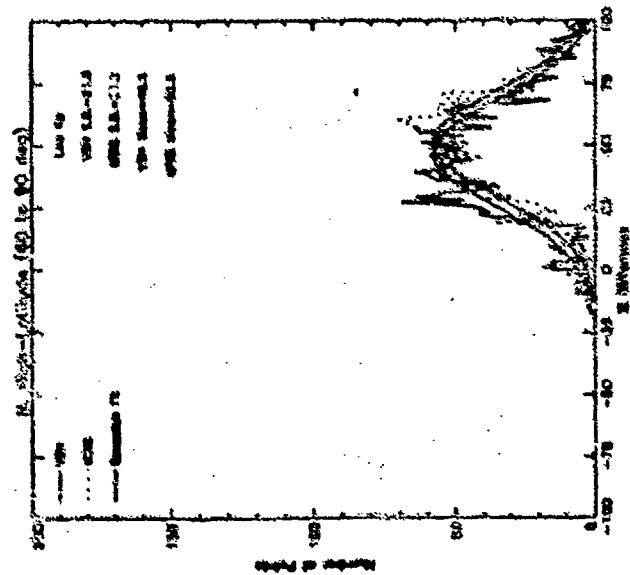
and overestimation occurring in the northern hemisphere summer. Or, it could simply be due to hemispheric differences. Pole to pole differences in the turbopause height would allow for differences in total density measurements. Also, since the circulation pattern is slightly different in the southern high latitudes than in the northern high latitudes, resulting density measurements could also be different.

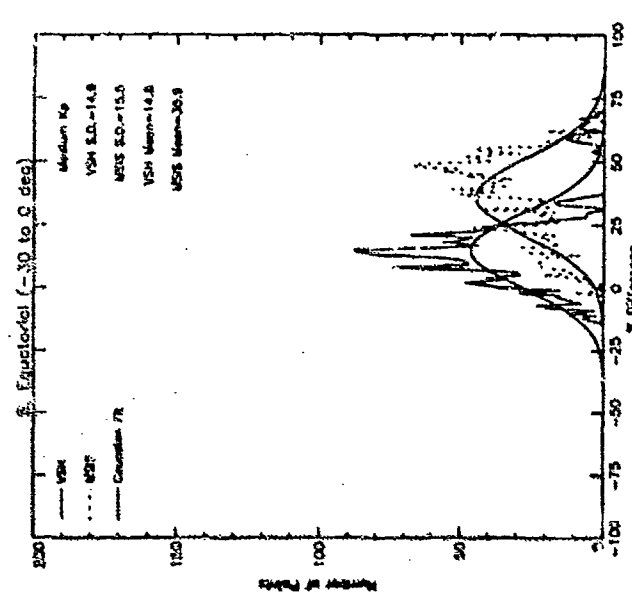
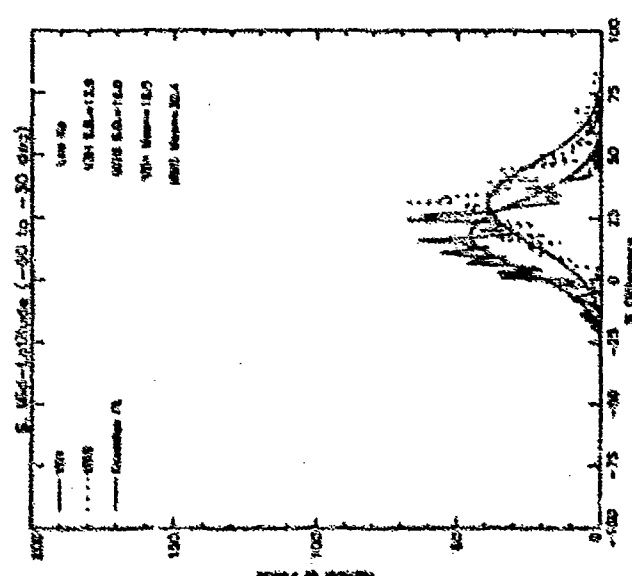
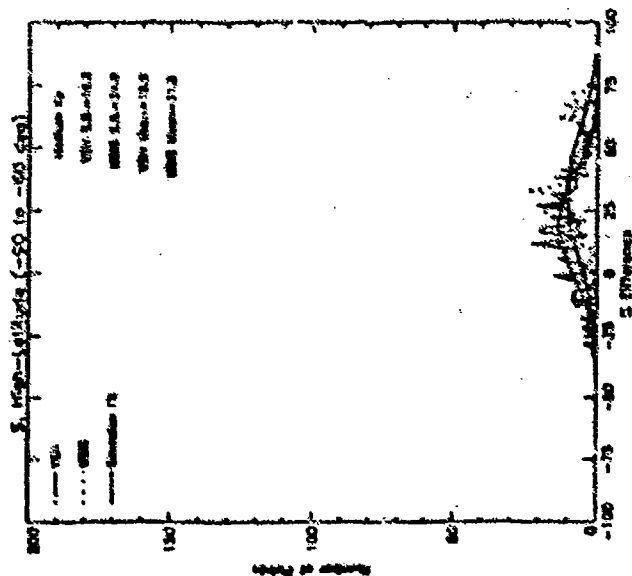
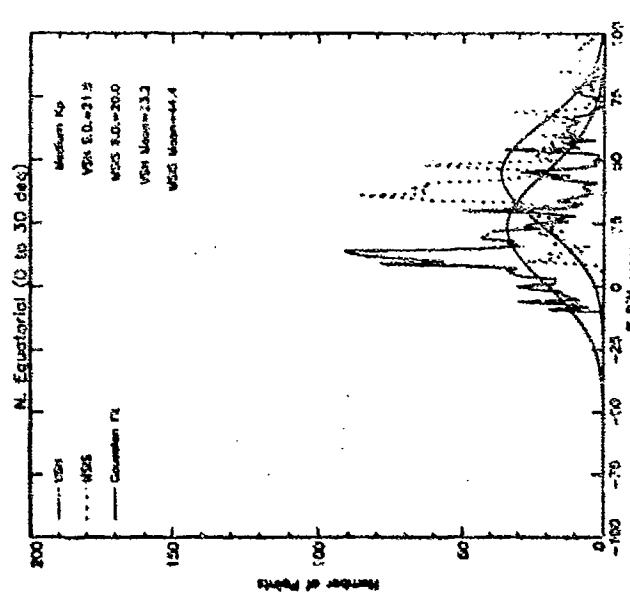
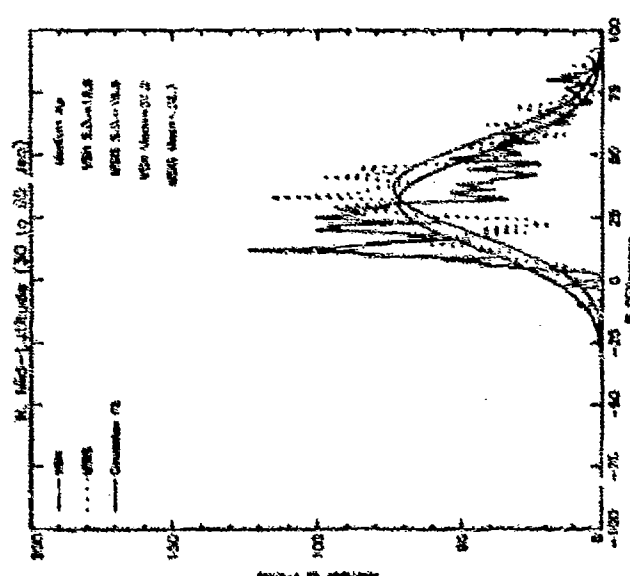
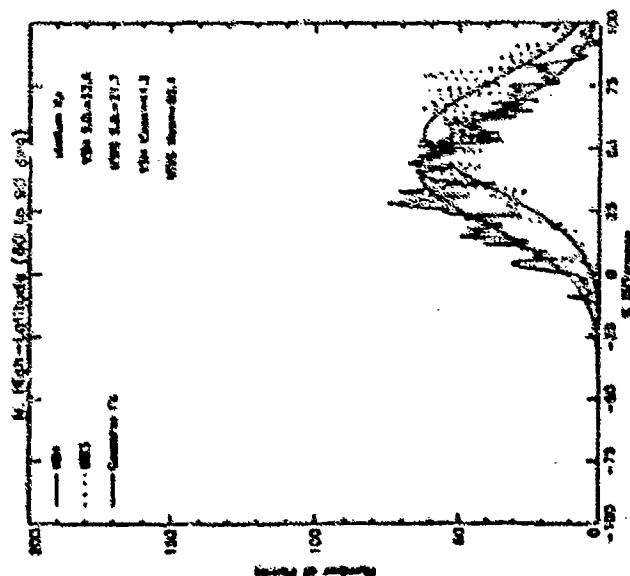
Another feature evident in these plots is that VSH tends to do better in the northern hemisphere than in the southern hemisphere, whereas MSIS shows no hemispheric bias. This bias of VSH is possibly due to the northern hemisphere bias exhibited in the NCAR-TIGCM.

In the high Kp case, degradation in the model curves is quite evident, especially in the high latitude region. VSH is strongly skewed in the positive direction in the southern hemisphere, but MSIS is even more so in all cases with a secondary maximum beginning to show up (see south mid-latitude and equatorial region plots). This secondary maximum is most possibly a high solar flux dependence by MSIS. The plot in figure 3.14 illustrates the same F10.7 bins as in section 3.2.1 and shows that the area of overestimation in the MSIS curve does not show up in the low F10.7 plot but does appear to occur in the high F10.7 plot.

The next series of plots show the results from comparing the models to measurements from the NACS instrument on the DE-2 satellite during the same time period as the SETA-2 data set. This satellite flew at an altitude range of 300 to over 1000 km with composition measurements were taken only up to ~500 km. It was hoped that using high altitude DE-2 data in conjunction with the low altitude data from the SETA-2 instrument would help show altitude dependences of the models. However, upon comparing the NACS plots, figures 3.15-3.17, to the SETA-2 plots it became







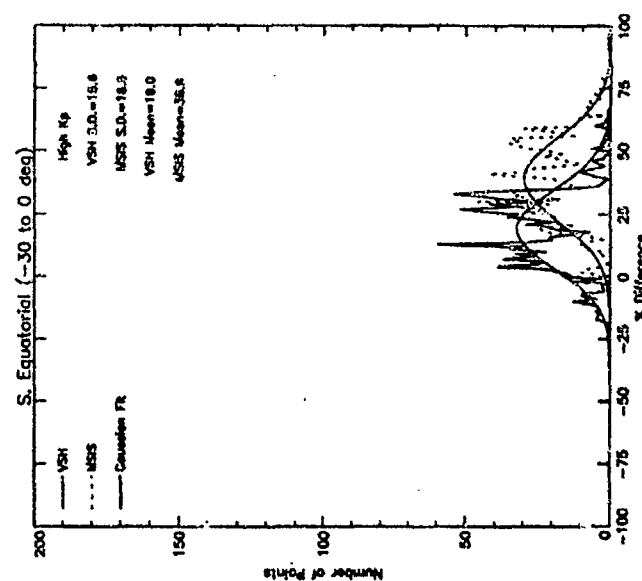
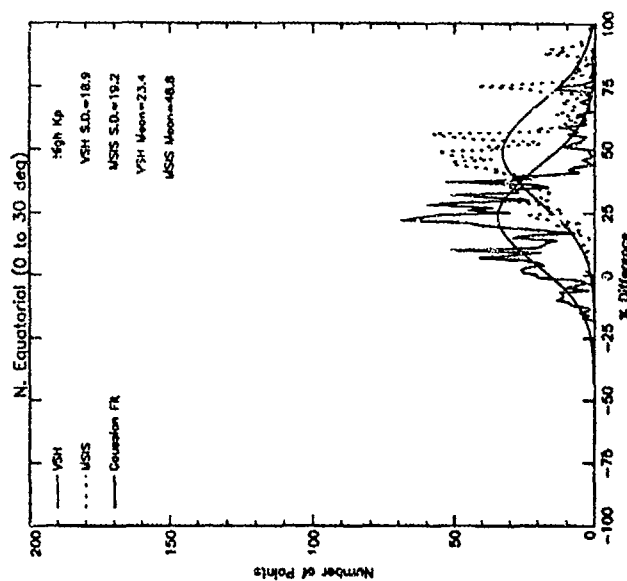
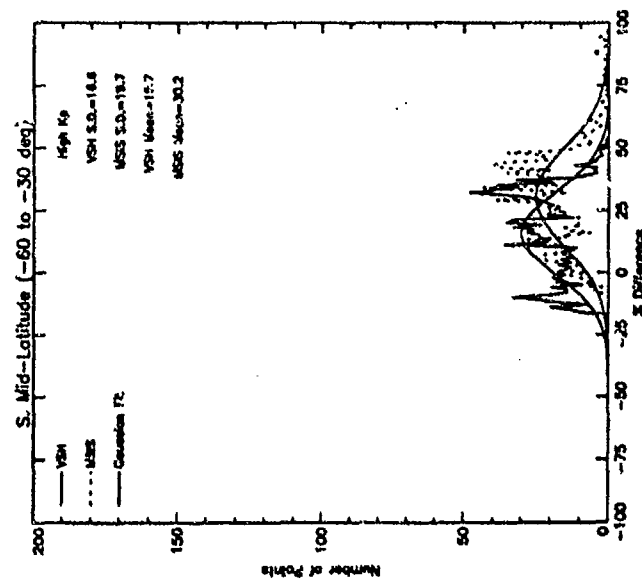
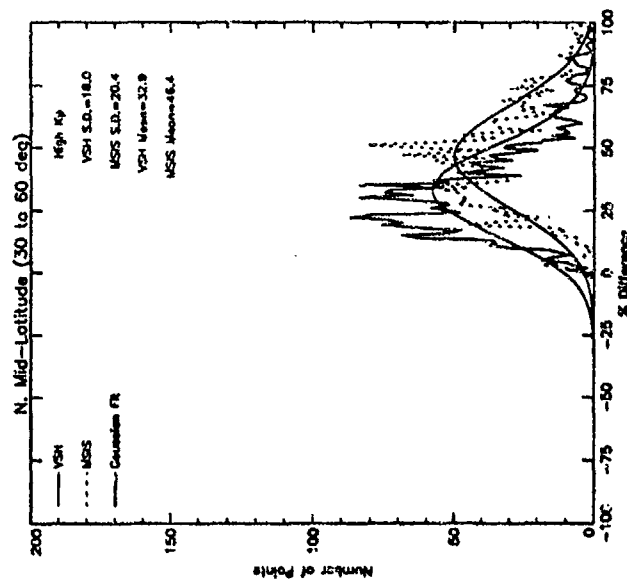
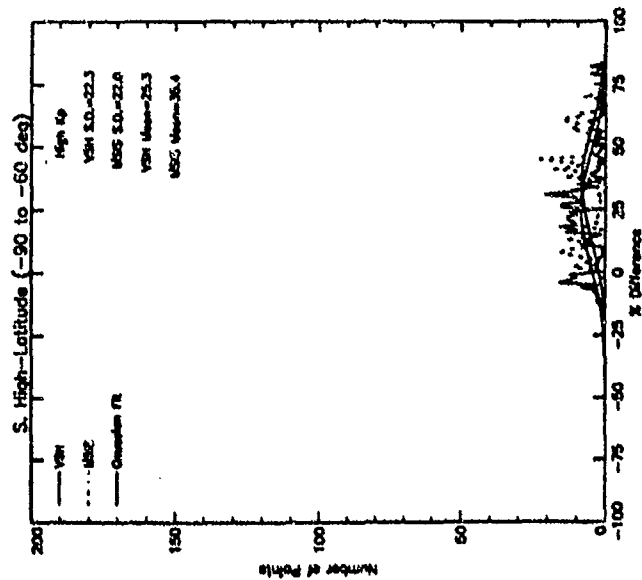
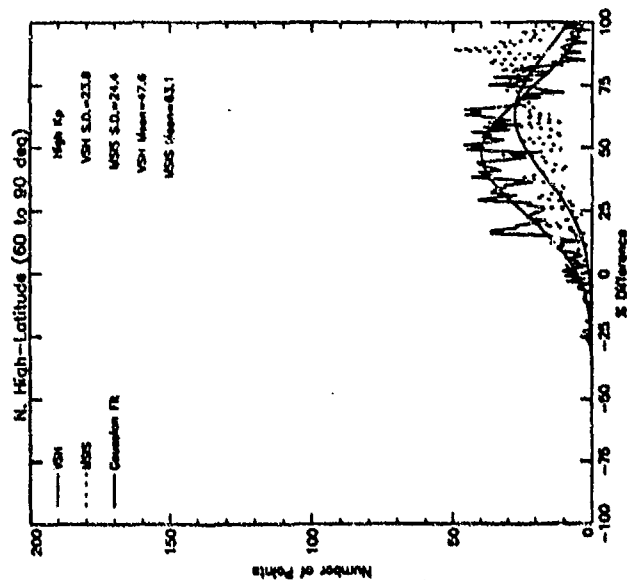


Figure 3.17 Same as 3.15 except High Kp case.

quite obvious that the absolute instrument accuracy approaches model accuracy due to the calibration problem explained in section 2.5. Also, the amount of NACS data during this time period was about a factor of ten less than there was SETA-2 data, and the resulting statistical distributions (note vertical scale) are not quite as good. This small amount of data and the instrument accuracy make model to data comparisons quite difficult to make.

Absolute comparisons cannot be made with the SETA-2 plots for the above reasons but comparisons can be made and trends can be detected among the two models within the data set. As in the previous section figures 3.15-3.17 represent latitude and Kp dependences. There was more northern hemisphere data than southern hemisphere data available during this time since perigee was in the northern high latitudes, so southern latitude comparisons are difficult to make and are not included in the following short discussion.

In the low Kp case MSIS shows better standard deviations than VSH over all latitudes, but the mean values are fairly close to each other. The VSH mean values show a definite trend towards higher errors with increasing latitude for all three Kp cases. This could show a height dependence of the model or it could be variability in the instrument accuracies over altitude ranges. Little else can be said about the medium and high Kp cases except that the standard deviations of both models are close through all latitudes.

### 3.2.2.4 Standard deviation comparisons

To make easily observable comparisons between VSH and MSIS I binned the SETA-2 data into four parameters separately. The standard deviations of VSH and MSIS were calculated for each case and compared using a bar graph.

The parameters include Kp, latitude, F10.7, and altitude. The first three parameters were binned using the same intervals as before and the altitude parameter was binned into three intervals over the SETA-2 altitude range (160-200, 200-230, 230-260).

Figure 3.18 shows the results from binning the data by low, middle and high Kp values. In each case VSH has a lower standard deviation than MSIS by ~2 percentage points.

The next figure, 3.19, indicates the variability of the standard deviation over latitude. VSH does very well in the northern hemisphere as compared to MSIS, but the VSH-MSIS difference is much closer in the southern hemisphere with higher standard deviations for each corresponding latitude interval in the southern hemisphere. This is most probably due to the hemispheric bias of the NCAR-TIGCM as mentioned earlier in this chapter.

The F10.7 standard deviations of the models in the next figure are quite close in the medium and high F10.7 cases but VSH does ~3 percentage points better than MSIS in the low F10.7 case.

The final graph shows the altitude dependence of the models. Again, VSH does significantly better (~4%) in the lower altitude regions, but the two models are essentially equal in the high altitude interval.

### Deviation from SETA 2 Data

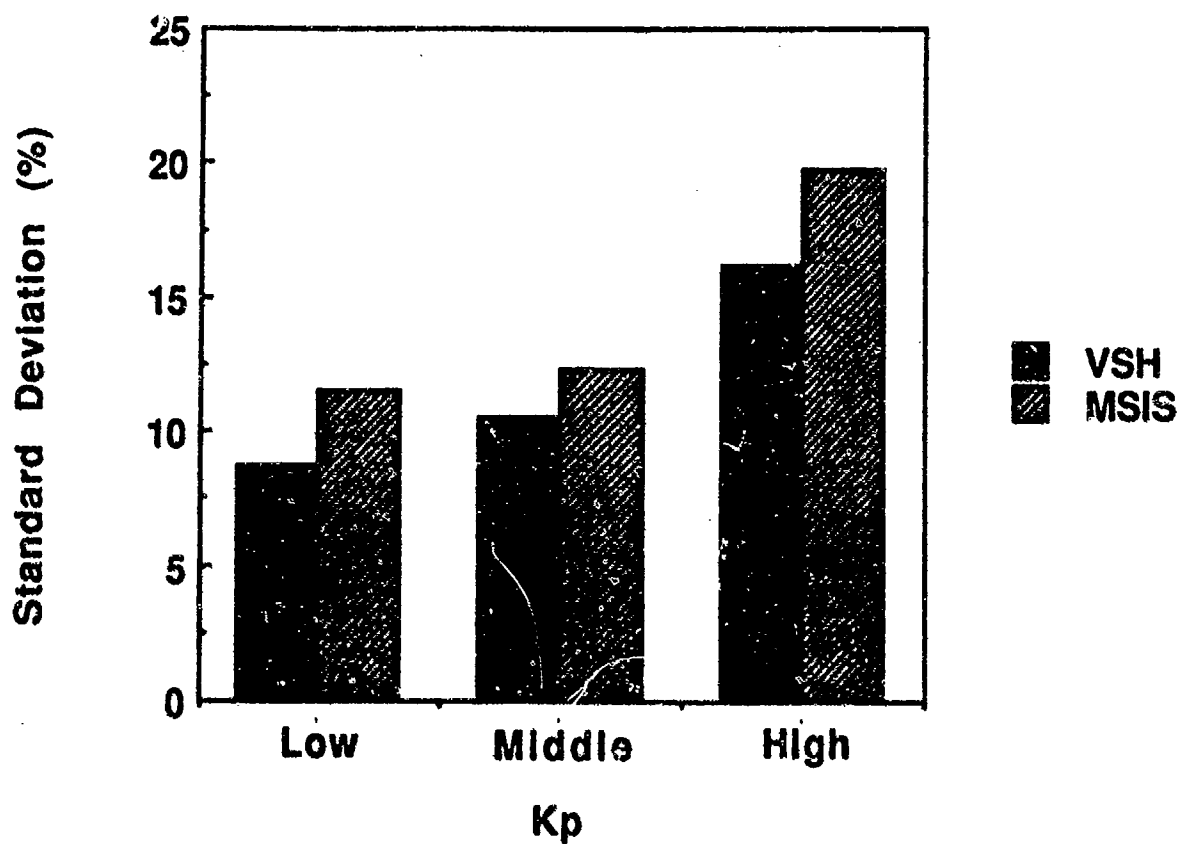


Figure 3.18 Standard deviation comparisons of the Kp dependence of VSH and MSIS.

### Deviation from SETA 2 Data

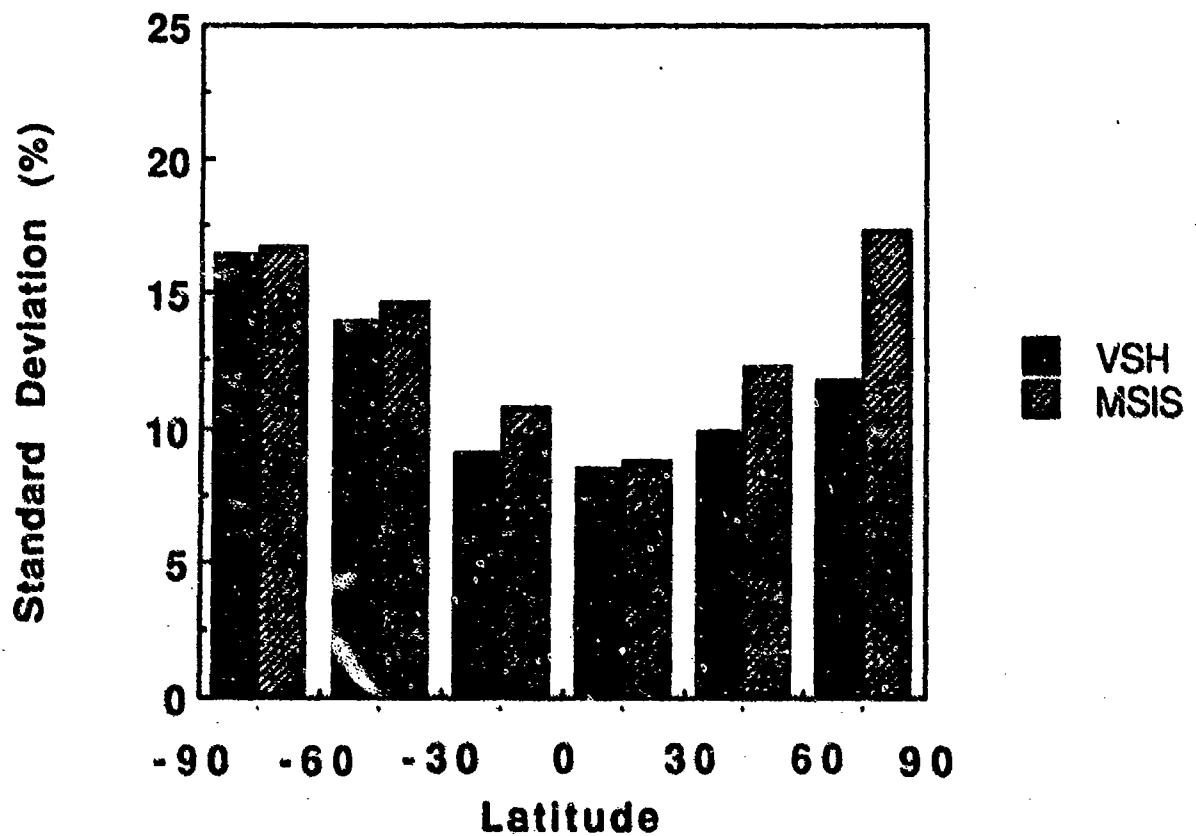


figure 3.19 Same as figure 3.18 except for latitude dependence.

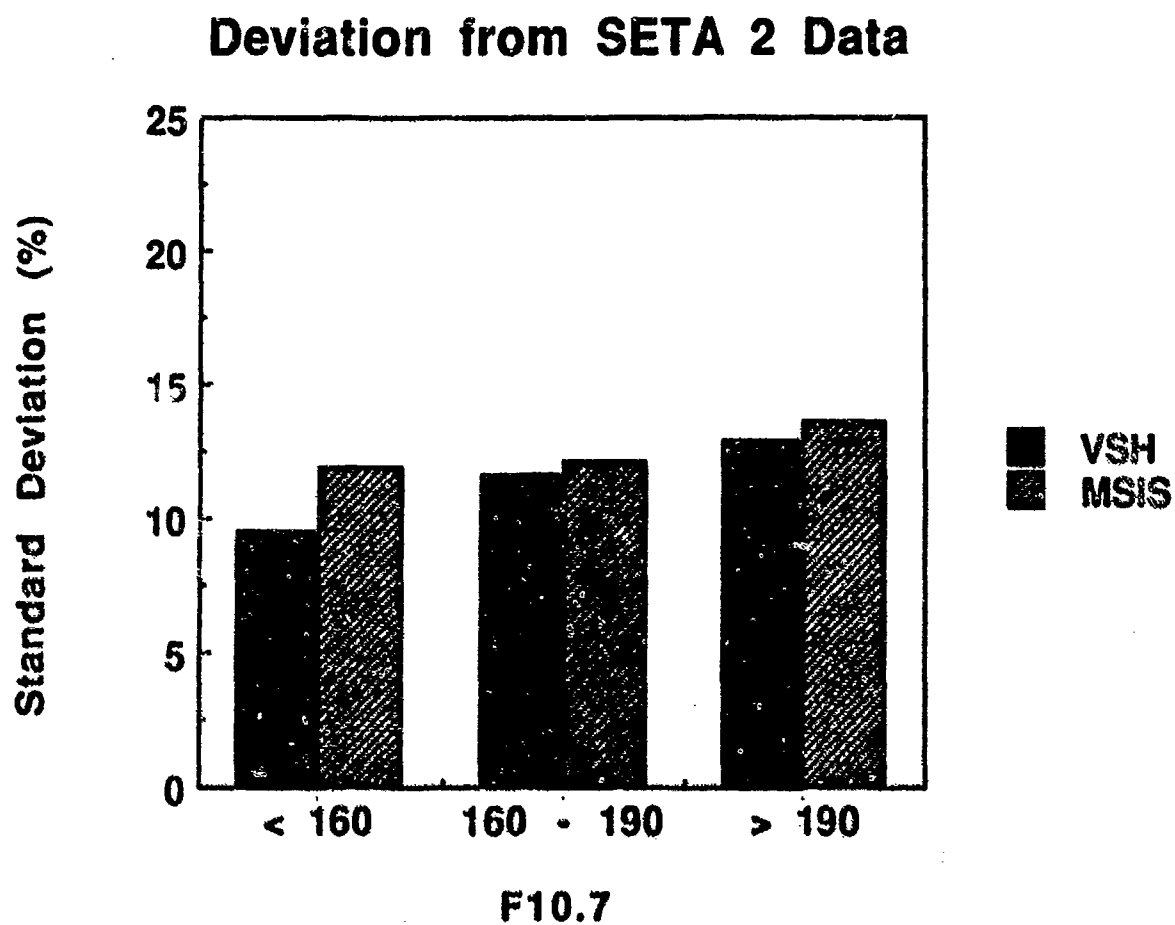


figure 3.20 Same as figure 3.18 except for F10.7 dependence.



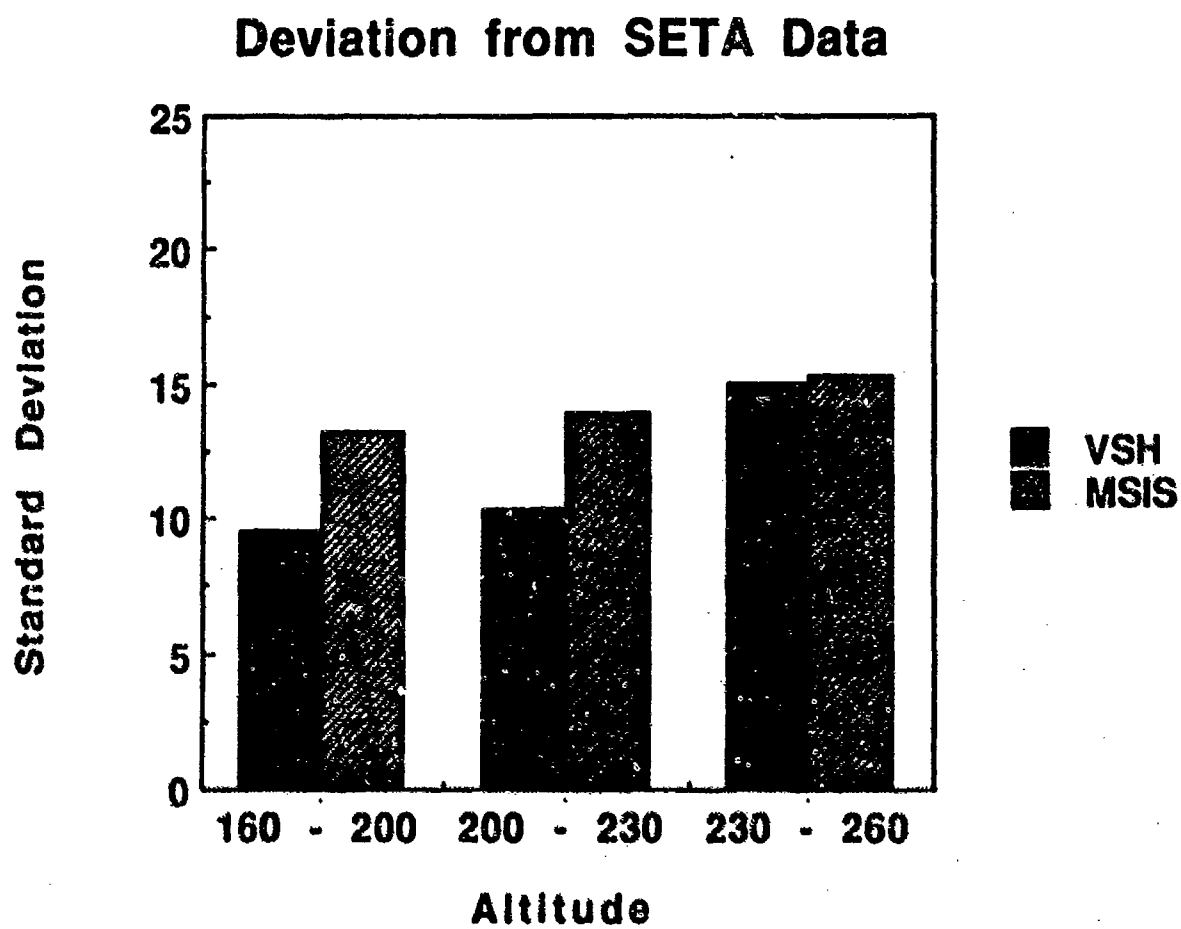


figure 3.21 Same as figure 3.18 except for altitude dependence.

These results were determined using the same statistical technique described in chapter 1 and are consistent with the results from the validation study in the previous subsection.

### 3.3 Conclusions

This is one of the first extensive validation studies of the VSH model. Neutral density output from the model was compared to accelerometer measurements of the lower thermosphere. The SETA-2 data set was quite extensive, providing 70 days worth of data during solstice conditions in 1982 which was a time close to solar maximum. The SETA-2 measurements were shown to be quite helpful in validating the VSH model in a region of the atmosphere that is quite data sparse.

More work can be done using this data set, such as evaluating any local time dependences of the model. After this, the validation study can continue by using measurements from other instruments, such as the SETA-1 instrument that took lower thermospheric wind and total density measurements during equinox conditions of 1979.

During this study we discovered a significant shortcoming in the VSH model based on a solar flux dependence. The problem was corrected using a height dependent F10.7 parameterization that includes the use of the F10.7 average value. The subsequent results show marked improvements in density specification.

The data was binned using a variety of parameters to test the characteristics of the VSH and MSIS models. The results show that VSH exhibit very low standard deviations ( $< 10\%$ ) during low magnetic activity and virtually all latitude regions. Only minor increases of  $\sim 5\%$  for each

latitude region are shown as the magnetic activity increases to higher Kp values.

In the overall comparison, with no data bins, we found that VSH exhibited a standard deviation of 12.2% or ~3% lower than the MSIS empirical model. Also, during the model comparisons based solely on Kp, latitude, F10.7 and altitude, VSH standard deviations values were noticeably less in all cases than MSIS values. In particular, the northern high latitude and low altitude regions are ~3-4% lower.

## CHAPTER 4

### EFFECTS OF ORBITAL IN-TRACK WINDS ON SATELLITE DRAG

#### 4.1 Introduction

Neutral winds are important in the determination of the forces experienced by satellites. Such winds in the polar cap region of the earth's thermosphere can reach speeds greater than 1000 m/s and can change the drag or lift forces felt by a satellite by a large amount due to the uncertainty in the wind velocity. Such changes can subsequently affect the orbit of the satellite. Also, instruments, such as SETA, measuring density are dependent on wind information for being able to accurately specify the density (Killeen et al., 1988). Obviously, it is important to be able to accurately measure winds and know the effects that such winds have on space structures.

In this chapter I have included the results from my research that attempted to quantify the effects of meridional winds on a polar-orbiting satellite. My goal was to conduct this study over a large number of different orbits in order to provide a good statistical distribution of this effect. I also wanted to calculate the integrated drag through a whole orbit and determine the percentage of the drag over different regions about the globe.

However, due to time constraints, only the drag effect at each orbital point was determined. Rather than using measured winds, I used VSH model neutral meridional winds to illustrate the research capabilities of the model. Initial results indicate that a 700 m/s wind parallel to the satellite velocity vector changes the satellite drag by 23% during a time of high magnetic activity.

## 4.2 Procedure

To begin with I chose a typical DE-2 orbit late in the satellite's operational cycle in order to get a more circular orbit. A closely circular orbit would allow primarily latitude dependent wind variations and cut out most of the altitude dependence. The altitude interval through the orbit was 300 - 500 km with the perigee over the high latitude regions. The orbit was also constrained to certain local time meridians since we wanted the satellite to pass parallel to the transpolar flow, or the middle of the circulation pattern. The center of the circulation pattern lies roughly parallel to the 0-12 local time meridian and varies widely during enhanced magnetic activity.

In order to provide for a worse-case scenario, a time was chosen during 1982 when the F10.7 and Ap indices were high indicating strong magnetic activity and an enhanced ion convection pattern. July 14 was selected with the following geophysical conditions:

F10.7.....269.2

F10.7a....172.7

Ap.....153

The next step included using a FORTRAN routine that created the spatial and temporal points along the orbit given the initial conditions of apogee, perigee and local time. Along with the indicated geophysical conditions these orbital points were used by the VSH computer model to provide the total mass density and the neutral meridional winds required for satellite drag calculations. The method used for this calculation is described in section 1.3.

The resulting output was used in an IDL routine that determined the aerodynamic drag based on the in-track (meridional) winds and the density along the orbit. The output from this routine included satellite drag due to winds and the satellite drag without winds being taken into account. Using these two values the change in drag effect due to winds was calculated for each orbital point.

### **4.3 Results and discussion**

The data illustrated in this section results from an orbit with a 02-14 local time meridian with the geophysical conditions specified in the previous section. After observing the meridional winds along orbits with different meridians it was determined that this local time slice exhibited the strongest winds (742 m/s at a latitude of  $-85^{\circ}$ ) over the southern polar cap region.

The percent difference between the aerodynamic drag due to winds and the drag experienced without the effect of winds was calculated and plotted against the latitude along the orbit. The results are shown in figure 4.1. The plot shows that the largest absolute value of the percent difference causes a change in the aerodynamic drag by 23% due to a wind speed of 742

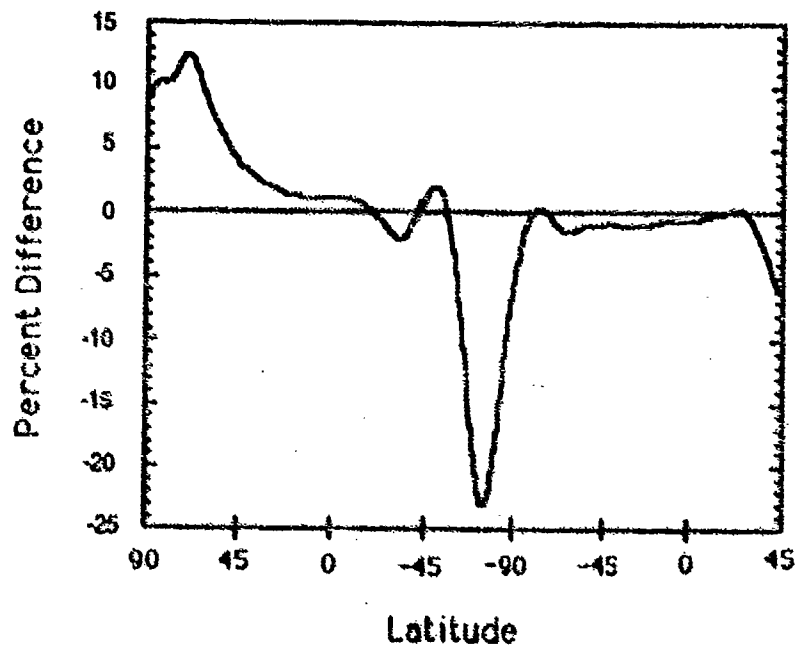


Figure 4.1 Percent difference between drag due to winds and drag with no winds plotted latitudinally

m/s over the southern pole. Since the percent difference is a negative value (the meridional wind vector is parallel to the satellite velocity vector) this actually means that the drag decreases or lift increases by 23%. However, due to the symmetry of the conditions, if the wind was directed against the satellite velocity vector, the drag would increase by 23%.

The plot coincides directly with the direction of the meridional winds but not with the magnitude, so a positive percent difference coincides with a northerly directed wind and the opposite goes for the negative values. It is then interesting to note that the plot also identifies the circulation pattern exhibited over the polar cap region. This is shown by the sudden change in the sign of the values as the plot goes from positive to negative and back on either side of the large peak in the southern hemisphere. A large peak is also noticed in the northern high latitudes which coincides with the circulation pattern in this region.

Although the results of this truncated study are inconclusive, they still indicate that winds can play a major part in determining satellite drag, especially during strong geomagnetic activity. This study also showed that the VSH model is quite useful in conducting research that requires input of thermospheric parameters. Rather than attempting to search a large satellite database for a particular orbit with the required orbital characteristics and conditions when a certain instrument is turned on, I was able to acquire the information much quicker and easier with the VSH model.



## CHAPTER 5

### DISCUSSION

A validation study of the total mass density output from the Vector Spherical Harmonic (VSH) computer model has been conducted with the subsequent results included in this thesis. Results from a small amount of research conducted on the effects of VSH neutral in-track winds on satellite drag have also been provided. Additional background on the thermospheric region and aerodynamic drag was included at the beginning of the thesis. I also provided information on the tools used in this study, which include the VSH and MSIS models, data from the SETA-2 and NACS instruments, and finally the statistical method used to compare the results in an objective manner.

An extensive validation program now exists that can be used to compare the VSH model to any data set. The program consists of a FORTRAN program that is capable of binning the data by various parameters and comparing these measurements to the corresponding results from the VSH and MSIS models. The output from this is then ran through another FORTRAN program that calculates the mean value and standard deviation of the specified data field and fits a normal (Gaussian)

distribution to the data. An IDL program allows the user to specify the particular bins and then plots the results in an appropriate format.

The plots illustrating the magnetic activity and latitude dependence of the models show that VSH provides the best results (with standard deviations less than 10%) during times of low Kp values and in lower latitude regions. There is only a factor of 1/2 increase during high Kp values and in higher latitudes. The VSH model does tend to show a hemispheric bias with better results in the northern latitudes.

Finally, in an overall comparison (through the whole data set with no bins) of VSH and MSIS, the standard deviation for VSH is ~3 percentage points lower than that of MSIS. A value of 12.2% for VSH is much lower than the standard that has been exhibited by empirical models over the past decade. This shows that a model based on truncated output of a TGCM is capable of improving our ability to specify thermospheric density.

However, it must be mentioned that these results are based solely on the SETA-2 measurements. Although an accelerometer provides some of our most accurate measurements of total density in the lower thermosphere, the information provided by the SETA-2 measurements is limited by the orbital characteristics of the satellite it flew on. There was a strong local time bias of the data, all the measurements are at an almost constant local time meridian (10-22 LT). Also, perigee occurred in the day sector and apogee in the night sector.

Another limitation to the results includes the statistical method used in comparing the two models. Although the technique for fitting a Gaussian distribution to the data is the same as in previous studies, due to the extent of the data and the extent of the skewness exhibited by the distributions, many of the model frequency distributions were distinctly

non-Gaussian and the use of these statistics did not fully represent the distribution. The resulting fits shifted the mean value and showed more dispersion about the mean than the main body of the distribution. Therefore, more robust statistics are recommended in future validation studies. Such a technique would strongly weight values closer to the mean than those that are further away and then use a full width at half maximum method. This method would apply only to the main body of the distribution rather than taking into account the "outliers", or values further away from the mean.

Nonetheless, with the SETA-2 conditions taken into account VSH still provides very good results. Under most conditions the VSH curves showed little dispersion about the mean and exhibited little or no latitude dependent drift in the mean value. There were only a few situations where the Gaussian fits were not representative. In those cases, the VSH distribution curve was nevertheless quite close to the MSIS curve.

The results from the research conducted on the effects of wind drag on satellites are not dramatic, but do tend to support previous studies indicating the importance of neutral winds on satellite drag. The initial results indicated a 23% change in the drag experienced by the satellite due to a 740 m/s wind. Since winds in the polar cap region have been measured at much higher speeds during strong magnetic activity it is obvious that the drag felt by a satellite flying through such an area will be even more changed due to the velocity squared term in the equation for aerodynamic drag.

The gist of this study has to do with our ability to specify the parameters that effect satellites in orbit about the earth. Both winds and density have a strong affect on such satellites and our ability to maintain

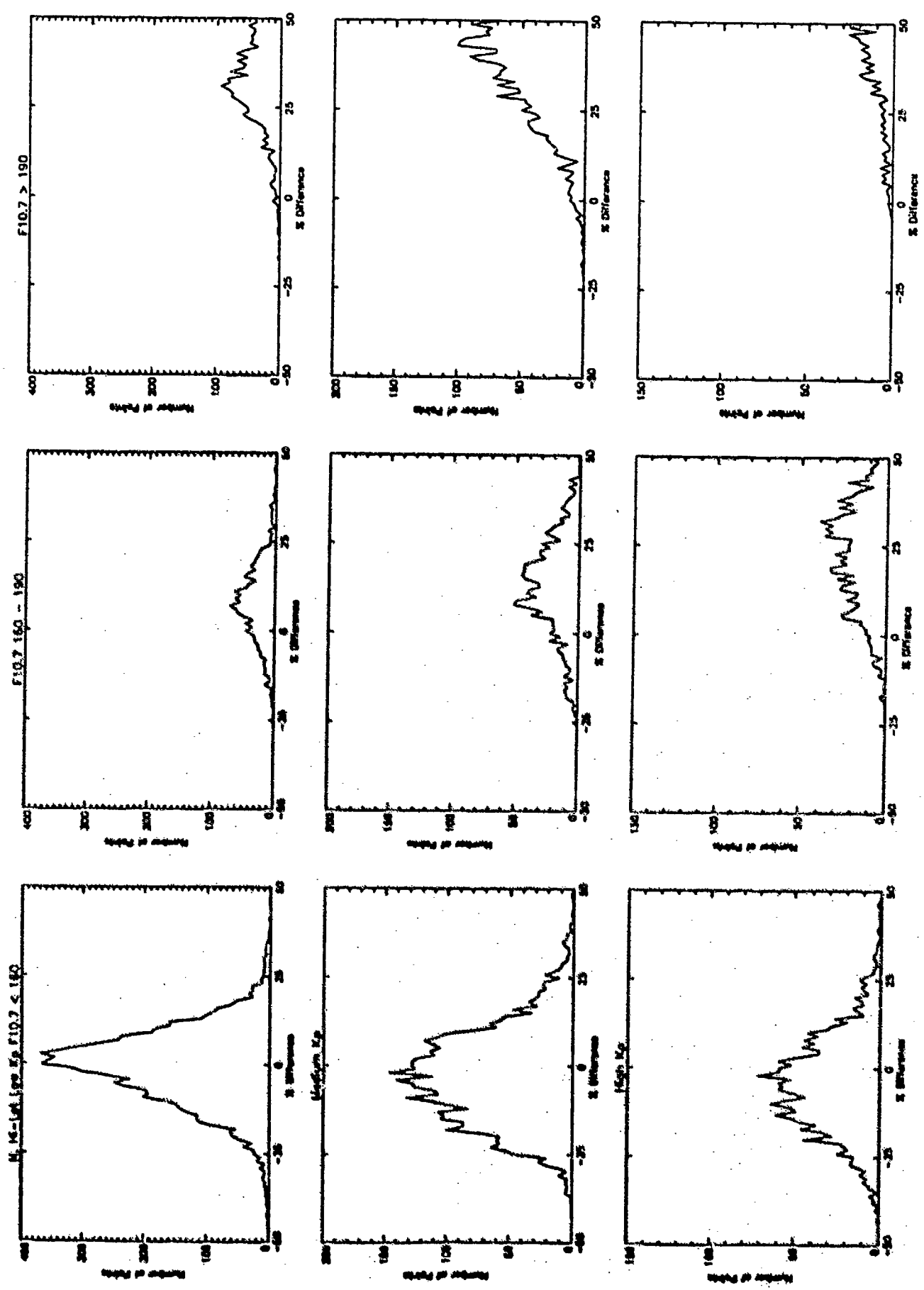
and use these spacecraft can be strongly impacted by the accuracies with which we are capable of specifying these parameters. Further research into such computer models as VSH will only increase our knowledge of the thermosphere and allow us to better keep track of the valuable resources that orbit through this region.

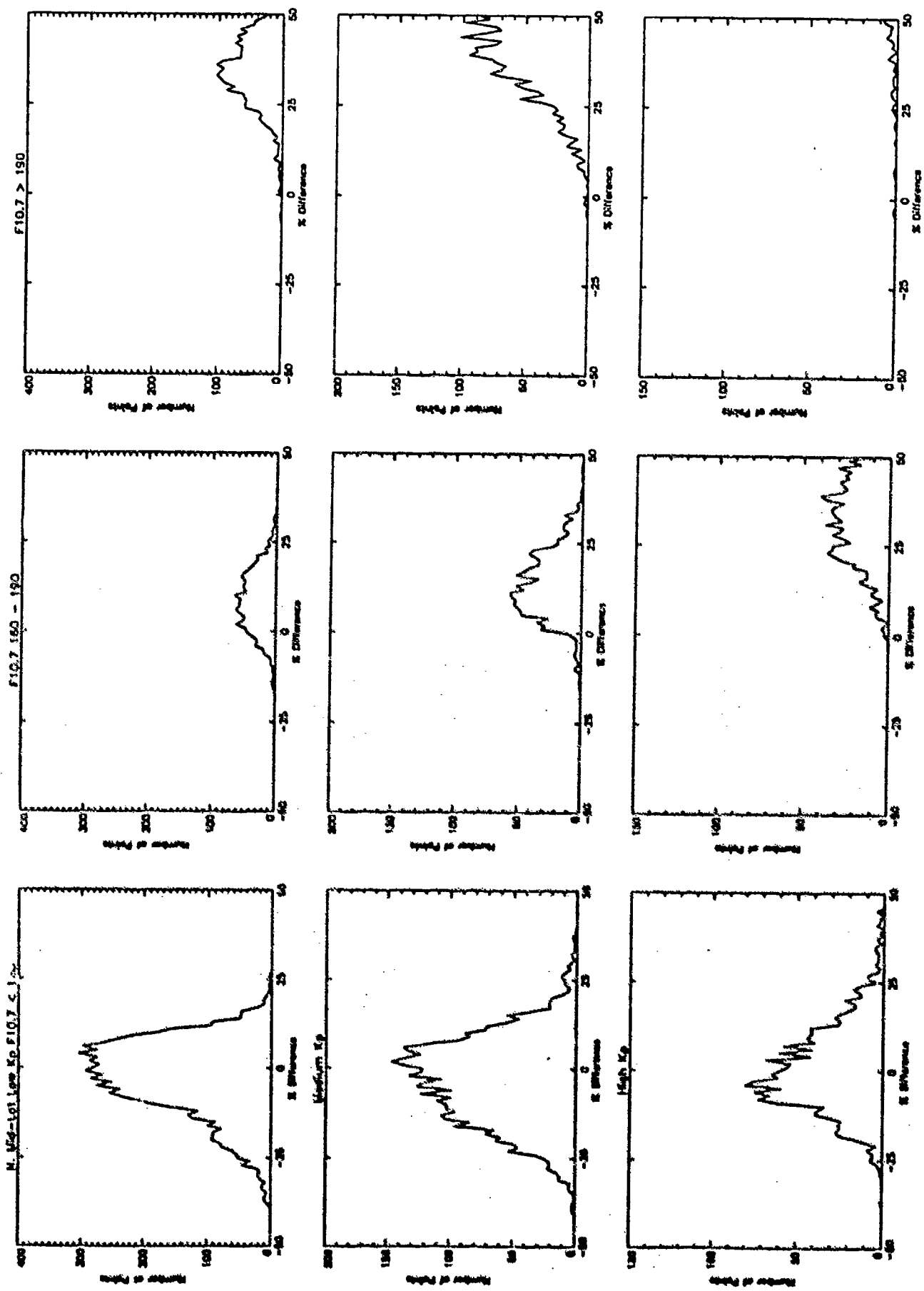
**APPENDIX**

## APPENDIX A

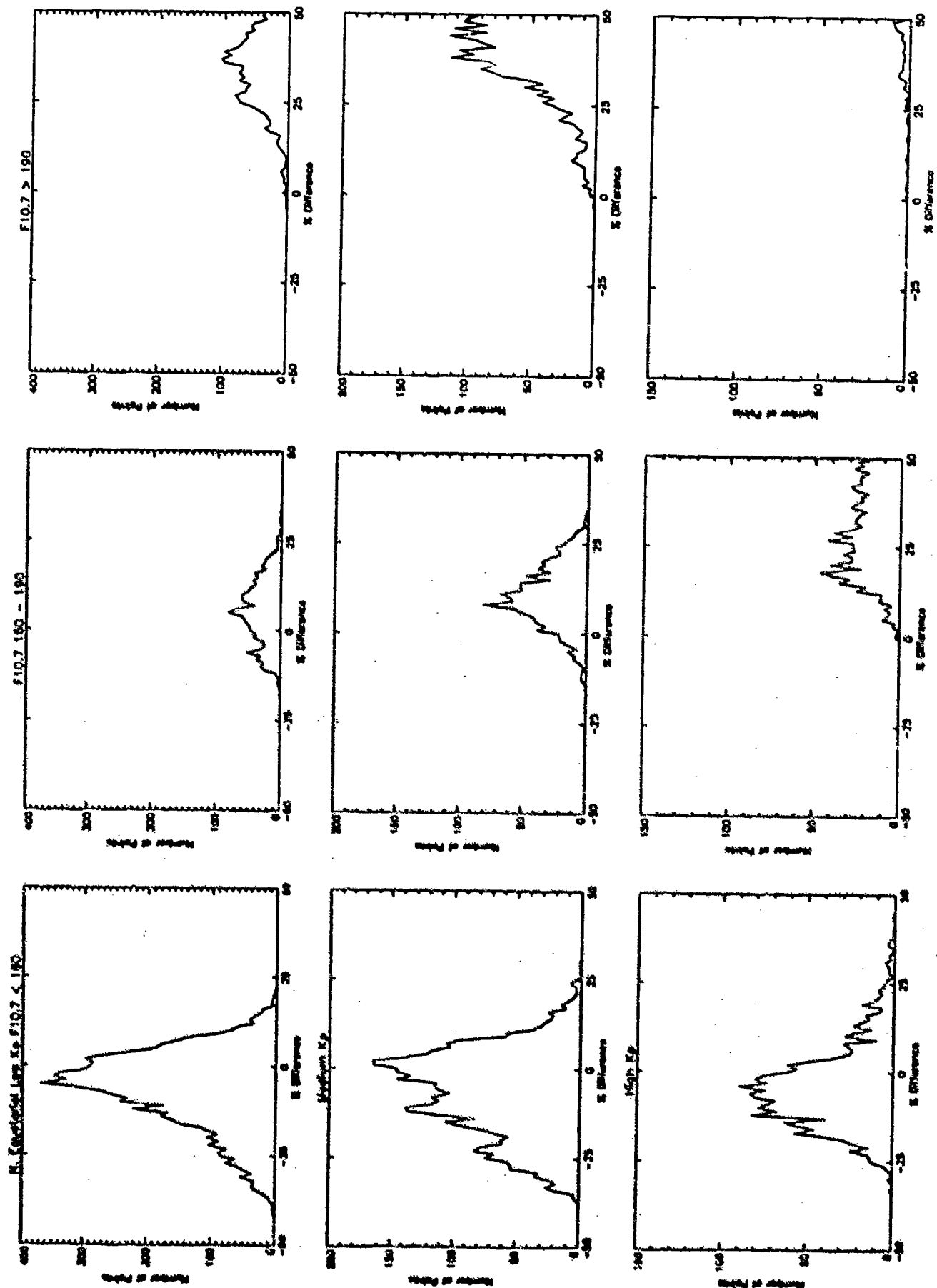
## F10.7 dependence plots

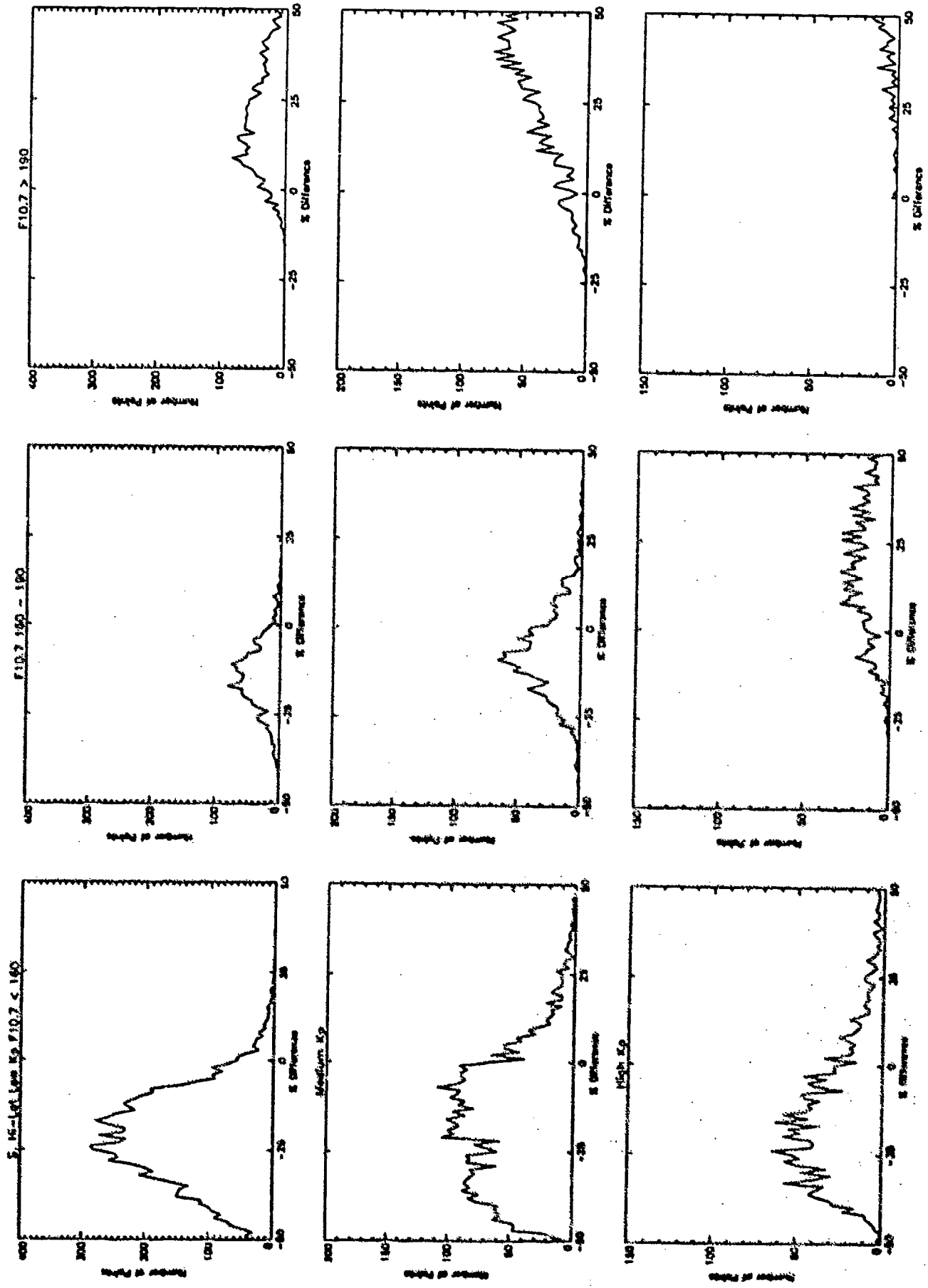
This appendix contains the plots described in section 3.2.1 that illustrated the F10.7 dependence depicted by the older version of VSH. The plots on each page represent one latitude region. The three columns represent the three F10.7 intervals and the rows represent the three Kp intervals. These plots show conclusively that the VSH curves were bifurcating based on solar flux inputs; ie. the large positively skewed area on the latitude plots occur during high F10.7 values as indicated by the plots in this appendix.

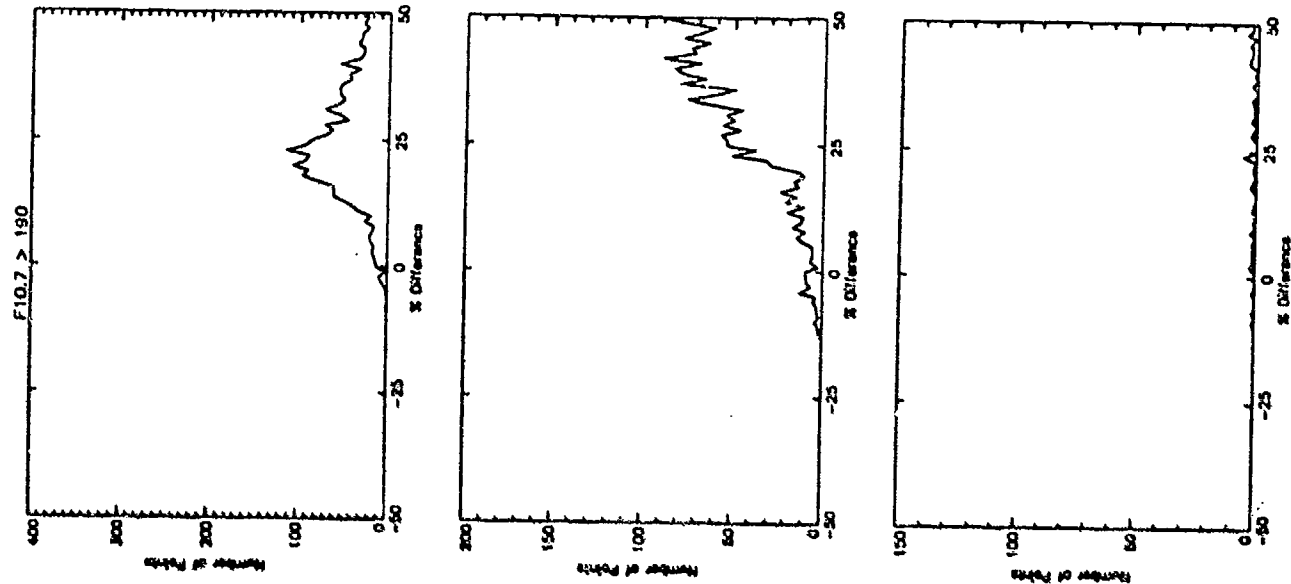
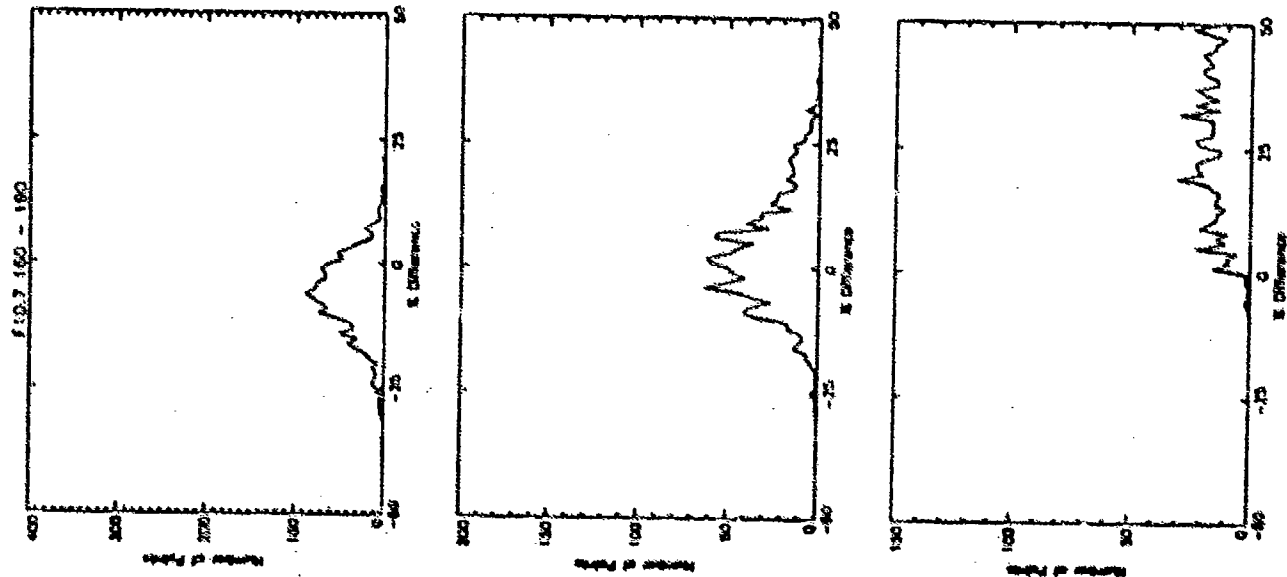
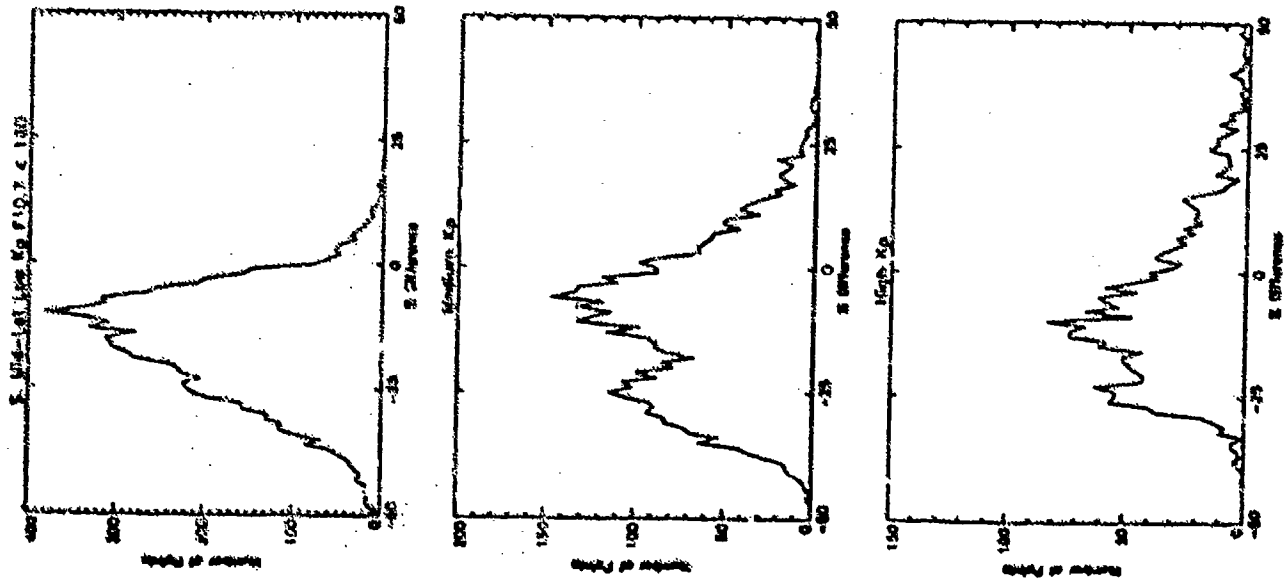






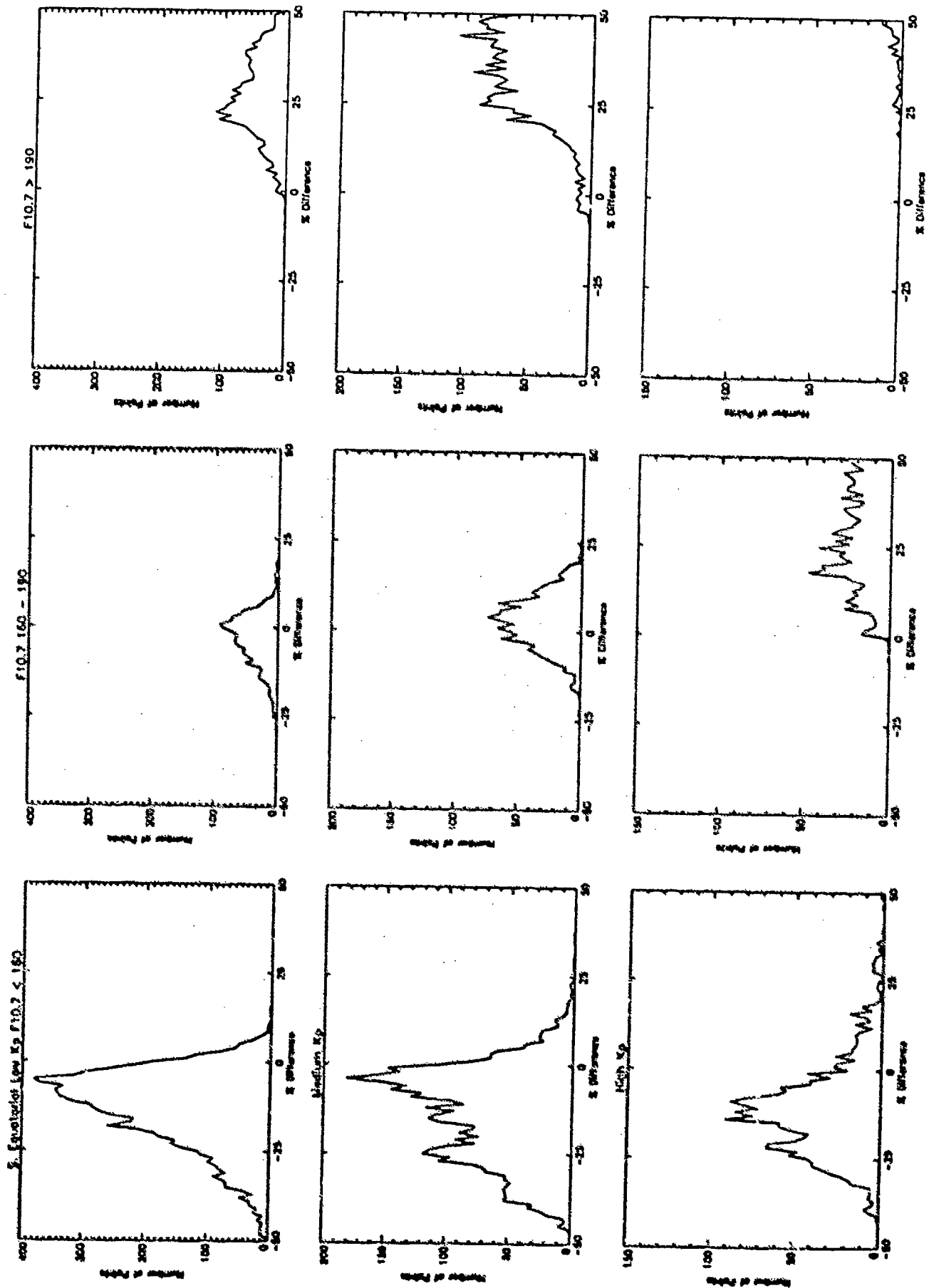






A-5 Same as A-1 except for S. Mid-latitude case.

A-6 Same as A-1 except for S. High latitude case.



## REFERENCES

## REFERENCES

- Bevington, P. R., Data Reduction and Error Analysis for the Physical Sciences, McGraw-Hill Book, 1969.
- Carignan, G. R., B. P. Block, J. C. Maurer, A. E. Hedin, C. A. Reber, N. W. Spencer, The neutral mass spectrometer on Dynamics Explorer B, Space Science Instrumentation, 5, 429-441, 1981.
- Dickinson, R. E., E. C. Ridley, and R. G. Roble, A three-dimensional, time-dependent general circulation model of the thermosphere, J. Geophys. Res., 86, 1499-1512, 1981.
- Emery, B. A., et al., Thermospheric and ionospheric structure of the southern hemisphere polar cap on October 21, 1981, as determined from Dynamics Explorer 2 satellite data, J. Geophys. Res., 90, 6553-6566, 1985.
- Forbes, J. M., Roble, R. G., Marcos, F. A., Thermospheric dynamics during the March 22, 1979, magnetic storm: 2. Comparisons of model predictions with observations, J. Geophys. Res., 92, 6069-6081, 1987.
- Fuller-Rowell, T. J. and D. Rees, A three-dimensional time-dependent model of the thermosphere, J. Atmos. Sci, 37, 2545-2567, 1980.
- Handbook of Geophysics and the Space Environment, Air Force Geophysics Lab, U.S. Air Force, 1985.
- Hedin, A. E., A revised thermospheric model based on mass spectrometer and incoherent scatter data: MSIS-83, J. Geophys. Res., 88, 10,170-10,188, 1983.
- Hedin, A. E., et al., A global thermospheric model based on mass spectrometer and incoherent scatter data: MSIS 1. N<sub>2</sub> density and temperature, J. Geophys. Res., 82, 2139-2156, 1977.
- Hedin, A. E., MSIS-86 Thermospheric model, J. Geophys. Res., 92, 4649-4662, 1987.
- Hedin, A. E., N. W. Spencer, T. L. Killeen, Empirical Global model of upper thermosphere winds based on Atmosphere and Dynamics Explorer satellite data, J. Geophys. Res., 9959-9978, 1988.
- Hinteregger, H. E., Representations of solar EUV fluxes for aeronautical applications, Adv. Space Res., 1, 39-52, COSPAR 1981.

- Hoffman, R. A., E. R. Schmerling, Dynamics Explorer Program: An Overview, Space Sci. Inst., 5, 345-348, 1981.
- Hoffman, R. A., G. D. Hogan, R. C. Maehl, Dynamics Explorer spacecraft and ground operations systems, Space Sci. Inst., 5, 349-367, 1981.
- Killeen, T. L., A. G. Burns, B. C. Kennedy, Feasibility study for the Atmospheric Density Specification (ADS) mission, 1988.
- Killeen, T. L., R. G. Roble, N. W. Spencer, A computer model of global thermospheric winds and temperatures, Adv. Space Res., 7, (10)207-(10)215, 1987.
- Killeen, T. L., R. G. Roble, R. Raskin, J. P. Thayer, R. M. Johnson, A. G. Burns, F. A. Marcos, Revised computer model of the thermosphere based on numerical model calculations and Dynamics Explorer satellite measurements, for submission to J. Geophys. Res., 1991.
- Marcos, F. A., Development and validation of new satellite drag models, AAA 91-491, AAS/AIAA Astrodynamics Specialist Conference, Durango, CO, 1991.
- Marcos, F. A., J. M. Forbes, Thermospheric winds from the satellite electrostatic triaxial accelerometer system, J. Geophys. Res., 90, 6543-6552, 1985.
- Marcos, F. A., T. L. Killeen, A. G. Burns, R. G. Roble, Evaluation of new atmospheric drag modeling techniques, Adv. Astron. Sci., 71, 763-782, 1989.
- Marcos, F. A., E. R. Swift, Application of the satellite triaxial accelerometer experiment to atmospheric density and wind studies, AFGL-TR-82-0091, 1982.
- Menvielle, M., A. Berthelier, The K-derived planetary indices: description and availability, Reviews of Geophysics, 29, 415-432, 1991.
- Press, W. H., B. P. Flannery, S. A. Teukolsky, W. T. Vetterling, Numerical Recipes: The Art of Scientific Computing, Cambridge University Press, 1986.
- Roble, R. G., J. M. Forbes, F. A. Marcos, Thermospheric dynamics during the March 22, 1979, magnetic storm: 1. Model simulations, J. Geophys. Res., 92, 6045-6068, 1987.
- Snow, D. E., J. J. F. Jiu, Atmospheric variations observed from orbit determination, AAS 91-492, AAS/AIAA Astrodynamics Specialist Conference, Durango, CO, 1991.

Spencer, N. W., L. E. Wharton, H. B. Niemann, A. E. Hedin, G. R. Carignan, J. C. Maurer, Space Sci. Inst., 5, 417-428, 1981.

Thayer, J. P., Neutral wind vortices in the high-latitude thermosphere, Technical Report, 1990.

Torr, M. R., P. G. Richards, D. G. Torr, Solar EUV energy budget of the thermosphere, Adv. Space Res., 1, 53-61, COSPAR 1981.